Synthesis of Stable Interfaces on SnO_2 Surfaces for Charge-Transfer Applications

By

Michelle C. Benson

A dissertation submitted in partial fulfillment of the requirements for the degree of

Doctor of Philosophy

(Chemistry)

At the

UNIVERSITY OF WISCONSIN-MADISON

2013

Date of final oral examination: 1/11/13

The dissertation is approved by the following members of the Final Oral Committee:
Robert Hamers, Professor, Chemistry (Materials)
Song Jin, Associate Professor, Chemistry (Materials)
John Wright, Professor, Chemistry (Analytical)
Kyoung-Shin Choi, Professor, Chemistry (Materials)
Martin Zanni, Professor, Chemistry (Physical)

Synthesis of Stable Interfaces on SnO_2 Surfaces for Charge-Transfer Applications

Michelle C. Benson

Under the supervision of Robert J. Hamers

University of Wisconsin-Madison

Abstract

The commercial market for solar harvesting devices as an alternative energy source requires them to be both low-cost and efficient to replace or reduce the dependence on fossil fuel burning. Over the last few decades there has been promising efforts towards improving solar devices by using abundant and non-toxic metal oxide nanomaterials. One particular metal oxide of interest has been SnO_2 due to its high electron mobility, wide-band gap, and aqueous stability. However SnO_2 based solar cells have yet to reach efficiency values of other metal oxides, like TiO_2. The advancement of SnO_2 based devices is dependent on many factors, including improved methods of surface functionalization that can yield stable interfaces.

This work explores the use of a versatile functionalization method through the use of the Cu(I)-catalyzed azide-alkyne cycloaddition (CuAAC) reaction. The CuAAC reaction is capable of producing electrochemically, photochemically, and electrocatalytically active surfaces on a variety of SnO_2 materials. The resulting charge-transfer characteristics were investigated as well as an emphasis on understanding the stability of the resulting molecular linkage. We determined the CuAAC reaction is able to proceed through both azide-modified and alkyne-modified surfaces. The resulting charge-transfer properties showed that the molecular tether was capable of supporting charge separation at the interface. We also investigated the enhancement of electron injection upon the introduction of an ultra-thin ZrO_2 coating on SnO_2. Several complexes were used to fully understand the charge-transfer capabilities, including model systems of ferrocene and a ruthenium coordination complex, a ruthenium mononuclear water oxidation catalyst, and a commercial ruthenium based dye.

Acknowledgements

I would first like to thank Professor Bob Hamers for his guidance, support, and kindness during the course of my graduate career. I am grateful for the opportunity to have worked with Bob and all the knowledge he has passed given me. Bob has also been more than a wealth of knowledge but a support for the entire research group as we faced trying times in our personal and research lives, and for that I cannot imagine having a better PhD thesis advisor.

Thanks to my collaborators in the Stahl group at the University of Wisconsin-Madison, Dr. James Gerkin and Matt Rigsby and Professor Randy Thummel and Dr. Ruifa Zong at the University of Houston for their synthesis of ruthenium coordination complexes for the attachment to SnO_2 surfaces.

I also want to thank Professor Jeff Rack at Ohio University for giving a young college sophomore a chance. I can affirm that without his mentorship I would not have considered graduate school and all the doors a PhD in chemistry can open.

The last person in my academic career I want to thank is Mrs. Lois Kuhns, my honors chemistry and AP teacher from Chardon high school. Without her enthusiasm and knowledge of chemistry plus the bribery of extra credit to join the science Olympiad team and compete in chemistry events, I do not think I would have considered a career in chemistry.

Thank you to my University of Wisconsin-Madison family. Without my friends, faculty, and staff this experience would not have been nearly as enjoyable and I am thankful for all the happy memories.

A special thanks to my mom, dad, sister (Nicole), and brother (Drew), without their support and unconditional love I know that I would not have become the person I am today.

Finally, to my wonderful husband, Jordan, there are no words to express my gratitude for your love and understanding these last several years. While your job took you thousands of miles away, you understood why I could not join you and how important it was for me to complete my graduate degree. Your words of encouragement every morning and night have given me the strength to accomplish my goals.

Table of Contents

Chapter 1

Introduction and Background

1.1. Nanotechnology for Renewable Energy Applications

The need for low-cost renewable energy is undeniable, as the continued burning of fossil fuels is known to have adverse environmental impacts.[1] Utilization of solar energy is the most promising of all the possible renewable energy sources due to the Sun's energy output in one hour is enough to power human's needs for an entire year.[2] However, challenges such as combining low-cost materials with high solar-to-electrical energy conversion continue to hinder the replacement of burning fossil fuels with solar devices.[1,2] The use of nanomaterials for photovoltaic solar cells has thus far been one of the most promising due the tunability of electronic and optical properties with reduced fabrication costs.[3-5]

One possibility for harvesting solar energy through the use of nanomaterials has been proposed through the fabrication of photoelectrochemical cells (PECs).[6-8] A sensitized PEC is capable of converting light into electrical energy through the use of a semiconductor sensitized by a species capable of absorbing sunlight, as shown in Figure 1.1.

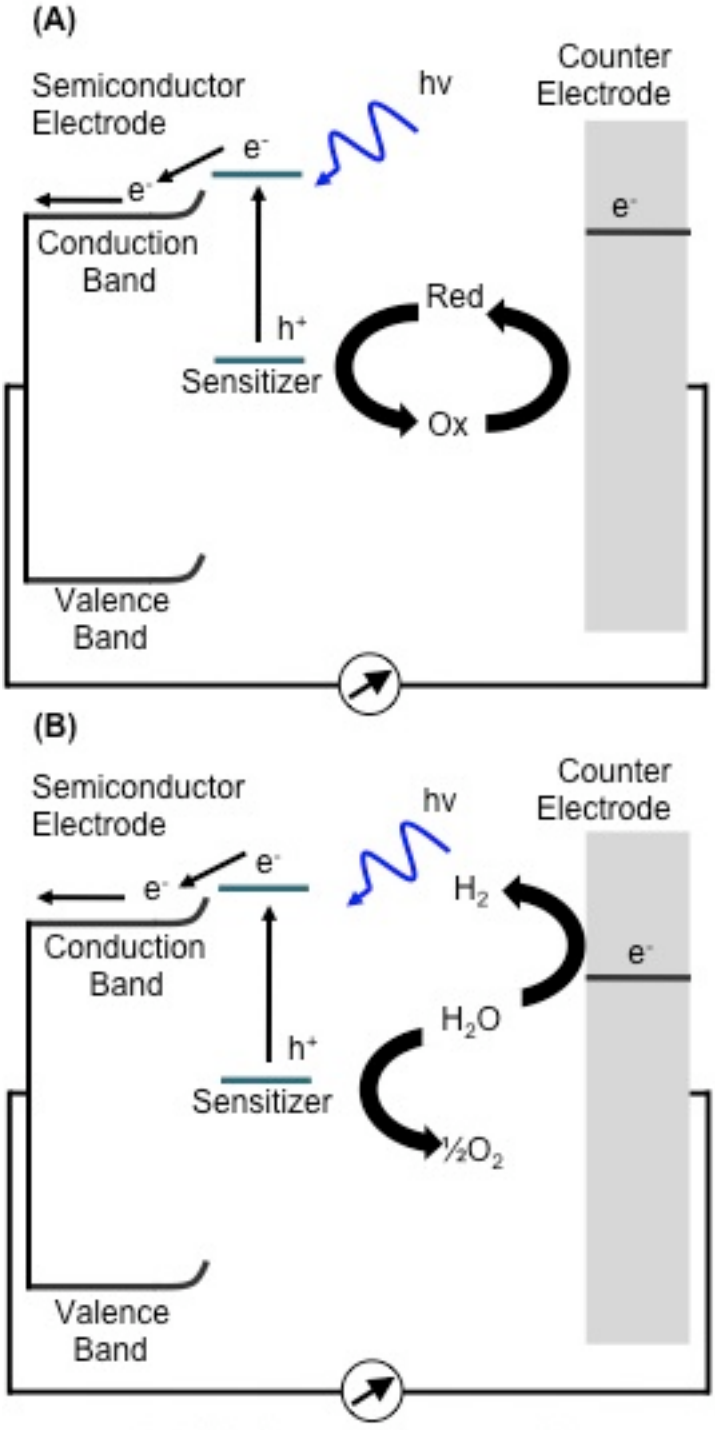

Figure 1.1: (A) Schematic drawing of photoelectrochemical cell with an n-type semiconductor and (B) Photocatalysis cell with an n-type semiconductor illustrating water splitting. Adapted from ref 7 and 8

The semiconducting electrode is termed sensitized due to the attachment of either a molecular absorber or an inorganic nanoparticle, which is capable of injecting photoexcited electrons into the conduction band of the semiconductor electrode to which it is attached.[8] Figure 1.1a depicts a regenerative type of cell where there is no net chemical change upon the generation of electricity. The second cell, shown in Figure 1.1b, involves a redox reaction initiated by solar irradiation, that is capable of splitting H_2O to produce H_2 for use as a fuel that burns without producing any carbon.[7,9] Both of these PECs require the use of a wide-band gap semiconductor. The semiconductor is named the “acceptor” due to conduction band alignment being able to accept injected electrons from the light-absorbing species, which is called the “donor”. The band gap of the semiconductor must be large enough so that the sunlight does not have enough energy to generate photoexcited charges within the semiconductor itself, which can limit the performance of the cell by causing photo-oxidation of the sensitized species. [10,11]

One famous example of a PEC cell is the dye-sensitized solar cell (DSSC) that was first introduced in 1991 by O’Regan and Grätzel.[12] An illustration summarizing the DSSC is shown in Figure 1.2, which shows a nanostructured TiO_2 electrode with an adsorbed Ruthenium dye onto the surface. The cell contains a counter electrode consisting of Pt coated fluorine-doped tin oxide (FTO) deposited onto glass. An electrolyte containing a redox couple, typically $I_3^-/3I^-$ is used to replenish the electron-deficient dye and complete the circuit. Since the introduction of the DSSC, the maximum reported efficiency has only been able to reach 11%.[13,14]

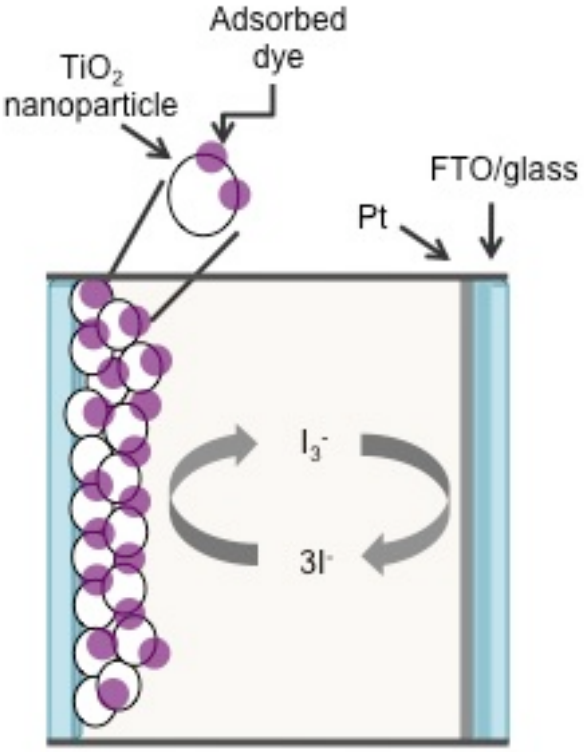

Figure 1.2: Schematic overview of the dye-sensitized solar cell using colloidal TiO_2 nanoparticles printed into a thin-film. Adapted from ref 13

There are several competing processes in these cells, which limit the efficiency of PECs such as recombination of photogenerated charge carriers and aqueous instability of adsorbed sensitizers.[15] To increase the efficiency of PECs, several modifications have been proposed, which include introduction of a covalent attachment between the acceptor and donor species, an insulating coating to reduce recombination, and alternative metal oxides with more robust electron mobilities.[10,15-22] The choice of TiO_2 for the acceptor semiconductor has dominated the research area of PECs because it is non-toxic, abundant, and possesses aqueous stability, however it may not be the most ideal wide-band gap semiconductor for improving solar conversion efficiencies.[14,23,24] Other metal oxides, such as SnO_2, have been proposed to replace TiO_2 in renewable energy applications.[14]

1.2. Motivation for SnO_2 in Renewable Energy Applications

SnO_2 is a wide-band gap semiconductor with a value of 3.6 eV,[25] which is larger than that of TiO_2 at 3.2 eV.[26] The greater band gap requires deep-UV light to generate excitons, which is only ~10% of the solar spectrum.[27] The lesser amount of excitons being generated decreases the amount of oxidizing holes, which are a known cause for degradation of adsorbed dyes and the redox couple in DSSCs thus, limiting the device's overall performance.[28] Figure 1.3 depicts a comparison of the band alignments of SnO_2, TiO_2, and a typical Ru-based dye. The absolute energy level of the conduction band of SnO_2 is lower than that of TiO_2, therefore the injection of the photoexcited electron from the dye into the conduction band of SnO_2 is thermodynamically more favorable than

TiO_2.[7] Besides SnO_2 having a larger band gap with preferred conduction band energy alignment, SnO_2 also possesses high electron mobility.

SnO_2 is an ideal material for applications in renewable technology due to its high electron mobility of 10 $cm^2V^{-1}s^{-1}$, which is several orders of magnitude higher than TiO_2 with an electron mobility of ~ $1x10^{-4}$ to $1x10^{-6}$ $cm^2V^{-1}s^{-1}$.[18,19] The increased electron mobility is theorized to be the result of the intrinsic oxygen defects in the crystal lattice, which are tolerated by the multi-valence nature of the Sn atom.[29] Despite the preferred band alignment and increased electron mobility, SnO_2-based PECs have yet to reach the performance of PECs based on TiO_2.[18,20,22,30]

The increased electron mobility, although optimal for creating low-resistance thin films and facilitating charge transfer, it also is also theorized to increase the rate of recombination with the adsorbed donor or the redox couple.[31] The ability to control the surface chemistry of the SnO_2 could lead to enhanced electron injection and increased stability while decreasing recombination. However, surface functionalization techniques for SnO_2 have not been well developed and often rely on electrostatic interactions, which are not capable of withstanding aqueous conditions, resulting in desorption of the donor species.[30,32-34]

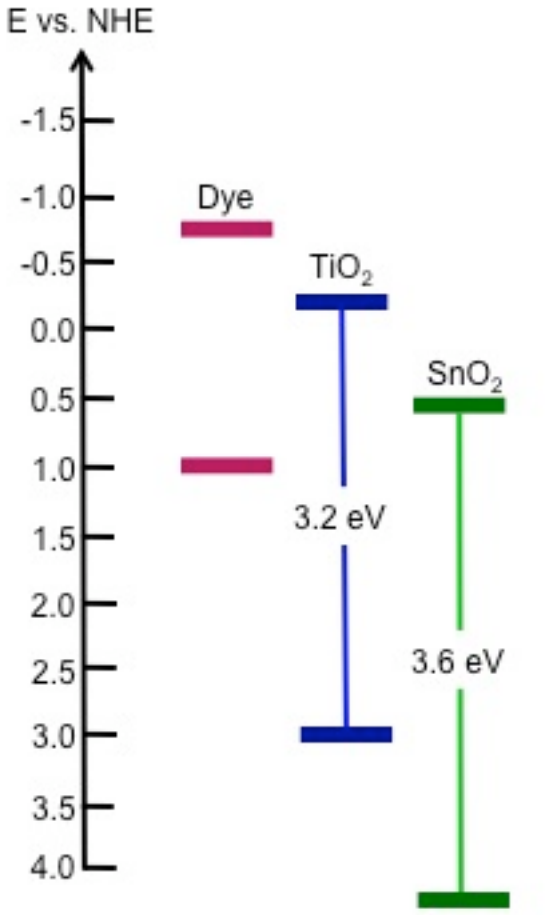

Figure 1.3: Schematic illustration comparing conduction and valence band alignments for TiO_2, SnO_2, and a typical Ru-based dye

1.3. Development of Modular Surface Chemistry for Synthesizing Stable Interfaces

Devices, such as PECs, rely on the ability to efficiently separate the photogenerated charges, which are then required to move through an interface before they can be utilized.[35] Therefore, the engineering of a stable interface that can effectively separate charge is pivotal to achieve better performing devices.[35,36] Improved surface functionalization techniques of SnO_2 can allow for covalent attachment of redox active molecules, molecular sensitizers, or nanoparticles with a desirable band alignment to the surface as well as facilitate charge transfer.[16,37,38] Covalent linkages to the surface of metal oxides have been shown to be highly stable under a variety of conditions as compared to adsorption through a carboxyl functional group that is often used as an anchor to the metal oxide surface.[39,40] The ability to covalently link a molecule of interest to the surface of SnO_2 could increase the overall stability of the system. A modular approach for introducing surface functionality would allow for versatility in the application of SnO_2 in PEC devices.

A class of organic reactions termed “click” chemistry is a possible route to introduce a covalent linkage between SnO_2 and a molecule of interest. “Click” reactions are selective with mild conditions, fast reaction times, and high yields.[41-43] One example of a “click” reaction that has been able to introduce functionality to a variety of surfaces is the Cu (I) catalyzed azide-alkyne cycloaddition (CuAAC) reaction, shown in Figure 1.4.[44-47] The CuAAC reaction involves the cycloaddition of a terminal alkyne with a terminal azide that results in a conjugated triazole ring that is thermally, hydrolytically,

and electrochemically stable.[43,44,46,48] The introduction of either an alkyne or azide to the surface of SnO_2 would allow for reaction with anything that bears the complementary functional group. Introducing a covalent linkage to the surface of SnO_2 that is capable of undergoing a modular approach could introduce versatility with increased stability of the organic-inorganic interface, however it does not change the intrinsic nature of SnO_2, which still limits the efficiency in PECs.

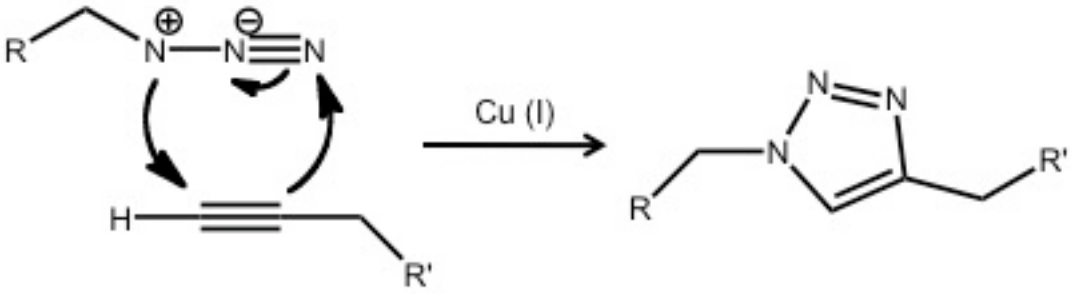

Figure 1.4: Schematic illustration of the CuAAC reaction between a terminal azide and alkyne in the presence of Cu (I)

1.4. Insulating Metal Oxide Coatings on SnO_2

Another potential method to increase SnO_2 overall efficiency is the introduction of an insulating metal oxide coating, which could reduce recombination and increase the electronic coupling between the SnO_2 nanocrystalline thin film and the adsorbed dye.[17,19,49-51] Several studies have shown the initial electron injection rate from adsorbed dye for SnO_2 is much less than for TiO_2.[52-54] The disparity between the two metal oxides is theorized to be due to the difference in their orbitals, that comprise the conduction bands resulting in poor electronic overlap between the adsorbed dye and increased rates of recombination.[31,55]

The conduction band of SnO2 consists of empty s and p orbitals which have densities of states orders of magnitude less than the d orbitals that comprise the conduction band of TiO2, as shown in Figure 1.5.[26,52,56] If the electronic coupling of the adsorbed dye relies on the overlap of the π* orbitals in the dye and empty conduction band orbitals of the semiconductor, the difference in electron injection kinetics could arise from there being fewer accepting states available for SnO2 as compared to TiO2.[52,56] Introduction of a thin coating of an insulating metal oxide onto SnO2 that introduces empty d orbitals could increase the electronic coupling between the donor species resulting in an increase in the electron injection efficiencies. It has also been theorized that an insulating metal oxide can also serve as an electron-blocking layer by increasing the physical separation between the SnO2 and the donor species, thus reducing recombination pathways as depicted in Figure 1.6.[21,57,58]

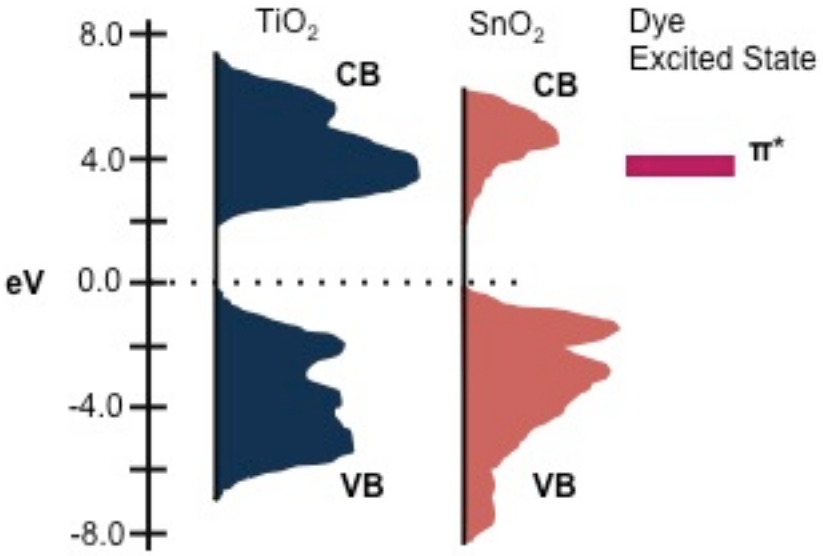

Figure 1.5: Representation of the density of states of the conduction bands (CB) and valence bands (VB) for TiO_2 and SnO_2 and approximate alignment with excited state of a dye (π^*). Adapted from ref 56

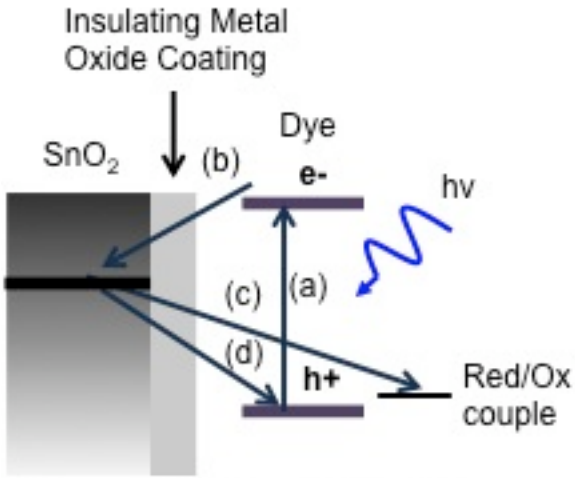

Figure 1.6: Schematic illustration representing possible pathways of reducing recombination. (a) photogeneration of electron, (b) electron injection into conduction band of SnO_2, (c) recombination of electron with red/ox couple (d) recombination with oxidized dye. Adapted from ref 21

1.5. Scope of Thesis

The work presented here investigates the ability to functionalize different morphologies of SnO_2 including nanocrystalline thin-films, nanorods, and planar fluorine-doped SnO_2. Chapter 2 will explore the step-wise surface functionalization technique to introduce an azide-modified SnO_2 nanocrystalline surface. The azide-modified surface is then able to undergo modular attachment of two model molecular species through the use of the CuAAC reaction. The resulting electrochemically and photoelectrochemically active surfaces are characterized using electrochemistry and time-resolved surface photovoltage. Chapter 3 will continue to evaluate the modular surface attachment and the versatility of CuAAC reaction by investigating SnO_2 nanorods and planar fluorine-doped tin oxide electrodes, with the attachment of a ruthenium coordination complex that exhibits water oxidation capabilities. The SnO_2 nanorods provide well-defined crystal planes and increased surface area as compared to the nanocrystalline thin-films, providing a platform in which the photoactive ruthenium complex is tethered and characterized using time-resolved surface photovoltage. The fluorine-doped tin oxide electrodes provide a conductive substrate in which the ruthenium coordination complex is covalently attached to form a heterogeneous catalyst. The heterogeneous catalyst stability and ability to oxidize water is evaluated and compared to an unmodified fluorine-doped tin oxide electrode. Chapter 4 will probe the functionalization of SnO_2 nanocrystalline thin-films with an alkyne group through a thermal grafting method. A small molecule with an azido functionality and CF_3 group is used to characterize the ability for the alkyne-modified surface to undergo CuAAC

reaction and investigate the aqueous stability of the modification. The CF_3 group provides a tag for x-ray photoelectron spectroscopy and Fourier-transform infrared analysis. Chapter 5 will evaluate the introduction an ultra-thin coating of ZrO_2 on SnO_2 thin-films and the effect that the introduction of d-band character has on the initial electron injection from a commercial ruthenium dye. Chapter 6 will include final conclusions and future directions with the work the reported here.

1.6. References

(1) Dresselhaus, M. S.; Thomas, I. L. *Nature* **2001**, *414*, 332.

(2) Lewis, N. S.; Nocera, D. G. *Proceedings of the National Academy of Sciences of the United States of America* **2006**, *103*, 15729.

(3) Lunt, R. R.; Osedach, T. P.; Brown, P. R.; Rowehl, J. A.; Bulovic, V. *Adv. Mater.* **2011**, *23*, 5712.

(4) Kamat, P. V. *Journal of Physical Chemistry C* **2007**, *111*, 2834.

(5) Tetreault, N.; Gratzel, M. *Energy Environ. Sci.* **2012**, *5*, 8506.

(6) Bak, T.; Nowotny, J.; Rekas, M.; Sorrell, C. C. *International Journal of Hydrogen Energy* **2002**, *27*, 991.

(7) Gratzel, M. *Nature* **2001**, *414*, 338.

(8) Youngblood, W. J.; Lee, S. H. A.; Maeda, K.; Mallouk, T. E. *Accounts of Chemical Research* **2009**, *42*, 1966.

(9) Bard, A. J.; Fox, M. A. *Accounts of Chemical Research* **1995**, *28*, 141.

(10) Hinsch, A.; Kroon, J. M.; Kern, R.; Uhlendorf, I.; Holzbock, J.; Meyer, A.; Ferber, J. *Progress in Photovoltaics* **2001**, *9*, 425.

(11) Sommeling, P. M.; Spath, M.; Smit, H. J. P.; Bakker, N. J.; Kroon, J. M. *Journal of Photochemistry and Photobiology a-Chemistry* **2004**, *164*, 137.

(12) O'Regan, B.; Gratzel, M. *Nature* **1991**, *353*, 737.

(13) Chen, C. Y.; Wang, M. K.; Li, J. Y.; Pootrakulchote, N.; Alibabaei, L.; Ngoc-le, C. H.; Decoppet, J. D.; Tsai, J. H.; Gratzel, C.; Wu, C. G.; Zakeeruddin, S. M.; Gratzel, M. *Acs Nano* **2009**, *3*, 3103.

(14) Nazeeruddin, M. K.; Kay, A.; Rodicio, I.; Humphrybaker, R.; Muller, E.; Liska, P.; Vlachopoulos, N.; Gratzel, M. *J. Am. Chem. Soc.* **1993**, *115*, 6382.

(15) Asghar, M. I.; Miettunen, K.; Halme, J.; Vahermaa, P.; Toivola, M.; Aitola, K.; Lund, P. *Energy Environ. Sci.* **2010**, *3*, 418.

(16) Benson, M. C.; Ruther, R. E.; Gerken, J. B.; Rigsby, M. L.; Bishop, L. M.; Tan, Y. Z.; Stahl, S. S.; Hamers, R. J. *Acs Applied Materials & Interfaces* **2011**, *3*, 3110.

(17) Cai, F. S.; Yuan, Z. H.; Duan, Y. Q.; Bie, L. J. *Thin Solid Films* **2011**, *519*, 5645.

(18) Chappel, S.; Zaban, A. *Sol. Energy Mater. Sol. Cells* **2002**, *71*, 141.

(19) Guo, J.; She, C.; Lian, T. *Journal of Physical Chemistry C* **2007**, *111*.

(20) Jose, R.; Thavasi, V.; Ramakrishna, S. *Journal of the American Ceramic Society* **2009**, *92*, 289.

(21) Palomares, E.; Clifford, J. N.; Haque, S. A.; Lutz, T.; Durrant, J. R. *J. Am. Chem. Soc.* **2003**, *125*, 475.

(22) Tiwana, P.; Docampo, P.; Johnston, M. B.; Herz, L. M.; Snaith, H. J. *Energy Environ. Sci.* **2012**, *5*, 9566.

(23) Chen, X.; Mao, S. S. *Chem. Rev.* **2007**, *107*, 2891.

(24) Ito, S.; Murakami, T. N.; Comte, P.; Liska, P.; Gratzel, C.; Nazeeruddin, M. K.; Gratzel, M. *Thin Solid Films* **2008**, *516*, 4613.

(25) Batzill, M.; Diebold, U. *Progress in Surface Science* **2005**, *79*, 47.

(26) Diebold, U. *Surf. Sci. Rep.* **2003**, *48*, 53.

(27) Fu, Q. In *Radiation (Solar)*; Elsevier Science Ltd.: 2003, p 1859.

(28) Hagfeldt, A.; Boschloo, G.; Sun, L. C.; Kloo, L.; Pettersson, H. *Chem. Rev.* **2010**, *110*, 6595.

(29) Kilic, C.; Zunger, A. *Physical Review Letters* **2002**, *88*.

(30) Stergiopoulos, T.; Arabatzis, I. M.; Cachet, H.; Falaras, P. *Journal of Photochemistry and Photobiology a-Chemistry* **2003**, *155*, 163.

(31) Green, A. N. M.; Palomares, E.; Haque, S. A.; Kroon, J. M.; Durrant, J. R. *Journal of Physical Chemistry B* **2005**, *109*, 12525.

(32) Liu, D.; Kamat, P. V. *Journal of the Electrochemical Society* **1995**, *142*, 835.

(33) Ferrere, S.; Zaban, A.; Gregg, B. A. *The Journal of Physical Chemistry B* **1997**, *101*, 4490.

(34) Subbaiyan, N. K.; Maligaspe, E.; D'Souza, F. *Acs Applied Materials & Interfaces* **2011**, *3*, 2368.

(35) Gregg, B. A.; Pichot, F.; Ferrere, S.; Fields, C. L. *Journal of Physical Chemistry B* **2001**, *105*, 1422.

(36) Ning, Z. J.; Fu, Y.; Tian, H. *Energy Environ. Sci.* **2010**, *3*, 1170.

(37) Cardiel, A. C.; Benson, M. C.; Bishop, L. M.; Louis, K. M.; Yeager, J. C.; Tan, Y. Z.; Hamers, R. J. *Acs Nano* **2012**, *6*, 310.

(38) Shah, S.; Benson, M. C.; Bishop, L. M.; Huhn, A. M.; Ruther, R. E.; Yeager, J. C.; Tan, Y. Z.; Louis, K. M.; Hamers, R. J. *Journal of Materials Chemistry* **2012**, *22*, 11561.

(39) Chen, J. X.; Franking, R.; Ruther, R. E.; Tan, Y. Z.; He, X. Y.; Hogendoorn, S. R.; Hamers, R. J. *Langmuir* **2011**, *27*, 6879.

(40) Franking, R. A.; Landis, E. C.; Hamers, R. J. *Langmuir* **2009**, *25*, 10676.

(41) Rostovtsev, V. V.; Green, L. G.; Fokin, V. V.; Sharpless, K. B. *Angewandte Chemie-International Edition* **2002**, *41*, 2596.

(42) Tornoe, C. W.; Christensen, C.; Meldal, M. *Journal of Organic Chemistry* **2002**, *67*, 3057.

(43) Finn, M. G.; Kolb, H. C.; Fokin, V. V.; Sharpless, K. B. *Progress in Chemistry* **2008**, *20*, 1.

(44) Landis, E. C.; Hamers, R. J. *Chemistry of Materials* **2009**, *21*, 724.

(45) Lee, J. K.; Chi, Y. S.; Choi, I. S. *Langmuir* **2004**, *20*, 3844.

(46) Ruther, R. E.; Rigsby, M. L.; Gerken, J. B.; Hogendoorn, S. R.; Landis, E. C.; Stahl, S. S.; Hamers, R. J. *J. Am. Chem. Soc.* **2011**, *133*, 5692.

(47) Devaraj, N. K.; Collman, J. P. *Qsar & Combinatorial Science* **2007**, *26*, 1253.

(48) Collman, J. P.; Devaraj, N. K.; Chidsey, C. E. D. *Langmuir* **2004**, *20*, 1051.

(49) Kim, M. H.; Kwon, Y. U. *Journal of Physical Chemistry C* **2011**, *115*, 23120.

(50) Prasittichai, C.; Hupp, J. T. *Journal of Physical Chemistry Letters* **2010**, *1*, 1611.

(51) Kay, A.; Gratzel, M. *Chemistry of Materials* **2002**, *14*, 2930.

(52) Ai, X.; Anderson, N. A.; Guo, J. C.; Lian, T. Q. *Journal of Physical Chemistry B* **2005**, *109*, 7088.

(53) Bauer, C.; Boschloo, G.; Mukhtar, E.; Hagfeldt, A. *International Journal of Photoenergy* **2002**, *4*, 17.

(54) Benko, G.; Myllyperkio, P.; Pan, J.; Yartsev, A. P.; Sundstrom, V. *J. Am. Chem. Soc.* **2003**, *125*, 1118.

(55) Katoh, R.; Furube, A.; Yoshihara, T.; Hara, K.; Fujihashi, G.; Takano, S.; Murata, S.; Arakawa, H.; Tachiya, M. *Journal of Physical Chemistry B* **2004**, *108*, 4818.

(56) Thomazi, F.; Roman, L. S.; Silva, A. F. d.; Persson, C. *physica status solidi (c)* **2009**, *6*, 2740.

(57) Tennakone, K.; Bandara, J.; Bandaranayake, P. K. M.; Kumara, G. R. A.; Konno, A. *Japanese Journal of Applied Physics Part 2-Letters* **2001**, *40*, L732.

(58) Tennakone, K.; Perera, V. P. S.; Kottegoda, I. R. M.; De Silva, L. A. A.; Kumara, G.; Konno, A. *Journal of Electronic Materials* **2001**, *30*, 992.

Chapter 2

Modular "Click" Chemistry for Electrochemically and Photoelectrochemically Active Molecular Interfaces to Tin Oxide Surfaces

The following chapter was published in *ACS Applied Materials and Interfaces*, **2011**, 3 (8), 3110–3119.

2.1. Introduction

Recent interest in hybrid organic–inorganic structures for applications such as low-cost solar cells[1-6] and photocatalysis[7-10] is placing increased emphasis on the development of optimized interfacial chemistries for linking molecular systems to metal oxide semiconductors. SnO_2 is of interest because of the semiconducting nature, which enhances charge separation at the molecule-semiconductor interface.[11,12] SnO_2 is of particular relevance in applications such as dye-sensitized solar cells[13-22] because the conduction band of SnO_2 is lower in absolute energy than that of the commonly studied TiO_2, facilitating electron transfer from surface-attached molecules into SnO_2.[13] The larger band gap of 3.6 eV also reduces creation of photoexcited holes, which are known to degrade surface-attached dyes.[20,22] Finally, SnO_2 films exhibit electron mobilities on the order of 10 $cm^2\ V^{-1}\ s^{-1}$, [23,24] much higher than the values of $\sim 1 \times 10^{-4}$ to 1×10^{-6} $cm^2\ V^{-1}\ s^{-1}$ typically obtained from nanocrystalline TiO_2 films.[25] The advantage of high electron mobility is enhancement of charge separation and production of low resistance films.

Previous studies have shown that molecules terminated with carboxylic acid[19,26] phosphonic acid,[27,28] and silane groups[19,21] can be used to link molecules to SnO_2 surfaces through a one-step adsorption mechanism. These highly functional molecules such as dyes or catalysts to metal oxides typically requires relatively difficult synthesis and purification steps en route to each of the derivatized compounds.[28,29] A more general approach to forming molecular interfaces to surfaces uses a bifunctional molecule that links to the surface using one functional group and leaves the second functional group exposed at the outermost surface which is available for further reaction with a the desired molecular species. A bifunctional-linker approach has been used to make electrochemically or photoelectrochemically active surfaces of materials including silicon,[30-32] diamond,[33,34] gold,[35] graphite,[36] and SnO_2.[19] In this two-step approach, surface attachment and compound synthesis chemistries thus become modular and orthogonal. Recent studies have shown a versatile route for the synthesis of surfaces[34-37] with a high degree of functionality through the generically known “click” reaction.[38-40] The Cu (I)-catalyzed azide–alkyne cycloaddition (CuAAC) reaction is of particular interest because studies on carbon surfaces have shown that the resulting triazole linkages are highly stable even under highly oxidizing conditions and support electron-transfer processes.[34,35,37,41]

Here, we present a modular approach for synthesis of molecular interfaces through the use of the Cu (I)-catalyzed azide–alkyne cycloaddition (CuAAC). Our results show that grafting of a short alkene chain with a terminal alcohol group can be converted to produce an azide-modified SnO_2 surface. Through the azide terminated

surface it is possible to use the CuAAC reaction to link more complex molecular structures to SnO_2 surface. Model systems consisting of ferrocene and a ruthenium terpyridyl complex were used to demonstrate that the resulting interfaces support both electrochemical and photoelectrochemical charge transfer.

2.2. Experimental

2.2.1. Preparation of SnO_2 nanoparticles and SnO_2 thin films

SnO_2 nanoparticles were synthesized following previously reported procedures, via hydrolysis of $SnCl_4$ under basic conditions followed by calcining.[42] In a typical reaction 2.22 mmol of $SnCl_4 \cdot 4H_2O$ and 50.0 mmol of NaOH were ball-milled for 15 s, followed by addition of 1.11 mmol NaCl and further milling for 30 s. The mixture was annealed at 400 °C for 2 h, washed with deionized water three times, then dried at 100 °C for 1 h. The resulting nanocrystalline SnO_2 powder was collected and analyzed using scanning electron microscopy (SEM) and X-ray diffraction (XRD) methods, shown in Figure 2.1a and 2.1b respectively. Figure 2.1a shows an SEM image of the nanoparticles with an average diameter of approximately 50 nm dispersed on a conducting substrate. XRD data of the nanoparticles, shown in Figure 2.1b demonstrates the majority are tetragonal (aka cassiterite) which is the most common phase of SnO_2.[13] A comparison of purchased nanoparticles (Nanostructured and Amorphous Materials, Los Alamos, NM) and the synthesized nanoparticles showed no significant difference in experimental results.

The nanoparticles were sintered to form a nanocrystalline thin film before further surface modification by adaptation of a previously reported procedure.[43] Typically, a 120 mg sample of SnO_2 was suspended in absolute ethanol via sonication. To the suspended mixture was mixed 335 mg of 10 wt % ethyl cellulose (46070, Sigma-Aldrich) in absolute ethanol (EtOH) with 260 mg of 10 wt % (in absolute EtOH) ethyl cellulose (46080, Sigma-Aldrich), and 484 mg of anhydrous terpineol were added. The mixture was subjected to ultrasonication for 30 min and the solvent was removed using rotary evaporation. The paste was then screen-printed onto the desired substrate, and the screen-printed substrate with paste applied was sintered at 600 °C for 1 h, followed by one additional hour at 500 °C. This procedure yielded a highly textured sintered film well suited for further functionalization and analysis. All experiments were performed using substrates consisting of a thin film of fluorinated tin oxide (FTO) on glass (sheet resistance 15 Ω/sq,) because these substrates provide good electrical contact to the SnO_2 nanoparticle films and are transparent. As an additional control to ensure the SnO_2 nanoparticle film was being probed and not the underlying substrate, duplicate XPS experiments were performed on some samples using substrates consisting of 100 nm Ti evaporated onto heavily doped Si wafers, Unless otherwise stated, all results shown here were obtained using sintered SnO_2 films fabricated on the fluorinated tin oxide substrates.

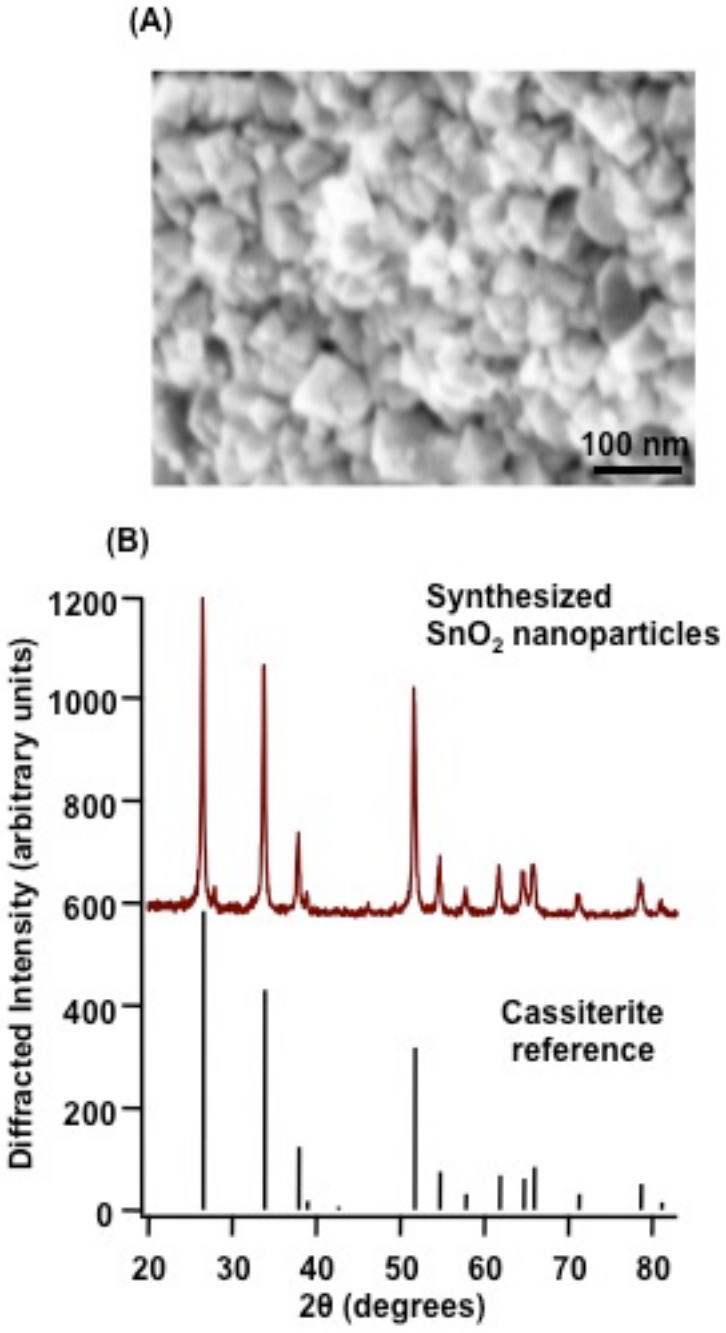

Figure 2.1: (A) SEM top-down image of synthesized SnO_2 nanoparticles (B) XRD diffraction pattern with cassiterite reference

A representative SEM image after the nanoparticles were synthesized into a continuous film is shown in Figure 2.2. SEM images of multiple samples showed that the SnO_2 films used were typically 700 nm to 1 μm in thickness. The sintered SnO_2 films have a highly textured surface but have a relatively low porosity. The highly textured nature of the SnO_2 surface provided higher surface area than a comparable planar film (estimated as approximately a 2-fold enhancement by visual inspection of the SEM images), thereby enhancing the sensitivity of the surface analytical measurements. We chose to use sintered films with a low porosity in studies presented here because this structure confined the liquid reactants to a thin layer near the outmost surface, thereby avoiding potential reactions with the underlying substrate, enhancing transport of reactants to the SnO_2 surface reaction sites, and facilitating proper rinsing of the SnO_2 films after reaction. These factors are important in making unambiguous distinction between species chemically bound to the SnO_2 surface and those physically adsorbed or trapped in the film via non-covalent interactions.

2.2.2. Molecular Reagents

Three different molecules were used to study the coupling chemistry to the SnO_2 surface. The compounds 4-(trifluoromethoxy)phenylacetylene (TFMPA) and ethynylferrocene were purchased commercially (Sigma-Aldrich). The $[Ru(tpy)(tpy')]^{2+}$ (tpy = 2,2′:6′,2″-terpyridyl), (tpy′=4-ethynyl-2,2′:6′,2″-terpyridyl) derivative bearing a

pendant alkyne group was prepared using a procedure published previously.[44] All other reagents were purchased from Sigma-Aldrich unless stated otherwise.

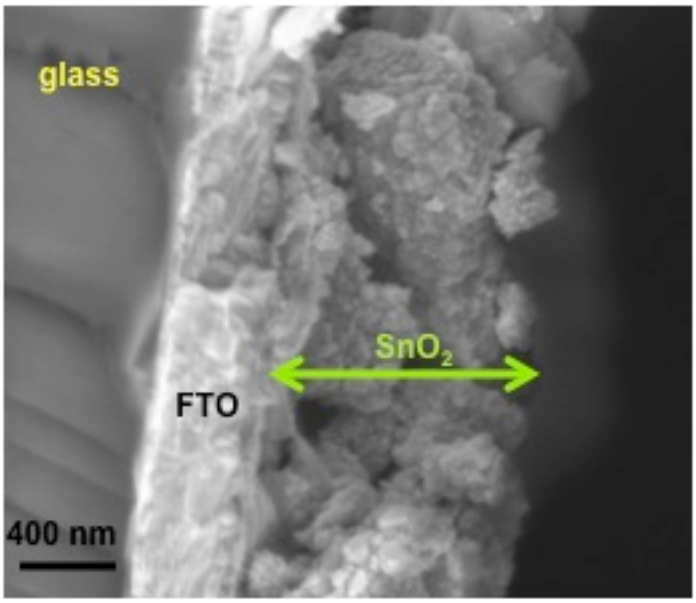

Figure 2.2: SEM cross-section image of SnO_2 nanoparticles after film processing on FTO substrate

2.2.3. Fourier-Transform Infrared (FTIR) Measurements

Infrared spectra were collected using an FTIR spectrometer (Vertex 70, Bruker Optics, Billerica, MA) at a resolution of 4 cm^{-1}. FTIR spectra were collected in single-bounce external reflection mode using a variable angle specular reflectance accessory with a wire grid polarizer (VeeMAX II, Pike Technologies, Madison, WI). All reflection spectra were collected with p-polarized light at an incident angle of 50° from the surface normal. FTIR spectra of functionalized surfaces were measured using an unfunctionalized sample as the background. Residual baselines were removed to improve the clarity of the spectra. Baseline correction was achieved using a polynomial fit to remove sloping and/or curved background. A single polynomial was fit to each spectrum, taking care to avoid any regions containing peaks likely to be associated with surface species. The polynomial fits typically included the following regions: 3150–3250, 2700–2420, 2300–2175, 1890–1770, and 1670–1490 cm^{-1}. In each case, the experimental spectrum was fit to a polynomial using all points in the selected regions, and the resulting polynomial was then subtracted from the data. In general, fits were performed using several different polynomial orders in order to ensure that the spectral features observed were not sensitive to the precise details of the fitting procedure.

2.2.4. X-ray Photoelectron Spectroscopy (XPS)

XPS data were obtained using a custom-built XPS system (Physical Electronics Inc., Eden Prairie, MN) consisting of a model 10–610 Al Kα source (1486.6 eV photon energy) with a Model 10–420 toroidal monochromator and a model 10–360

hemispherical analyzer with a 16-channel detector array; measurements were typically performed using a electron takeoff angle of 45°. Peak areas were calculated by fitting the raw data to Voigt functions after a Shirley baseline correction.[45,46] The Voigt function consists of a mixed Gaussian–Lorentzian of the form $f(x) = (A)/[1+(m(E - E_0)^2)/(w^2)] \exp[(1 - m)(\ln 2)(E - E_0)^2/(w^2)]$.[47] In this equation, w is the peak width parameter, E_0 is the binding energy of the peak center, E is the binding energy, m is the mixing ratio (m = 0 for pure Gaussian, m = 1 for pure Lorentzian), and A is an amplitude coefficient. The spectra of each sample were shifted as necessary to make the primary C(1s) peak lie at a fixed energy of 284.4 eV; all other spectra for a given sample were shifted by the same amount.

2.2.5. Electrochemical Characterization

All electrochemical measurements were performed using an Autolab potentiostat (PGSTAT302N, Metrohm Autolab B.V., Utrecht, The Netherlands) using the SnO_2 samples as the working electrode, a Bioanalytical Systems (BASi, West Lafayette, IN) Ag/AgCl junctioned reference electrode, and a platinum wire counter-electrode. The aqueous Ag/AgCl reference electrode consisted of a silver wire immersed in a solution of 3 M NaCl.

2.2.6. Optical Characterization

Absorption spectra were obtained on a UV–visible spectrophotometer (UV240PC, Shimadzu, Addison, IL). Excitation and emission spectra were measured on a spectrofluorimeter (Model K2, ISS, Champaign-Urbana IL).

2.2.7. Time-Resolved Surface Photovoltage (TR-SPV) Measurements

Time-resolved surface photovoltage measurements[47-49] were performed using a custom-made cell holder in which an FTO sense electrode was held 25 μm away from the sample surface. The entire cell was sealed inside an argon glovebox. The sample was illuminated with short pulses (<3 ns, 600 μJ/pulse) from a tunable laser system (NT340, Ekspla, Inc., Vilnius, Lithuania); the resulting injection of electrons from the surface into the bulk induced transient changes in the potential, and these changes were measured at the pickup electrode. The sense electrode signal was amplified using a fast amplifier (Model TA2000B-3, FAST ComTec GmbH, Oberhaching/München, Germany) with a 50 Ω input and output impedances, 1.5 GHz bandwidth, and 40x voltage gain. The amplified output was recorded on a sampling digital oscilloscope (Model DSO5054A, Agilent, Inc., Santa Clara, CA).

2.3. Results

2.3.1. Preparation of Azide-Functionalized SnO_2 Surfaces

A key step in enabling the CuAAC reaction on metal oxides is the formation of either an azide or alkyne group on the surface. We chose to focus on preparing azide-modified SnO_2 surfaces because reduced risk with storing molecules bearing alkyne groups than molecules with azide groups (which are often explosive), and because alkyne-modified molecules are generally easier to obtain commercially. We prepared azide-functionalized SnO_2 nanocrystalline thin films via the three-step process shown in Figure 2.3.

The initial step involved the introduction of 3-buten-1-ol to the surface by a photochemical grafting reaction using 254 nm ultraviolet light (~10 mW/cm^2, 15 h) which yielded a high density of surface alcohol groups that are slightly removed from the bare SnO_2 surface. We choose to use the photochemical grafting of alkenes because it has been shown to yield highly stable molecular layers on surfaces of TiO_2[50] and other oxides.[51] Although the grafting mechanism has not been fully elucidated, studies to date suggest that photoexcited surface −OH groups act as hole traps that facilitate nucleophilic attack by the organic alkene group to link the molecules to the surface.[50,52] The surface alcohol groups were then converted to methanesulfonyl ("mesyl") groups using methanesulfonyl chloride (MsCl) with triethylamine (NEt_3) in dichloromethane (DCM) (1:1:10) and allowed to react for 1 hour in an ice bath. The mesyl functional group provided an effective leaving group for azide termination.

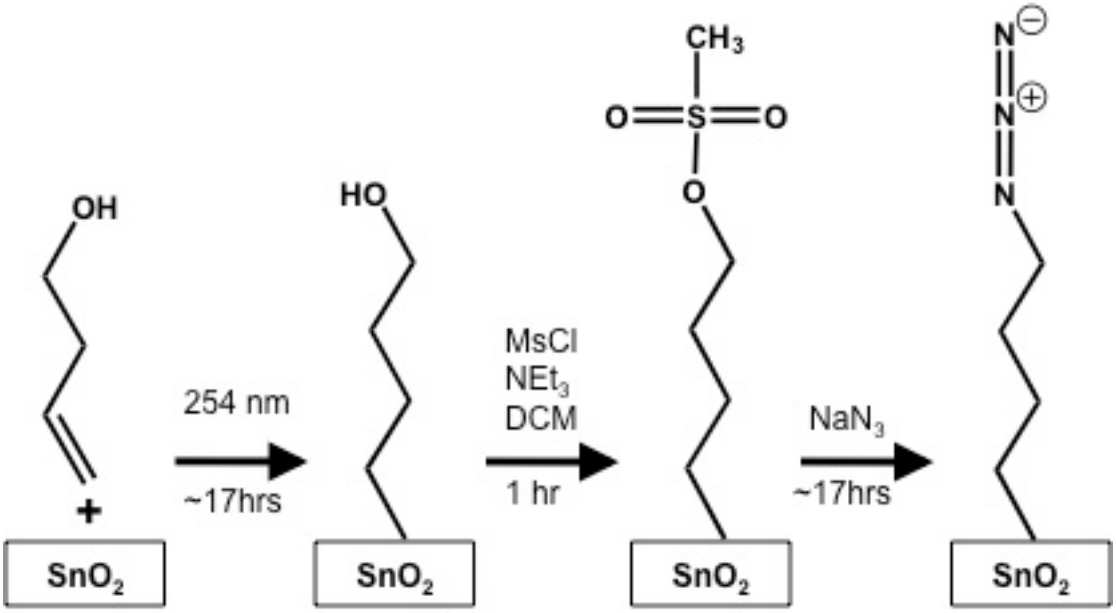

Figure 2.3: Reaction scheme for azide termination

Azide groups replaced the surface-bound mesyl groups by treatment with supersaturated NaN_3 in DMSO solution into vials that were crimp-sealed inside an Ar environment. The vials were then heated at 80°C for ~17 hours. Figure 2.4 shows the FTIR spectra of the sample after photochemical grafting with 3-butene-1-ol, after the mesylation step and after conversion to the azide. After grafting of 3-buten-1-ol the FTIR spectrum shows peaks at 2860 and 2923 cm^{-1} from the C-H vibrations of the grafted molecules and a large, broad –OH peak from ~3100-3400 cm^{-1}. After treatment with methylsulfonylchloride, the OH stretch is no longer present and two sharp peaks appear at 1174 and 1352 cm^{-1}. These frequencies attributed to the symmetric and asymmetric stretching vibrations of the SO_2 group. After treatment with NaN_3, the S=O stretches disappear and the spectrum shows a sharp feature at 2096 cm^{-1} from the azide group. A small OH peak is seen that most likely arises from adsorbed water after the NaN_3 reaction and subsequent rinsing. It is important to note that the CH_2 stretch is unchanged after each of the subsequent functionalizations, proof that the carbon chain remains intact and all reactions occur at the terminal functional group. To demonstrate successful “click” chemistry and to understand the applications to systems involving electrochemical and photoelectrochemical electron transfer, several molecules bearing an alkyne functional group were explored.

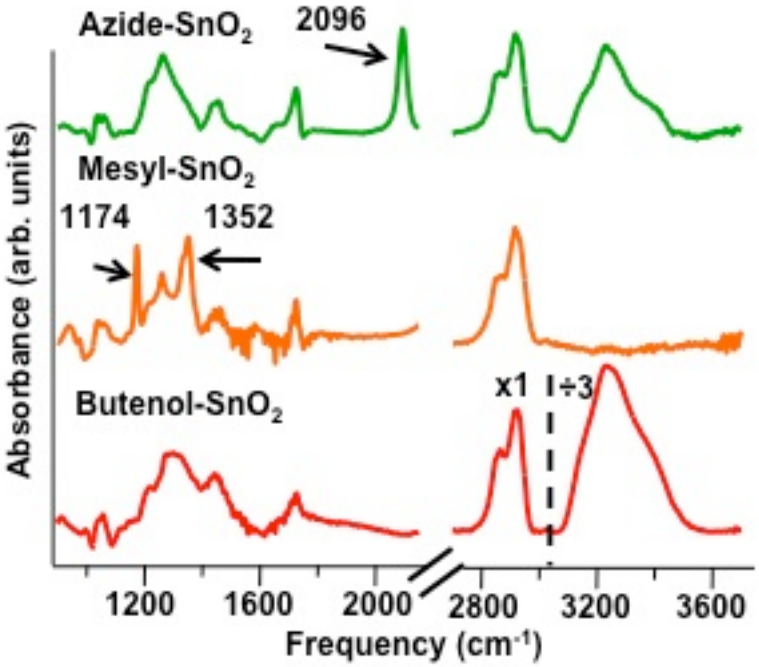

Figure 2.4: FTIR spectra of SnO_2 at different stages of functionalization of butenol grafted (bottom), mesyl terminated (middle), and azide terminated (top). Note: the intensity of 3000-3700 cm^{-1} containing O-H peak was reduced three-fold for butenol spectrum only.

2.3.2. Grafting of TFMPA to SnO_2 Surfaces

Since there has not been any previous studies demonstrating the use of CuAAC on metal oxide surfaces, a less complex compound was used to understand the reactivity of azide-modified surfaces. We used the compound 4-(trifluoromethoxy)phenylacetylene (TFMPA), which has a CF_3 group as a marker for XPS and FTIR analysis. TFMPA was linked to the SnO_2 surfaces as depicted in Figure 2.5, by submersing the azide-modified SnO_2 nanocrystalline thin film into a solution containing 0.5 mM Cu(II)(tris-(benzyltriazolyl-methyl)amine)$(BF_4)_2$ (henceforth referred to as TBTA), 1.0 mM of TFMPA, and 25 mM of sodium ascorbate in 3:1 (v:v) DMSO:H_2O for 17 h at room temperature. The samples were then rinsed sequentially with deionized H_2O, $CHCl_3$, and isopropyl alcohol (IPA). Experiments performed using shorter coupling times of 90 min and 5 h showed incomplete reaction, while the reaction was complete at 14 h. Reaction times of >14 h were used in all subsequent experiments. Similar reaction times have been used in previous studies of CuAAC reactions on azide-terminated silicon[32] and diamond[34] surfaces.

Figure 2.6 shows infrared spectra of an azide-modified SnO_2 surface, an azide-modified SnO_2 surface after the CuAAC reaction with TFMPA, and neat TFMPA. Figure 2.6a shows the entire region of interest, while Figure 2.6b is an enlarged view of the 1100–1600 cm^{-1} region.

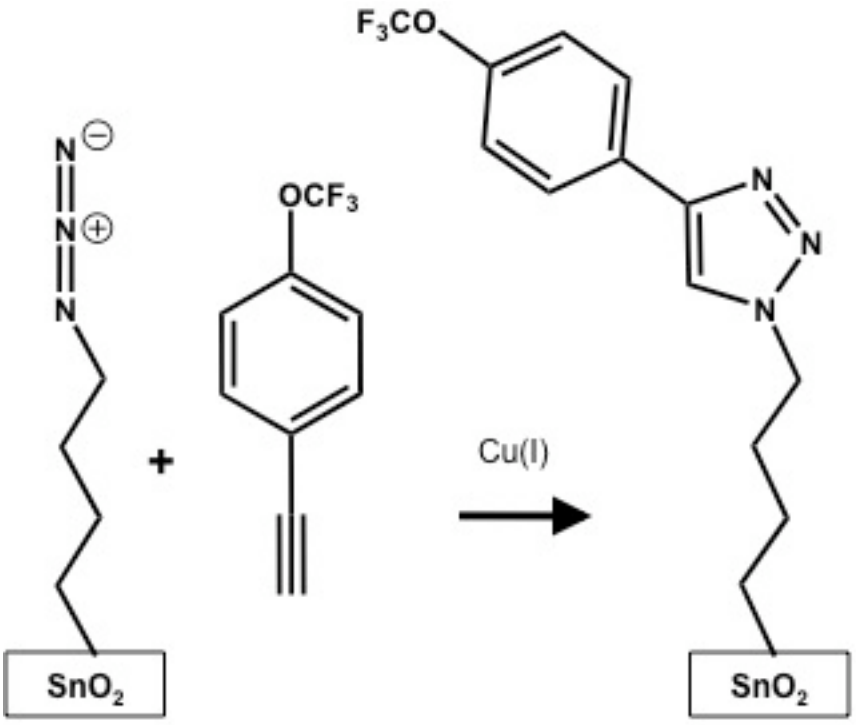

Figure 2.5: Reaction scheme of CuAAC reaction between azide-modified SnO_2 and TFMPA

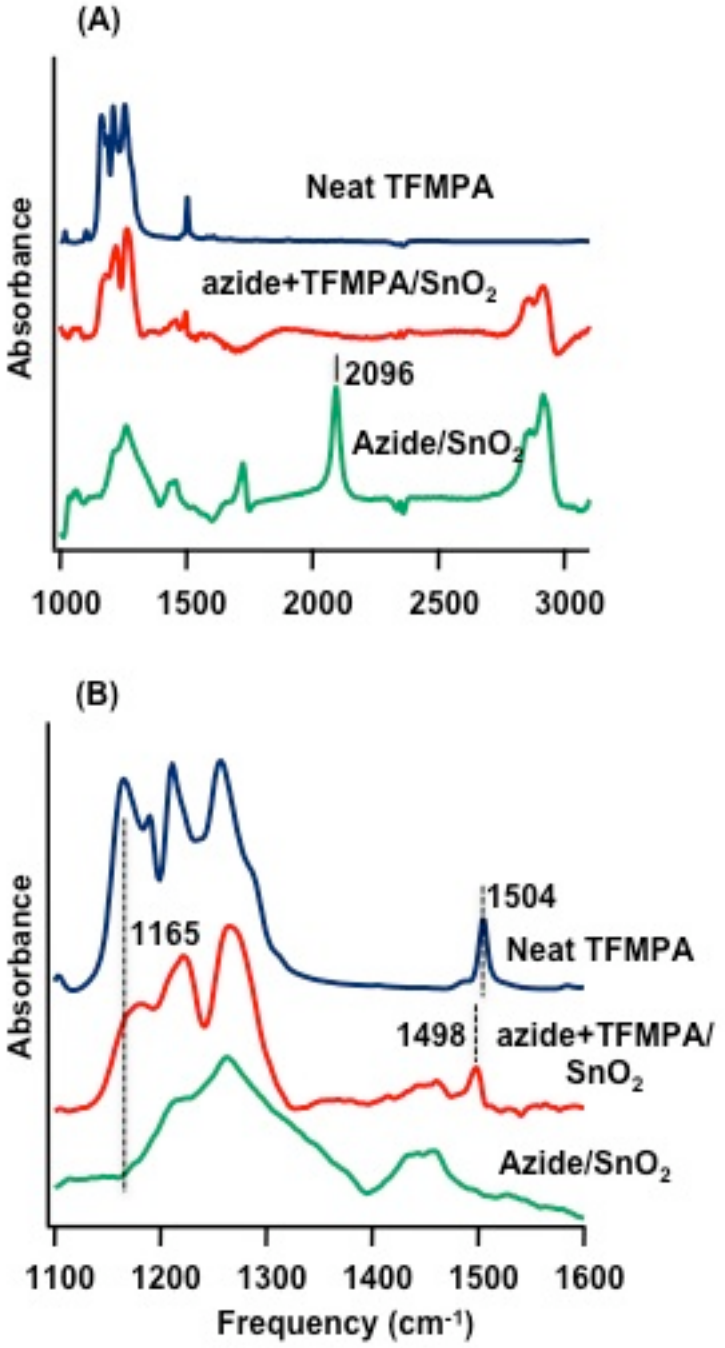

Figure 2.6: (A) FTIR spectra of Neat TFMPA, TFMPA-modified SnO_2 and azide-modified SnO_2 (B) FTIR enlarged view of 1100-1600 cm^{-1}

The azide-modified SnO_2 surface exhibits a very sharp peak at 2096 cm^{-1} that is characteristic of the symmetric stretch of the azide group, along with C–H modes at 2914 and 2860 cm^{-1} from the 3-buten-1-ol molecule. In addition, a broadened peak near 1261 cm^{-1} and a smaller peak near 1444 cm^{-1} arise from the alkyl chains of the butenol and lattice vibrations of SnO_2.

Finally, a sharp peak at 1724 cm^{-1} is observed, likely arising from the C═O stretch of adsorbed CO_2.[53] After CuAAC reaction with TFMPA, the azide peak is no longer present and three additional peaks appear at 1165, 1220, and 1265 cm^{-1}. These peaks are a clear superposition (with small shifts) of the triplet of C–F peaks from TFMPA at 1165, 1211, and 1255 cm^{-1}. The CuAAC-reacted sample also shows a peak at 1498 cm^{-1}; and neat TFMPA shows a similar peak shifted at 1504 cm^{-1} attributed to the aromatic ring.[54] The disappearance of the azide peak and appearance of the triplet associated with CF_3 indicates successful CuAAC reaction.

XPS was used to further verify successful CuAAC reaction. Figure 2.7 shows the C(1s), F(1s), and N(1s) regions of an azide-modified sample that was reacted with TFMPA in the presence of the Cu(I) catalyst along with results from two control samples. One control sample (“No Cu”) was carried through the entire procedure depicted in Figures 2.3 and 2.5 except the Cu catalyst was left out during the final step. A second control sample (“No azide”) was carried through the complete procedure except the mesylation/azidation sequence shown in Figure 2.3 was eliminated. If the reactions proceed as depicted in Figures 2.3 and 2.5, the “No azide” control should

correspond to the alcohol-terminated surface, whereas the “No Cu” control should correspond to the azide-terminated surface.

The “Full CuAAC” sample shows a single F(1s) peak at 689.3 eV from the $-CF_3$ group of TFMPA. The C(1s) spectrum shows a main peak at 284.4 eV, a shoulder at ~285.5 eV, and an isolated peak at 294.0 eV. The peak at 284.4 eV corresponds to non-oxidized carbon from the alkyl chain of the initial butenol layer and from the carbon atoms in the aromatic ring of TFMPA. The peak at 294.0 eV arises from C atoms in the CF_3 group of TFMPA, while the small shoulder at ~285.5 eV is consistent with C atoms adjacent to either N or O atoms which are both electron-withdrawing. Finally, the “Full CuAAC” sample shows two overlapping N(1s) peaks at 399.6 and 401.1 eV, similar to previous results of CuAAC reactions on surfaces [34,41] and correspond to the N atoms in the triazole ring. Thus, the “Full CuAAC” spectrum is fully consistent with the spectrum expected from the reaction depicted in Figure 2.5.

From the peak areas of F(1s) and Sn(3d) peak areas coverage of TFMPA can be estimated. Using an electron escape depth of ~2 nm in SnO_2 [55,56] and atomic sensitivity factors of 4.1 for the Sn ($3d_{5/2}$) peak and 1.0 for F(1s)[57] yields an coverage of ~1.7×10^{15} TFMPA molecules/cm^2 in the planar-sample limit. However, this value is larger than the true molecular coverage because the textured nature of the film surface increases the effective surface area and consequently the number of $-CF_3$ groups within the sampling area relative to the number of Sn atoms detected. Accurate determination of molecular coverage would require detailed modeling of electron emission and scattering in the nanoparticle film, but simple geometric arguments

indicate that the geometric corrections have a magnitude of approximately 2.[50] Thus, we estimate the true TFMPA coverage is on the order of 5×10^{14} to 1×10^{15} molecules/cm^2. Although the molecular coverage cannot be determined exactly, the values obtained are high and indicate that the molecules achieve dense packing on the surface.

Further confirmation that the surface grafting took place via the CuAAC reaction and not from non-specific binding comes from the control samples. The spectrum of the "No Cu" control sample shows no detectable fluorine and an N(1s) signal consisting of two peaks at 404.3 and 400.1 eV. The peak at 404.3 eV has a binding energy characteristic of the central N atom with the localized positive charge of the azide group.[58] The presence of this peak on the "No Cu" control but not on the "Full CuAAC" sample is strong evidence for reaction of the azide group with the alkyne group of TFMPA to form the triazole ring. The spectrum of the "No azide" sample shows no detectable F(1s) or N(1s) intensity but shows two C(1s) peaks: a main peak at 284.4 eV and a shoulder at 285.9 eV. The 284.4 eV peak arises from the alkyl chains while the 285.9 eV peak is consistent with that expected from C atoms of alcohol groups. From these control experiments it can be concluded that the absence of any F(1s) signal on the two control samples shows that there is no significant nonspecific binding of TFMPA to the surface. It can also be concluded that the CuAAC reaction requires the Cu(I) to catalyze the cycloaddition between the azide terminated nanocrystalline thin film SnO_2 and TFMPA. The XPS data are fully consistent with the FTIR data, and confirm the reaction proceeds as depicted in Figure 2.5.

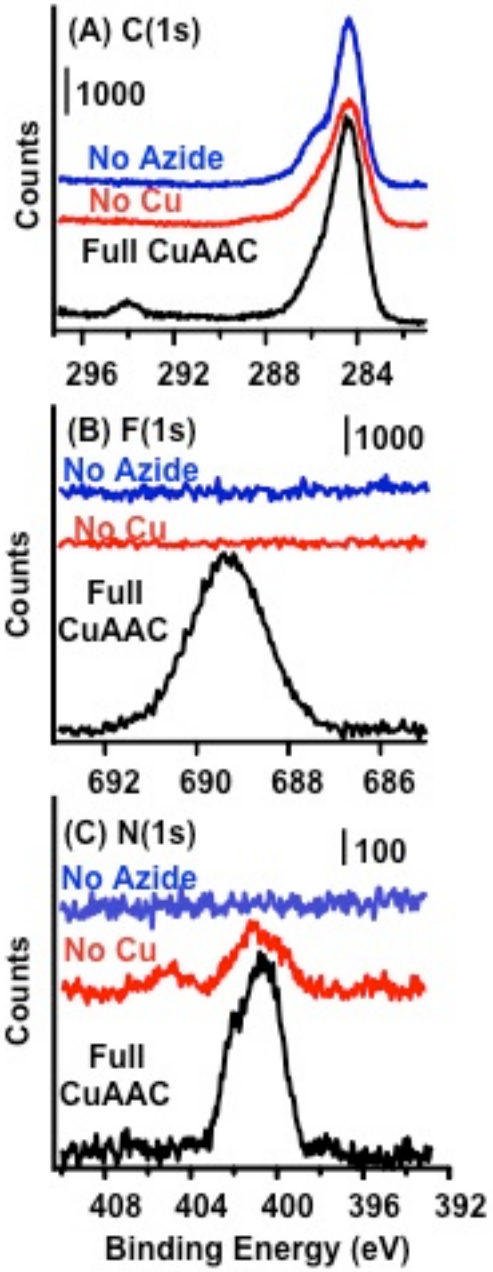

Figure 2.7: XPS spectra of (A) High-resolution scan of C(1s) region, (B) F(1s), and (C) N(1s) for no azide control (blue), no Cu control (red), and full CuAAC (or TFMPA modified) (black)

2.3.3. Formation and Characterization of Ferrocene-Modified SnO_2 Surfaces via CuAAC Reaction

The XPS and FTIR data of TFMPA-modified SnO_2 establishes the successful use of CuAAC chemistry to link model compounds to the surface. To test the generality of the method and reaction conditions, we tested the ability to make surface adducts with molecules that are expected to exhibit charge-transfer processes under electrochemical conditions. Ferrocene was chosen as a model system because previous studies based on the CuAAC, has been performed on carbon-based materials[36,41] and on self-assembled monolayers on gold.[35,37] Figure 2.8 depicts the binding of ethynylferrocene to the SnO_2 surface. In this case, the azide-modified SnO_2 thin films were immersed in a solution containing 3.8 mM ethynylferrocene, 8.0 mM sodium ascorbate, 0.4 mM $Cu(BF_4)_2$, and 0.1 mL of triethylamine in 3:1 (v:v) DMSO:H_2O. The reaction was carried out at room temperature for 17 h, and the sample was then rinsed sequentially with MeOH, $CHCl_3$, and IPA.

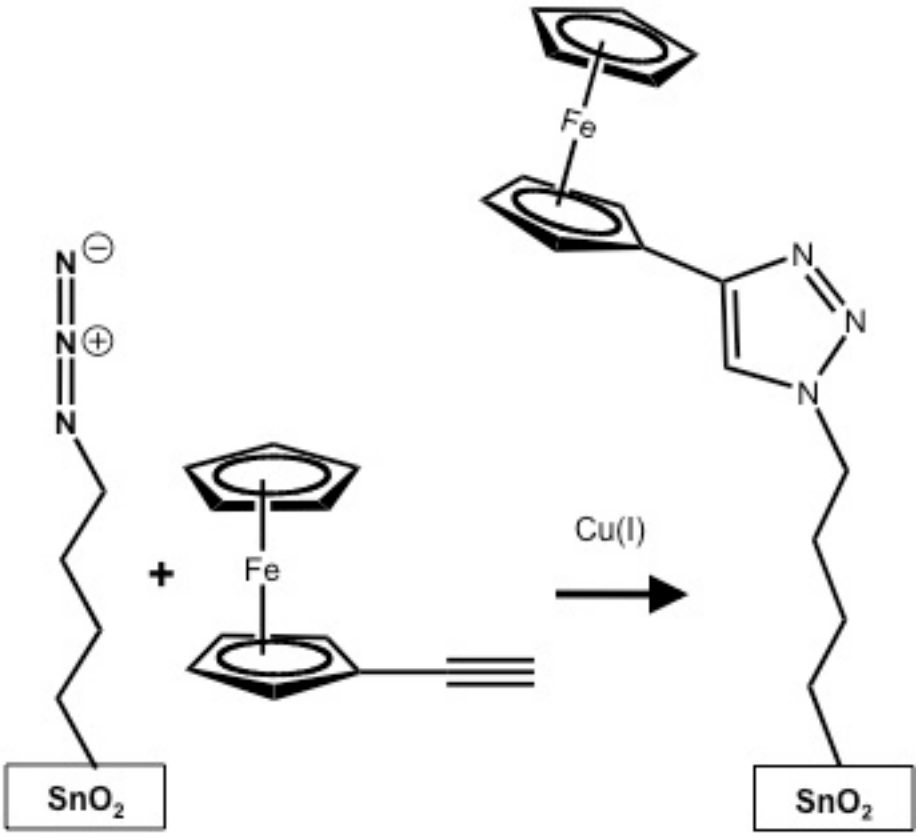

Figure 2.8: CuAAC reaction between azide-modified SnO_2 and ethynylferrocene

Figure 2.9a shows the FTIR spectra of the azide-modified SnO_2 surface before and after the CuAAC reaction with ethynylferrocene. After reaction with ethynylferrocene the 2100 cm^{-1} peak associated with the azide group, decreases almost completely, and a new sharp peak at 3103 cm^{-1} appears. The latter matches very well the 3106 cm^{-1} peak associated with the aromatic C–H modes of ferrocene vapor.[51] As compared to the previous results with TFMPA, the azide peak is not completely eliminated, suggesting the ethynylferrocene steric bulk does not allow for complete reaction with available azide groups but can pack sufficiently close together to allow for the majority of azide groups to be reacted.

XPS spectra were also obtained of the ferrocene-modified surface. The signature of surface-bound ferrocene is the appearance of a Fe ($2p_{3/2}$) peak in the XPS spectra near 709 eV, as shown in Figure 2.9b. This peak is weak and lies close to the larger Sn ($3p_{3/2}$) peak, but it is clearly visible on the sample exposed to the full CuAAC conditions and absent on the “No Cu” control sample where it was exposed to ethynylferrocene in the absence of Cu catalyst. The XPS and FTIR data strongly support the successful grafting of ferrocene groups to the SnO_2 surface through the same azide termination followed by CuAAC.

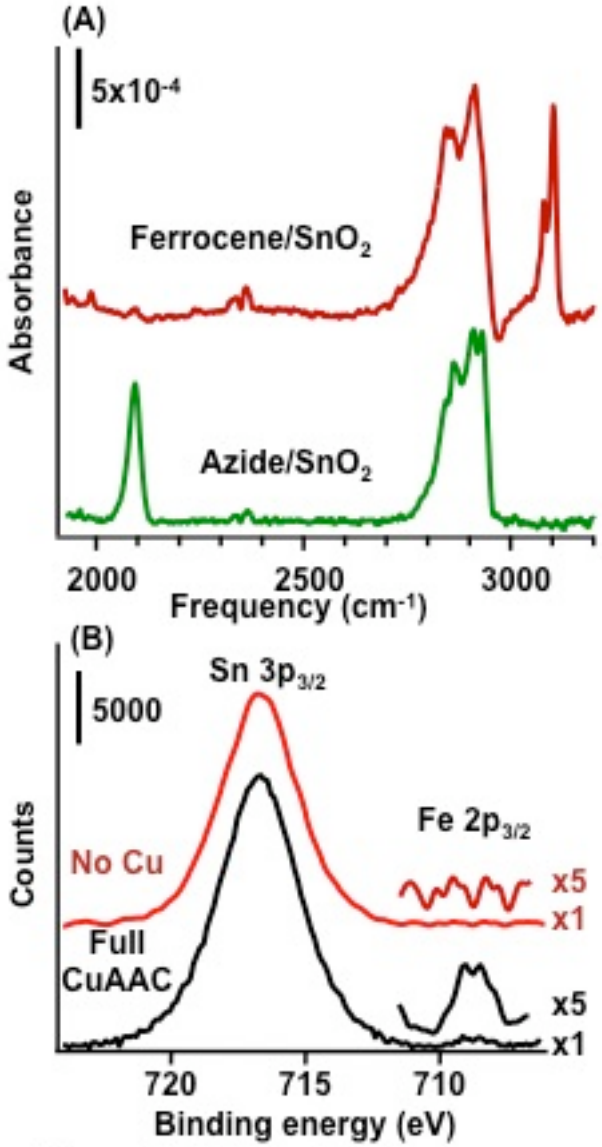

Figure 2.9: FTIR and XPS characterization of ferrocene-modified SnO2: (A) Infrared spectra of azide-modified SnO_2 thin film before and after CuAAC reaction with ethynylferrocene. (B) XPS spectra of sample exposed to full CuAAC condition, and control sample without Cu catalyst.

2.3.4. Electron-Transfer Properties of Ferrocene-Modified Layers

To determine if the ferrocene groups linked to SnO_2 are electrochemically active, cyclic voltammetry (CV) was performed at scan rates of 0.3 V/s, 1 V/s, 3 V/s, and 10 V/s in 1M $HClO_4$ as seen in Figure 2.10.[59] A "No Azide" control consisting of a butenol terminated SnO_2 exposed to full CuAAC reaction solution was also scanned. For a perfect redox-active monolayer on a metallic surface, the splitting between oxidized and reduced waves should approach zero at infinitely slow scan rate,[60,61] and the background from the (non-functionalized) electrode should be a simple trapezoid arising from the Helmholtz capacitance of the interface and uncompensated solution resistance. With semiconductors however, the space-charge layer and surface defects introduce additional resistance and capacitance components. These effects are particularly important for nanocrystalline semiconductor films because they have very high density of surface states.[62,63]

The CVs on the "no azide" control sample are similar to those reported previously on bare nanocrystalline films of SnO_2[64] and TiO_2.[63] Those studies showed that nanocrystalline SnO_2 and TiO_2 films have chloride impurities and bulk oxygen vacancy defects that create a band of unoccupied states in the bandgap.[64] The gap states give rise to an interfacial capacitance that is dependent on the sample potential and scan rate due to the distribution of energies extending from the conduction band edge into the band gap, [63] The scan rate dependent charging and discharging of the interfacial capacitance gives rise to the general shape of the background scans and is well described by these models.[63] It is important to note the "no azide" control sample does

not show any peaks that can be attributed to oxidation or reduction of ferrocene, however the azide-terminated surface that was exposed to CuAAC reaction conditions show clear oxidation and reduction peaks, similar to what has been observed on gold, at ~0.3-0.4 vs. Ag/AgCl. [65] These results confirm that the binding of ferrocene to the surface requires the presence of the surface azide group.

The electron-transfer properties of this system can be understood from analysis of the potentials at which the oxidation and reduction waves reach their maxima, obtained by subtracting the capacitive background from the oxidation and reduction waves at each scan rate. Figure 2.10e summarizes the potentials at which the oxidation and reduction peaks reached their maximum current. For a perfectly reversible system, zero splitting of the peaks would be observed, however ferrocene-modified SnO_2 shows a splitting between oxidation and reduction waves of ~50mV. This nonzero splitting indicates that the electron transfer is not fully reversible. At higher scan rates the splitting becomes larger, but in an asymmetric manner: the peak potential for the oxidation wave remains nearly constant while the potential of the reduction wave changes significantly with scan rate. A lower bound on the standard electrochemical charge-transfer rate k^0_{ct} can be estimated from the peak-to-peak splitting, ΔE_{pp}, and rate, R, as $k^0_{ct}=R/\Delta E_{pp}$. This value is a lower bound because it neglects other charge transfer processes that can limit the rate at which the surface potential changes, such as space-charge effects and/or charging of surface states. The 50 mV change in ΔE_{pp} as the scan rate is increased from 0 to 10 V/s yields a lower limit of $k^0_{ct}>1000\ s^{-1}$. The peak splitting we observe here is smaller than that observed in previous work linking

ferrocene to SnO_2 and TiO_2 via a phosphonic acid linkage, where a peak-to-peak splitting of ~400 mV was observed on SnO_2 and 390 mV on TiO_2.[27] The small value we observed here suggests that the CuAAC reaction substantially improves the electron communication between ferrocene and the underlying oxide surface compared with the approach employed previously. In repeated cycling, the cyclic voltammograms were extremely stable for more than 100 repeated cycles but eventually degraded, likely due to the inherent instability of SnO_2 in acidic conditions, as shown in Figure 2.11. Integration of the oxidation peak yields a total integrated charge of 2.2×10^{-5} Coulombs. Using the projected sample area, this corresponds to 5×10^{14} redox active ferrocene groups/cm^2. This value is at the lower end of the range of 5×10^{14} to 1×10^{15} molecules/cm^2 estimated from XPS studies of TFMPA, consistent with the slightly larger size of the ferrocene molecule and the presence of a small azide peak observed in FTIR.

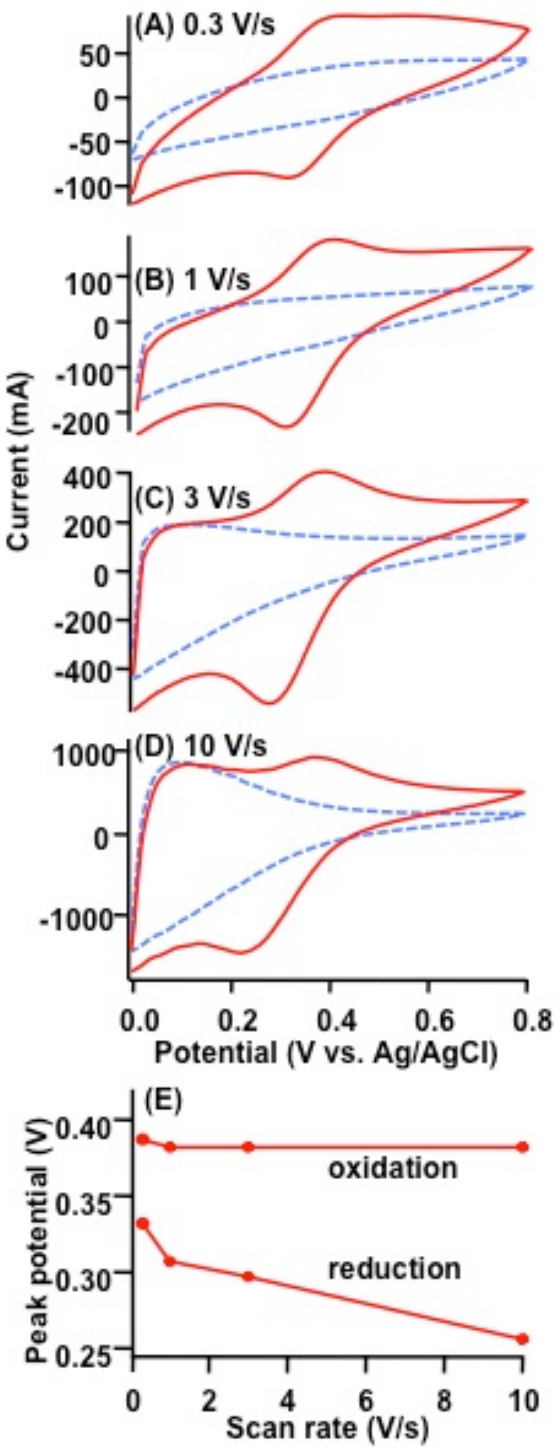

Figure 2.10: Cyclic voltammograms of bare (dashed lines) and ferrocene-functionalized (solid lines) SnO_2 nanocrystalline thin films. (A) 0.3 V/s, (B) 1 V/s, (C) 3V/s, and (D) 10 V/s. Panel (D) shows the peak potentials of the oxidation and reduction waves.

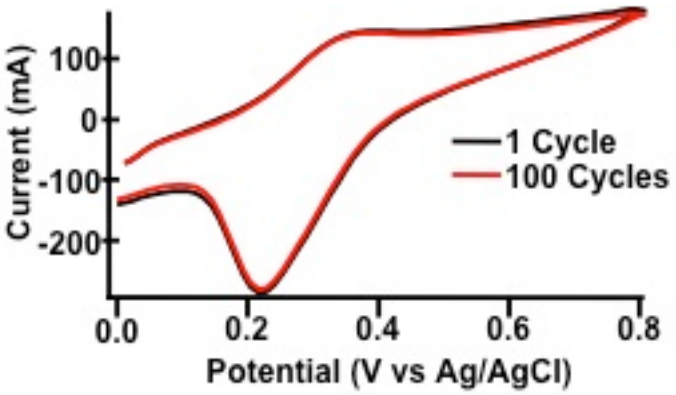

Figure 2.11: CV of 1st and 100th cycle of ferrocene modified SnO_2 at 1 V/s in 1M $HClO_4$

2.3.5. Photoelectrochemically Active Charge-Transfer Complex

To test whether the use of the CuAAC chemistry is capable of allowing surface-tethered molecules in excited electronic states to transfer electrons into the SnO_2 conduction band, a Ru-based coordination complex was used as shown in Figure 2.12. Ruthenium coordination complexes have attracted wide attention for their unique photophysical properties.[10,66] The alkyne-modified coordination complex $[Ru(tpy)(tpy')]^2$ was tethered to the azide-modified SnO_2 by immersing the samples into a solution of 100 μM $[Ru(tpy)(tpy')]^{2+}$, 0.8 mM CuTBTA, and 15 mM sodium ascorbate in 3:1 (v:v) DMSO:H_2O for 18 h at room temperature. The samples were rinsed sequentially with MeOH, $CHCl_3$, and IPA.

FTIR analysis shown in Figure 2.13a show reduction of the azide peak at 2100 cm^{-1} suggesting the steric interactions limit the efficiency of CuAAC reaction on the surface of SnO_2. XPS data shown in Figure 2.13b and 2.13c provide evidence for functionalization of the azide-modified SnO_2 surface with the $[Ru(tpy)(tpy')]^{2+}$ complex. The $Ru(3d_{5/2})$ peak is close to the primary C(1s) peak at 284.4 eV overlapping with the $3d_{3/2}$ spin–orbit component that should be 2/3 the intensity of the $3d_{5/2}$ component seen at 280 eV. The N(1s) peaks show the characteristic changes expected from the azide functionalization step and subsequent CuAAC reaction.

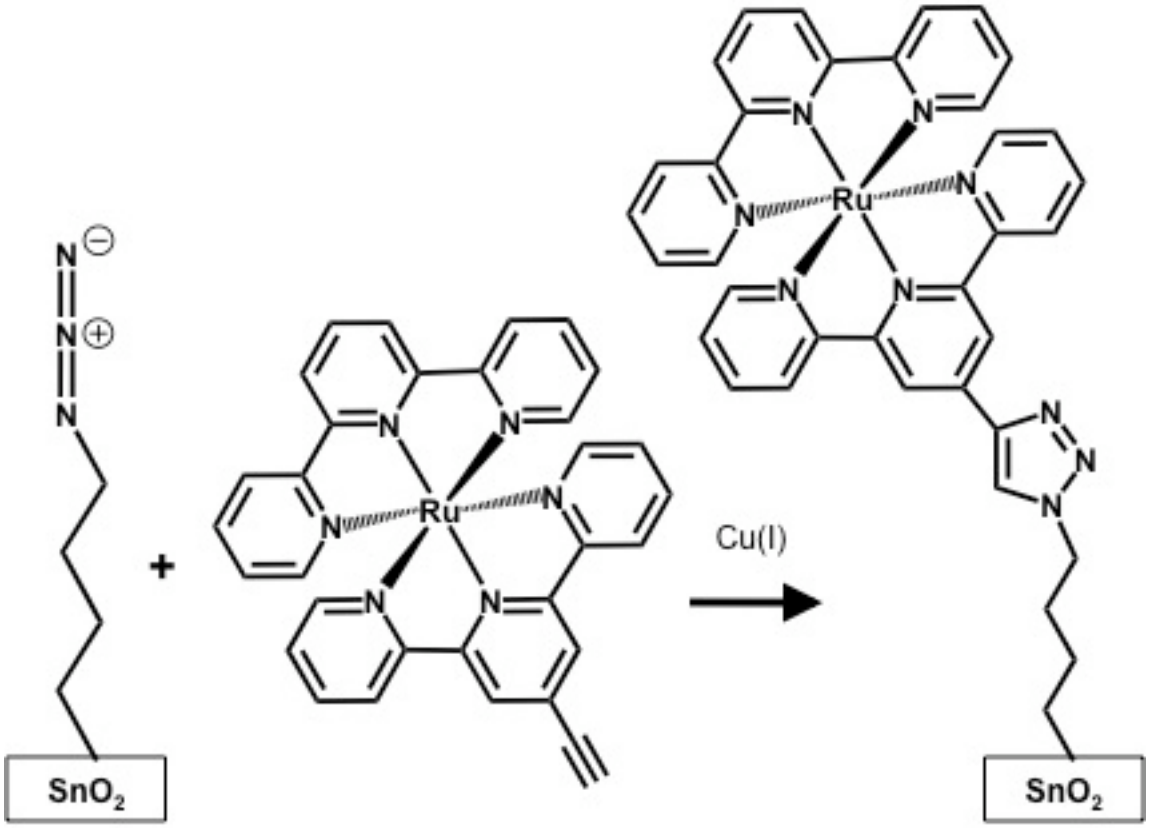

Figure 2.12: Reaction scheme of CuAAC reaction of azide-modified SnO_2 with $[Ru(tpy)(tpy')]^{2+}$

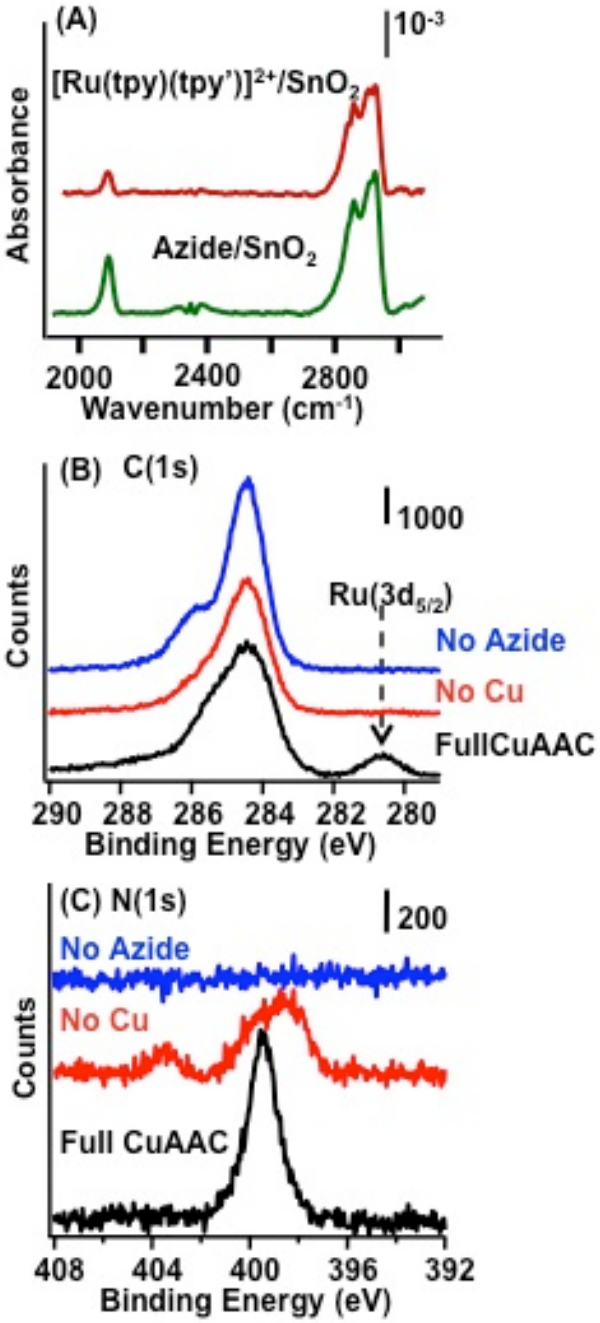

Figure 2.13: (A) FTIR of aizde-SnO_2 before and after CuAAC reaction with $[Ru(tpy)(tpy)]^{2+}$ (B) XPS high resolution scan of the C(1s) and $Ru(3d_{5/2})$ peaks for $[Ru(tpy)(tpy)]^{2+}$, and control experiments. The $Ru(3d_{3/2})$ peak lies under the C(1s) peak and should be 2/3 the intensity of the $Ru(3d_{5/2})$ peak (C) N(1s) spectrum of grafted sample and controls.

Figure 2.14a shows optical absorption spectra of the $[Ru(tpy)(tpy')]^{2+}$ complex in DMSO and a measurement made in transmission mode of the complex linked to the SnO_2 surfaces. The spectrum of $[Ru(tpy)(tpy')]^{2+}$ in DMSO has a maximum at 487 nm and appears similar to that reported previously for the unmodified $[Ru(tpy)_2]^{2+}$ in acetone and in acetonitrile.[67,68] The spectrum of the $[Ru(tpy)(tpy')]^{2+}$ bound to SnO_2 shows a peak at 496 nm that is slightly broadened and red-shifted compared to the $[Ru(tpy)(tpy')]^{2+}$ in DMSO. This shift is attributed to the additional delocalization of the electrons onto the triazole ring and is indicative of covalent bond formation. The excitation spectrum of $[Ru(tpy)(tpy')]^{2+}$ in DMSO at an emission wavelength of 680 nm shows a more complex spectrum, with a broad but structured peak at 505 nm, and additional peaks at 290 and 405 nm. The emission spectrum with excitation at 480 nm shows a maximum at 660 nm.

To characterize the charge injection of the $[Ru(tpy)(tpy')]^{2+}$ complex into the nanocrystalline SnO_2 thin film conduction band, time-resolved surface photovoltage (TR-SPV) measurements were performed. Figure 2.15a depicts the TR-SPV apparatus. Figure 2.15b and Figure 2.15c show the resulting TR-SPV transients measured at different wavelengths for the bare SnO_2 surface and $[Ru(tpy)(tpy')]^{2+}$ bound to the SnO_2 surface, respectively. A constant energy of 600 μJ/pulse and 20 Hz pulse rate were used. The bare SnO_2 surface shows no significant response in most of the visible region, although there is a small response at the shortest wavelengths. The $[Ru(tpy)(tpy')]^{2+}/SnO_2$ sample generates a much larger transient SPV response that

reaches a maximum at 490nm, close to where the absorption and fluorescence excitation spectra exhibit maxima. The positive sign of the transients corresponds to injection of electrons from the molecule into the SnO_2 surface, which leaves the surface with a transient positive charge that the sense electrode then polarizes to a negative charge. The time-resolved signal shows a fast rise and an almost equally fast fall time, both corresponding to the ~3 ns width of the incident laser pulse.

Since the rapid rise and decay are close to the bandwidth limits of the detection electronics, it is not possible to determine precise electron injection kinetics. However, the results demonstrate that optical excitation does induce significant charge transfer and that measurable charge transfer takes place on time scales of ≈3 ns or less. Literature reports the parent $Ru(tpy)_2^{2+}$ complex has an excited state lifetime of 250 ps at room temperature.[69]

Figure 2.15d shows normalized peak intensities versus wavelength, in which the peak amplitudes from Figure 2.15c have been normalized to represent the SPV generated per incident photon. This wavelength dependence appears similar to that of the UV–visible absorption spectrum in Figure 2.14a suggesting that all wavelengths capable of being absorbed are also able to inject electrons from the molecule into the SnO_2.

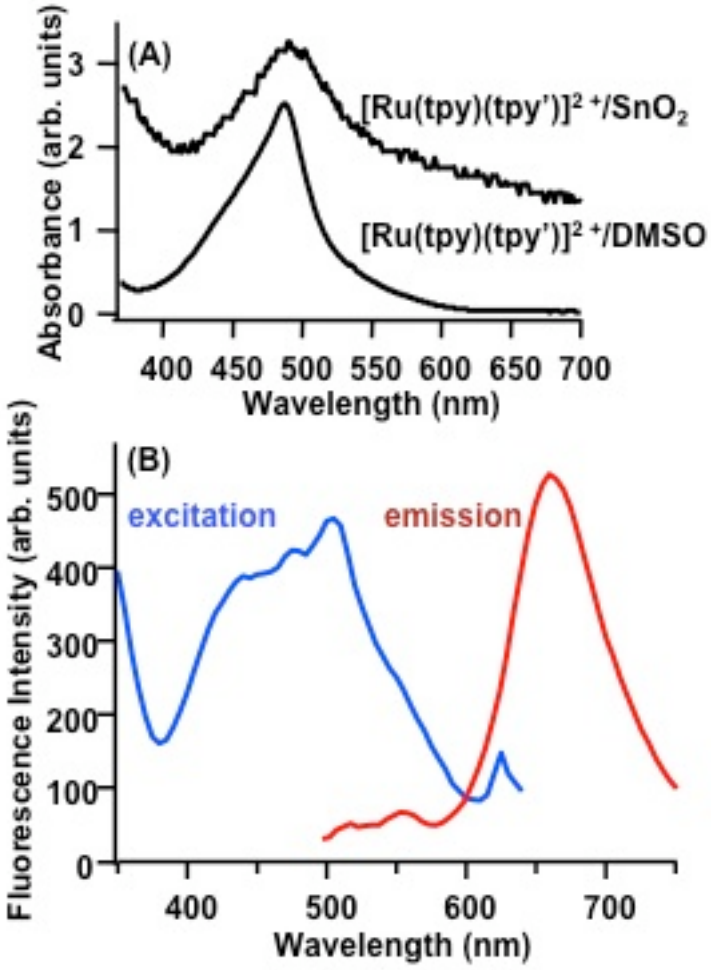

Figure 2.14: (A) Absorption spectrum of $[Ru(tpy)(tpy)]^{2+}$ grafted onto SnO_2 surface and solution-phase absorption spectrum of $[Ru(tpy)(tpy')]^{2+}$ in DMSO. The spectra have been scaled individually; the spectrum on SnO_2 has been shifted upward for clarity. (B) Fluorescence emission spectrum (480 nm excitation and fluorescence excitation spectrum (680 nm emission) of $[Ru(tpy)(tpy')]^{2+}$ in DMSO.

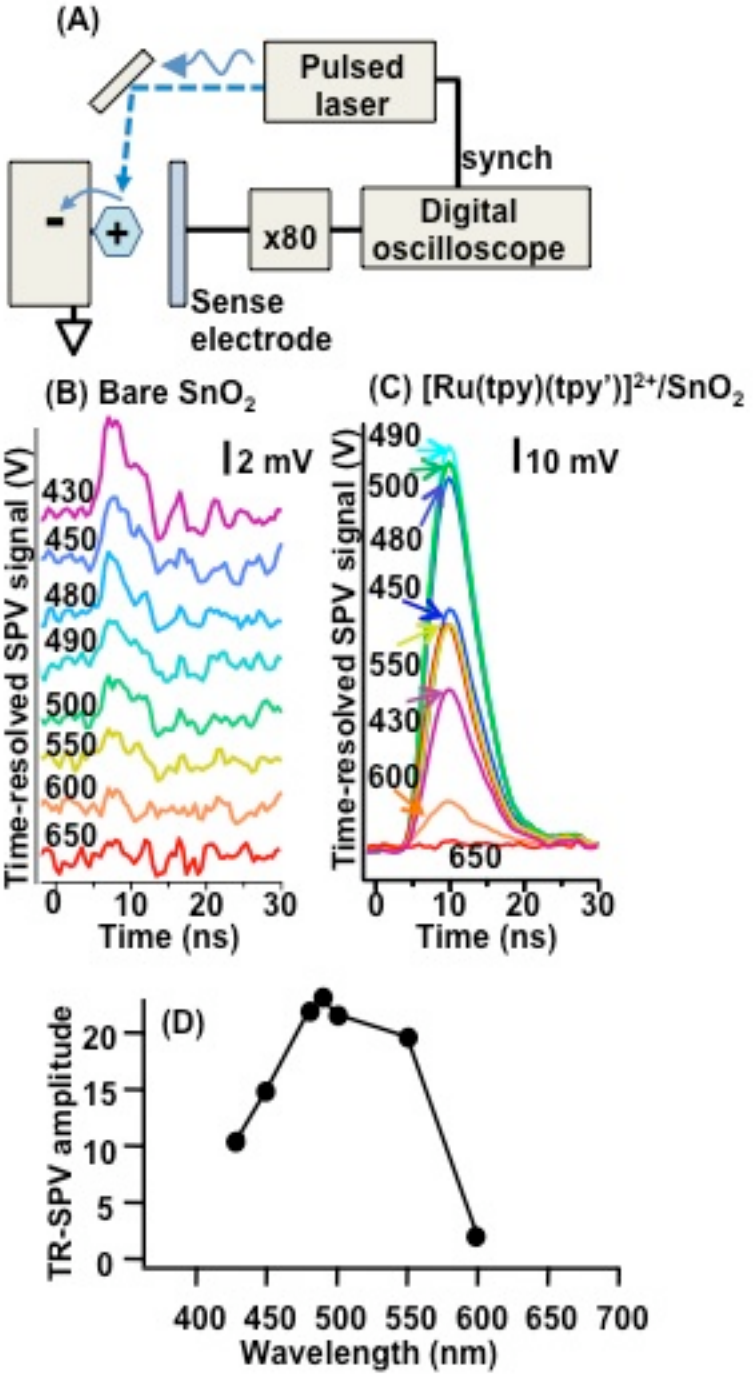

Figure 2.15: (A) Schematic illustration of apparatus (B) TR-SPV data from bare SnO_2 at different wavelengths (C) TR-SPV data from SnO_2 after CuAAC with $[Ru(tpy)(tpy')]^{2+}$ (D) Wavelength dependence of TR-SPV signal amplitude normalized by photon energy

2.4. Discussion

These results demonstrate that photochemical grafting as a multi-step pathway for producing azide-modified SnO_2 thin films can be combined the CuAAC "click" reaction and provides a versatile method to tether electrochemically and photoelectrochemically active molecules to SnO_2. The ability to transfer charge across molecular interfaces is central to the use of molecular adducts in applications such as photovoltaic devices and photocatalysis. Our results suggest that the methods described here may be promising for these and other emerging applications.

Our approach to functionalization involves the use of a short molecular linker (3-buten-1-ol) that provides a high density of surface alcohol groups that are slightly removed from the surface. By using a short spacer to move the −OH groups slightly away from the metal oxide surface we enable a wide range of organic chemistry reactions, such as the CuAAC reaction, to be used in subsequent transformations. This approach enables the surface-attachment chemistry to be optimized independently of the synthesis of redox- and photoactive molecular species.

One potentially adverse effect of this two-step chemistry is that the use of a molecular tether reduces the direct electronic coupling between the appended electron-injector groups and the metal oxide surfaces. To optimize electron transfer it may be desirable to link molecules to the surface using completely conjugated linkages. Recent studies on metals,[70-72] carbon nanostructures,[41,72] and conductive diamond[34] have shown that electron transfer in disordered molecular systems can be surprisingly facile,

even when alkyl chains and/or other nonconductive groups are included in the molecular chains. This enhanced electron transfer has been attributed to the increased conformational flexibility of loosely tethered molecules, which allows a closer approach of the molecule to the underlying substrate than would be the case for a densely packed self-assembled monolayer.[34,41,70-74] This property is further supported by previous studies of electron transfer in proteins[75] and in DNA layers on surfaces.[70,71,75]

Although extraction of quantitative rates from the ferrocene/SnO_2 data is complicated by the convolution of electron transfer and charge trapping/detrapping processes in SnO_2 gap states, our data with ferrocene suggests that thermal electron transfer takes place with a standard rate constant of >1000 s^{-1}, and our data for $[Ru(tpy)(tpy')]^{2+}$ indicate that photoexcited electron transfer can take place on time scales of 3 ns or less from excited electronic states. Thus, we conclude that the use of "click" chemistry as outlined here can be used as a way to link a diverse range of electrochemically and photoelectrochemically active groups to metal oxide surfaces while still maintaining desirable electron transfer properties. Additional studies will be required to fully characterize the rates and mechanisms of electron transfer.

2.5. Conclusions

Our results demonstrate a modular approach to the functionalization of metal oxide surfaces to yield electrochemically and photoelectrochemically active surfaces. Photochemical grafting of a short molecular layer provides a convenient means to produce a high density of alcohol groups slightly separated from the highly ionic and

reactive metal oxide surface. Therefore, subsequent steps, including conversion of surface −OH groups to surface azides, can be carried out without interference from the underlying metal oxide. The azide-modified surface is then able to undergo the Cu(I)-catalyzed azide–alkyne [3 + 2] cycloaddition “click” reaction to form electrochemically and photoelectrochemically active metal oxide surfaces, demonstrated here through the model systems of ethynylferrocene and $[Ru(tpy)(tpy')]^{2+}$. Although alkyl chains such as the short 3-buten-1-ol as the initial functionalization layer are often considered to be insulating, our results show that surface-tethered species such as ferrocene and $[Ru(tpy)(tpy')]^{2+}$ can undergo facile electron transfer to the metal oxides. Our results suggest that this method provides versatile and convenient pathway toward the formation of hybrid interfaces of metal oxides with organic molecules for potential applications in renewable energy.

2.6. References

(1) Argazzi, R.; Bignozzi, C. A.; Heimer, T. A.; Castellano, F. N.; Meyer, G. J. *Inorganic Chemistry* 1994, *33*, 5741.

(2) Bouclé, J.; Ravirajan, P.; Nelson, J. *Journal of Materials Chemistry* 2007, *17*, 3141.

(3) Grätzel, M. *Journal of Photochemistry and Photobiology C-Photochemistry Reviews* 2003, *4*, 145.

(4) Haick, H.; Hurley, P. T.; Hochbaum, A. I.; Yang, P.; Lewis, N. S. *Journal of the American Chemical Society* 2006, *128*, 8990.

(5) Kim, J. Y.; Kim, S. H.; Lee, H. H.; Lee, K.; Ma, W.; Gong, X.; Heeger, A. J. *Advanced Materials* 2006, *18*, 572.

(6) O'Regan, B.; Gratzel, M. *Nature* 1991, *353*, 737.

(7) Chen, Z. F.; Concepcion, J. J.; Hull, J. F.; Hoertz, P. G.; Meyer, T. J. *Dalton Transactions* 2010, *39*, 6950.

(8) Chen, Z. F.; Concepcion, J. J.; Jurss, J. W.; Meyer, T. J. *Journal of the American Chemical Society* 2009, *131*, 15580.

(9) Chen, Z. F.; Concepcion, J. J.; Luo, H. L.; Hull, J. F.; Paul, A.; Meyer, T. J. *Journal of the American Chemical Society* 2010, *132*, 17670.

(10) Ischay, M. A.; Anzovino, M. E.; Du, J.; Yoon, T. P. *Journal of the American Chemical Society* 2008, *130*, 12886.

(11) McNamara, W. R.; Milot, R. L.; Song, H.-e.; Snoeberger Iii, R. C.; Batista, V. S.; Schmuttenmaer, C. A.; Brudvig, G. W.; Crabtree, R. H. *Energy & Environmental Science* 2010, *3*, 917.

(12) Woodhouse, M.; Parkinson, B. A. *Chemical Society Reviews* 2009, *38*, 197.

(13) Batzill, M.; Diebold, U. *Progress in Surface Science* 2005, *79*, 47.

(14) Ford, W. E.; Rodgers, M. A. J. *Journal of Physical Chemistry* 1994, *98*, 3822.

(15) Ford, W. E.; Wessels, J. M.; Rodgers, M. A. J. *Journal of Physical Chemistry B* 1997, *101*, 7435.

(16) Fungo, F.; Otero, L.; Durantini, E. N.; Silber, J. J.; Sereno, L. E. *Journal of Physical Chemistry B* 2000, *104*, 7644.

(17) Gubbala, S.; Chakrapani, V.; Kumar, V.; Sunkara, M. K. *Advanced Functional Materials* 2008, *18*, 2411.

(18) Gubbala, S.; Russell, H. B.; Shah, H.; Deb, B.; Jasinski, J.; Rypkema, H.; Sunkara, M. K. *Energy & Environmental Science* 2009, *2*, 1302.

(19) Hawn, D. D.; Armstrong, N. R. *Journal of Physical Chemistry* 1978, *82*, 1288.

(20) Kay, A.; Gratzel, M. *Chemistry of Materials* 2002, *14*, 2930.

(21) Osa, T.; Fujihira, M. *Nature* 1976, *264*, 349.

(22) Park, N. G.; Kang, M. G.; Ryu, K. S.; Kim, K. M.; Chang, S. H. *Journal of Photochemistry and Photobiology a-Chemistry* 2004, *161*, 105.

(23) Korotkov, R. Y.; Farran, A. J. E.; Culp, T.; Russo, D.; Roger, C. *Journal of Applied Physics* 2004, *96*, 6445.

(24) Sanjinés, R.; Demarne, V.; Lévy, F. *Thin Solid Films* 1990, *193*, 935.

(25) Könenkamp, R. *Physical Review B* 2000, *61*, 11057.

(26) Wang, Y.-F.; Li, J.-W.; Hou, Y.-F.; Yu, X.-Y.; Su, C.-Y.; Kuang, D.-B. *Chemistry-a European Journal* 2010, *16*, 8620.

(27) Frantz, R.; Durand, J. O.; Lanneau, G. F.; Jumas, J. C.; Olivier-Fourcade, J.; Cretin, M.; Persin, M. *European Journal of Inorganic Chemistry* 2002, 1088.

(28) Houamer-Rassin, C.; Chaignon, F.; She, C.; Stockwell, D.; Blart, E.; Buvat, P.; Lian, T.; Odobel, F. *Journal of Photochemistry and Photobiology a-Chemistry* 2007, *192*, 56.

(29) Ryan, M. A.; Spitler, M. T. *Langmuir* 1988, *4*, 861.

(30) Marrani, A. G.; Cattaruzza, F.; Decker, F.; Zanoni, R.; Cossi, M.; Iozzi, M. F. *Journal of Nanoscience and Nanotechnology* 2010, *10*, 2901.

(31) Plass, K. E.; Liu, X.; Brunschwig, B. S.; Lewis, N. S. *Chemistry of Materials* 2008, *20*, 2228.

(32) Rohde, R. D.; Agnew, H. D.; Yeo, W.-S.; Bailey, R. C.; Heath, J. R. *Journal of the American Chemical Society* 2006, *128*, 9518.

(33) Das, M. R.; Wang, M.; Szunerits, S.; Gengembre, L.; Boukherroub, R. *Chemical Communications* 2009, 2753.

(34) Ruther, R. E.; Rigsby, M. L.; Gerken, J. B.; Hogendoorn, S. R.; Landis, E. C.; Stahl, S. S.; Hamers, R. J. *Journal of the American Chemical Society* 2011, *133*, 5692.

(35) Devaraj, N. K.; Decreau, R. A.; Ebina, W.; Collman, J. P.; Chidsey, C. E. D. *Journal of Physical Chemistry B* 2006, *110*, 15955.

(36) Devadoss, A.; Chidsey, C. E. D. *Journal of the American Chemical Society* 2007, *129*, 5370.

(37) Collman, J. P.; Devaraj, N. K.; Chidsey, C. E. D. *Langmuir* 2004, *20*, 1051.

(38) Hein, J. E.; Fokin, V. V. *Chemical Society Reviews* 2010, *39*, 1302.

(39) Kolb, H. C.; Finn, M. G.; Sharpless, K. B. *Angewandte Chemie-International Edition* 2001, *40*, 2004.

(40) Rostovtsev, V. V.; Green, L. G.; Fokin, V. V.; Sharpless, K. B. *Angewandte Chemie-International Edition* 2002, *41*, 2596.

(41) Landis, E. C.; Hamers, R. J. *Chemistry of Materials* 2009, *21*, 724.

(42) Tan, E. T. H.; Ho, G. W.; Wong, A. S. W.; Kawi, S.; Wee, A. T. S. *Nanotechnology* 2008, *19*.

(43) Ito, S.; Murakami, T. N.; Comte, P.; Liska, P.; Graetzel, C.; Nazeeruddin, M. K.; Graetzel, M. *Thin Solid Films* 2008, *516*, 4613.

(44) Ziessel, R.; Grosshenny, V.; Hissler, M.; Stroh, C. *Inorganic Chemistry* 2004, *43*, 4262.

(45) Conny, J. M.; Powell, C. J. *Surface and Interface Analysis* 2000, *29*, 856.

(46) Shirley, D. A. *Physical Review B* 1972, *5*, 4709.

(47) Mora-Séro, I.; Dittrich, T.; Garcia-Belmonte, G.; Bisquert, J. *Journal of Applied Physics* 2006, *100*.

(48) Anta, J. A.; Mora-Seró, I.; Dittrich, T.; Bisquert, J. *Journal of Physical Chemistry C* 2007, *111*, 13997.

(49) Kronik, L.; Leibovitch, M.; Fefer, E.; Burstein, L.; Shapira, Y. *Journal of Electronic Materials* 1995, *24*, 379.

(50) Franking, R. A.; Landis, E. C.; Hamers, R. J. *Langmuir* 2009, *25*, 10676.

(51) Hamers, R. J.; Chambers, S. A.; Evans, P. E.; Franking, R.; Gerbec, Z.; Gopalan, P.; Kim, H.; Landis, E. C.; Li, B.; McCoy, M. W.; Ohsawa, T.; Ruther, R. *physica status solidi (c)* 2010, *7*, 200.

(52) Li, B.; Franking, R.; Landis, E. C.; Kim, H.; Hamers, R. J. *Acs Applied Materials & Interfaces* 2009, *1*, 1013.

(53) Amalric-Popescu, D.; Bozon-Verduraz, F. *Catalysis Today* 2001, *70*, 139.

(54) Shishkov, I. F.; Geise, H. J.; Van Alsenoy, C.; Khristenko, L. V.; Vilkov, L. V.; Senyavian, V. M.; Van der Veken, B.; Herrebout, W.; Lokshin, B. V.; Garkusha, O. G. *Journal of Molecular Structure* 2001, *567*, 339.

(55) Nagata, T.; Bierwagen, O.; White, M. E.; Tsai, M. Y.; Yamashita, Y.; Yoshikawa, H.; Ohashi, N.; Kobayashi, K.; Chikyow, T.; Speck, J. S. *Applied Physics Letters* 2011, *98*.

(56) Wagner, C. D.; Naumkin, A. V.; Kraut-Vass, A.; Allison, J. W.; Powell, C. J.; Rumble, J. R., Jr *NIST X-ray Photoelectron Spectroscopy Database*; National Institue of Standards and Technology: Gaithersburg, MD, 2003; Vol. Version 3.5.

(57) Moulder, J. F.; Stickle, W. F.; Sobol, P. E.; Bomben, K. D. *Handbook of X-ray Photoelectron Spectroscopy*; Perkin-Elmer Corporation: Eden Prarie, MN, 1992.

(58) Collman, J. P.; Devaraj, N. K.; Eberspacher, T. P. A.; Chidsey, C. E. D. *Langmuir* 2006, *22*, 2457.

(59) Popenoe, D. D.; Deinhammer, R. S.; Porter, M. D. *Langmuir* 1992, *8*, 2521.

(60) Laviron, E. *Journal of Electroanalytical Chemistry* 1979, *101*, 19.

(61) Murray, R. W. *Electroanalytical Chemistry* 1984, *13*, 191.

(62) Bisquert, J.; Zaban, A.; Salvador, P. *Journal of Physical Chemistry B* 2002, *106*, 8774.

(63) Fabregat-Santiago, F.; Mora-Sero, I.; Garcia-Belmonte, G.; Bisquert, J. *Journal of Physical Chemistry B* 2003, *107*, 758.

(64) Kim, H.; Laitinen, H. A. *Journal of the Electrochemical Society* 1975, *122*, 53.

(65) Creager, S. E.; Rowe, G. K. *Analytica Chimica Acta* 1991, *246*, 233.

(66) Campagna, S.; Puntoriero, F.; Nastasi, F.; Bergamini, G.; Balzani, V. In *Photochemistry and Photophysics of Coordination Compounds I*; Balzani, V., Campagna, S., Eds. 2007; Vol. 280, p 117.

(67) Jakubikova, E.; Chen, W.; Dattelbaum, D. M.; Rein, F. N.; Rocha, R. C.; Martin, R. L.; Batista, E. R. *Inorganic Chemistry* 2009, *48*, 10720.

(68) Sauvage, J. P.; Collin, J. P.; Chambron, J. C.; Guillerez, S.; Coudret, C.; Balzani, V.; Barigelletti, F.; Decola, L.; Flamigni, L. *Chemical Reviews* 1994, *94*, 993.

(69) Winkler, J. R.; Netzel, T. L.; Creutz, C.; Sutin, N. *Journal of the American Chemical Society* 1987, *109*, 2381.

(70) Anne, A.; Demaille, C. *Journal of the American Chemical Society* 2006, *128*, 542.

(71) Anne, A.; Demaille, C. *Journal of the American Chemical Society* 2008, *130*, 9812.

(72) Uzawa, T.; Cheng, R. R.; White, R. J.; Makarov, D. E.; Plaxco, K. W. *Journal of the American Chemical Society* 2010, *132*, 16120.

(73) Beratan, D. N.; Onuchic, J. N.; Hopfield, J. J. *Journal of Chemical Physics* 1987, *86*, 4488.

(74) Landis, E. C.; Klein, K. L.; Liao, A.; Pop, E.; Hensley, D. K.; Melechko, A. V.; Hamers, R. J. *Chemistry of Materials* 2010, *22*, 2357.

(75) Fan, C. H.; Plaxco, K. W.; Heeger, A. J. *Proceedings of the National Academy of Sciences of the United States of America* 2003, *100*, 9134.

Chapter 3

Versatility of CuAAC Reaction with A Ruthenium Coordination Complex to Yield Photoelectrochemically SnO_2 Nanorods and Electrocatalytically Active Fluorine-doped SnO_2 Electrodes

3.1. Introduction

Various morphologies of SnO_2 like nanorods and planar fluorine-doped SnO_2 electrodes have become materials of increasing interest for photovoltaic applications due to their high electron mobilities, low manufacturing costs, and ease in fabrication.[1-3] Although their use in photovoltaic devices has been investigated, there has been little progress in the engineering of stable interfaces between SnO_2 surfaces and a molecular species, such as a ruthenium based light absorber or water oxidation catalyst.[2-7] The interface between the molecular species and the semiconducting electrode governs many of the electron transfer processes that can limit the performance of photovoltaic devices, which necessitates the need for better control of the molecular tether.[8-10] Previous methods of anchoring molecular species to SnO_2 and other metal oxide surfaces have been dependent on linkages that are labile in aqueous conditions.[4-6,11,12] Recently, we have shown progress towards improving the interface between the SnO_2 surface and organometallic complex through the use of a modular attachment with the Cu(I) azide-alkyne cycloaddition (CuAAC) reaction.[13-16] A model ruthenium complex was anchored to the surface of nanocrystalline SnO_2 through a short alkyl chain with a terminal azide that was able to undergo CuAAC reaction with a modified ruthenium

complex with a ligand bearing a terminal alkyne. The modification produced a photoelectrochemically active surface upon excitation by visible light.[13] However, to elucidate the versatility of the CuAAC reaction with various SnO_2 surfaces we used a ruthenium coordination complex that was synthesized by our collaborators in Professor Thummel's lab at the University of Houston. The modular attachment of $[Ru(bpy)(tpy")Cl]^+$ (where bpy=2,2, bypridine and tpy"= 4'-(4-Ethynylphenyl)-2,2':6',2''-terpyridine) to both SnO_2 nanorods and fluorine-doped SnO_2 was investigated.

SnO_2 nanorods are an interesting morphology because of their ability to maintain high electron mobility compared to nanocrystalline thin films which can have reduced electron mobility arising from grain boundaries.[17] Additionally, the one-dimensional morphology of the nanorods is theorized to allow a direct pathway for the photoexcited electrons injected from a molecular absorber.[18,19] Recent progress in SnO_2 nanorods in DSSCs have shown several 100 mV increase in the V_{OC} as compared to SnO_2 nanocrystalline thin films.[20] However, these linkages still relay on electrostatic interactions that can easily become desorbed in aqueous conditions.[18,19] Another, morphology of SnO_2 that has shown great promise in emerging renewable energy technologies is planar fluorine-doped tin oxide electrodes.

Fluorine-doped tin oxide (FTO) is used in many renewable energy applications such as a support for immobilizing electrochemically active catalysts, termed a heterogeneous catalysis system.[11,21-25] An advantage for the immobilization of an electrochemically active catalyst is that the presence of a sacrificial agent, like Ce (IV), is not needed.[26] One method of anchoring active catalysts to FTO is to drop cast a

water insoluble compound onto the surface of the electrode, however the catalytically active layer can easily become detached during electrochemical activation of the catalyst.[6,11] Another approach is to use a phosphine group to anchor a catalyst to the surface of FTO, however the phosphine functional groups can become desorbed in aqueous conditions.[11,24,25] It is essential for a heterogeneous catalysis in renewable energy applications consist of linkages that are water stable without hindering electron transfer.[27] The work presented here will explore the versatility of the modular approach for attaching $[Ru(bpy)(tpy")Cl]^+$ to different SnO_2 morphologies, including nanorods and planar FTO electrodes.

3.2. Experimental

3.2.1. Synthesis of SnO_2 nanorods and preparation of FTO electrodes

SnO_2 nanorod films were prepared following previously reported hydrothermal synthesis procedures.[18,28] Nanorod arrays were grown on 0.5 mm thick molybdenum foil cut into 10x10 mm squares. Prior to the nanorod growth, substrates were cleaned in a detergent solution, followed by sonication in acetone for ~30 minutes. The hydrothermal reaction consisted of a growth solution containing 6.00 g NaOH, 3.51 g of $SnCl_4 \cdot 5H_2O$, and 150 mL DI H_2O. The solution was then poured into a 300 mL stainless steel autoclave followed by placement of the Mo foil substrates. The autoclave was heated to 285°C for 15 hours, during which time the pressure within the autoclave reached ~1000 psi. The nanorods on the Mo substrates were then removed and rinsed with DI H_2O

followed by isopropanol for ~30 seconds each and characterized by SEM. The SEM image shown in Figure 3.1 show the nanorods grow in a “flower-like” geometry with the nanorods having a rectangular geometry that are approximately ~1 μm in length with a diameter range ~50-200 nm. FTO samples were purchased from Hartford Glass with a sheet resistance of 15 Ω cm^{-1}, with ~400 nm thick FTO layer deposited onto the glass slide. Samples were cut and cleaned with a detergent solution followed by rinsing with DI H_2O and isopropanol for ~30 seconds each.

3.2.2. X-ray Photoelectron Spectroscopy (XPS) Measurements

XPS data were obtained using a custom-built XPS system (Physical Electronics Inc.) consisting of a model 10–610 Al Kα source (1486.6 eV photon energy) with a Model 10–420 toroidal monochromator and a model 10–360 hemispherical analyzer with a 16-channel detector array; measurements were typically performed using a electron takeoff angle of 45°. Peak areas were calculated by fitting the raw data to Voigt functions after a Shirley baseline correction. The spectra of each sample were shifted as necessary to make the primary C(1s) peak lie at a fixed energy of 284.4 eV; all other spectra for a given sample were shifted by the same amount. Coverage calculations were determined using equation derived elsewhere, which uses literature values for sensitivity factors and an electron escape depth ~2 nm for SnO_2.[29,30]

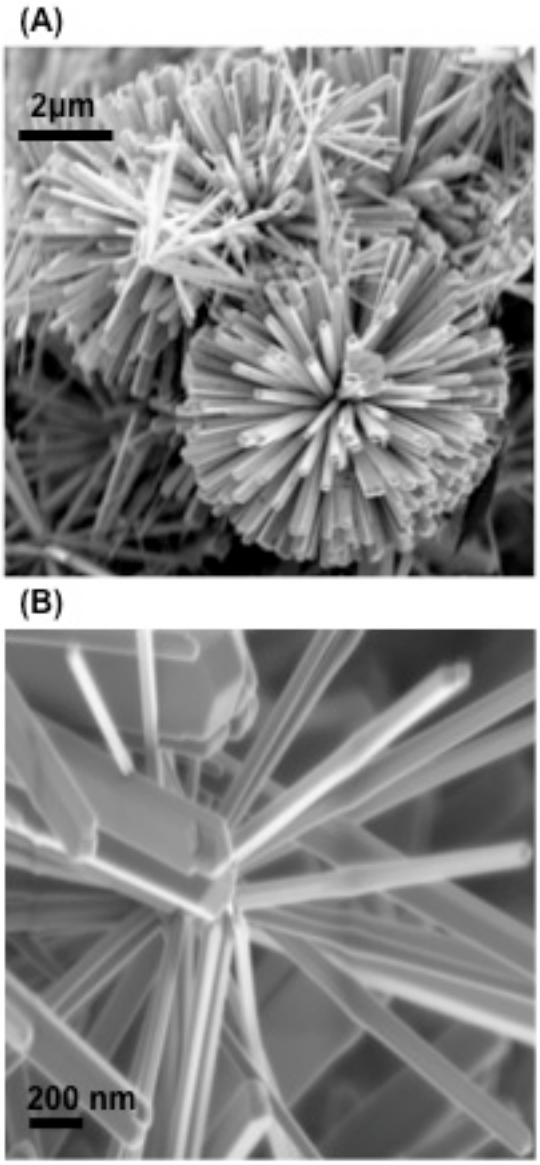

Figure 3.1: SEM images of SnO_2 nanorods (A) zoom-out image showing flower-like morphology (B) zoom-in image nanorods are ~1µm in length and 5-200 nm in diameter

3.2.3. Electrochemical Characterization

All electrochemical measurements were performed using an Autolab potentiostat (PGSTAT302N, Metrohm Autolab) using the FTO samples as the working electrode, an Ag/AgCl “no leak” reference electrode (Cypress Systems), and a platinum wire counter-electrode. The exposed area of the FTO sample was 0.785 cm^2.

3.2.4. Optical Characterization

Diffuse reflectance UV-Vis measurements were performed on a Jasco (V-570) UV/Vis/NIS spectrometer equipped with an integrating sphere accessory. Samples were mounted on a Teflon spacer to ensure equidistance between the sample surface and the sampling window. Absorption spectra of solutions were obtained on a UV–visible spectrophotometer (UV240PC, Shimadzu).

3.2.5. Time-Resolved Surface Photovoltage (TR-SPV) Measurements

Time-resolved surface photovoltage measurements[31-33] were performed using a custom-made cell holder in which an FTO sense electrode was held 25 μm away from the sample surface. The sample was illuminated with short pulses (<3 ns, 500 μJ/pulse) from a tunable laser system (NT340, Ekspla, Inc.); the resulting injection of electrons from the surface into the bulk induced transient changes in the potential, and these changes were measured at the pickup electrode. The sense electrode signal was amplified using a fast amplifier (Model TA2000B-3, FAST ComTec GmbH) with a 50-Ω

input and output impedances, 1.5 GHz bandwidth, and 40x voltage gain. The amplified output was recorded on a sampling digital oscilloscope (Model DSO5054A, Agilent, Inc.)

3.3. Results

3.3.1. Azide termination of SnO_2 Nanorods and FTO Electrodes

SnO_2 samples were terminated with an azide through a multi-step surface chemistry that was previously used on SnO_2 nanocrystalline films.[13] In summary, the samples were photochemically grafted with neat 3-buten-1-ol under 254 nm illumination for ~17 hours, to give alcohol groups slightly removed from the SnO_2 surface. The samples were then rinsed with methanol and isopropanol, ~30 seconds each. A mesylation reaction was performed to replace the alcohol group with a mesyl group in a 1:1:10 solution of methanesulfonyl chloride, triethylamine, and dichloromethane in an ice bath for ~1 hour. The samples were then rinsed with dichloromethane, methanol, and isopropanol, ~30 seconds each. The azide termination reaction was performed by submersing the samples in a supersaturated solution of NaN_3 in DMSO and heated to 80°C for ~17 hours then rinsed with DI H_2O and isopropanol, ~30 seconds each, refer to Chapter 2, Figure 2.3 for schematic representation.

3.3.2. Characterization of Photochemical Grafting on FTO

Because the photochemical grafting technique can lead to multilayer formation that could potentially perturb electron transfer processes,[16,34,35] it is important to characterize the extent of the initial photochemical grafting functionalization. FTO was used for these experiments because it is relatively smooth and variations in the calculations due to varying surface area morphology are minimized. FTO samples were exposed to 3-buten-1-ol and illuminated for varying amounts of time (~3 to 68 hours). The samples were then azide terminated to give a distinguishable feature by XPS. As seen in Figure 3.2a, the high resolution XPS scan of the N (1s) region shows a broad peak at ~400 eV that is from two overlapping. These peaks are associated with the two nitrogens that have a neutral and localized negative charge. An additional peak becomes especially distinguishable with increasing illumination times. This high binding energy peak at 405 eV is due to the nitrogen with the localized positive charge. Determining the peak area from nitrogen and comparing to the area under the Sn ($3d_{5/2}$) peak combined with the sensitivity factors of 0.477 and 4.095 for N (1s) and Sn ($3d_{5/2}$), respectively an approximate coverage of azide molecules can be determined. Figure 3.2b shows the calculated azide molecules per cm^2 on the left vertical axis while the right axis gives the C (1s) peak area to Sn ($3d_{5/2}$) peak area ratio. Illumination time for initial grafting is given on the x-axis. It is apparent that at illumination times shorter than 17.5 hours gives sub-monolayer formation and greater than 24 hours gives multilayer formation, therefore the photochemical grafting reaction illumination times were always between 17 and 24 hours.

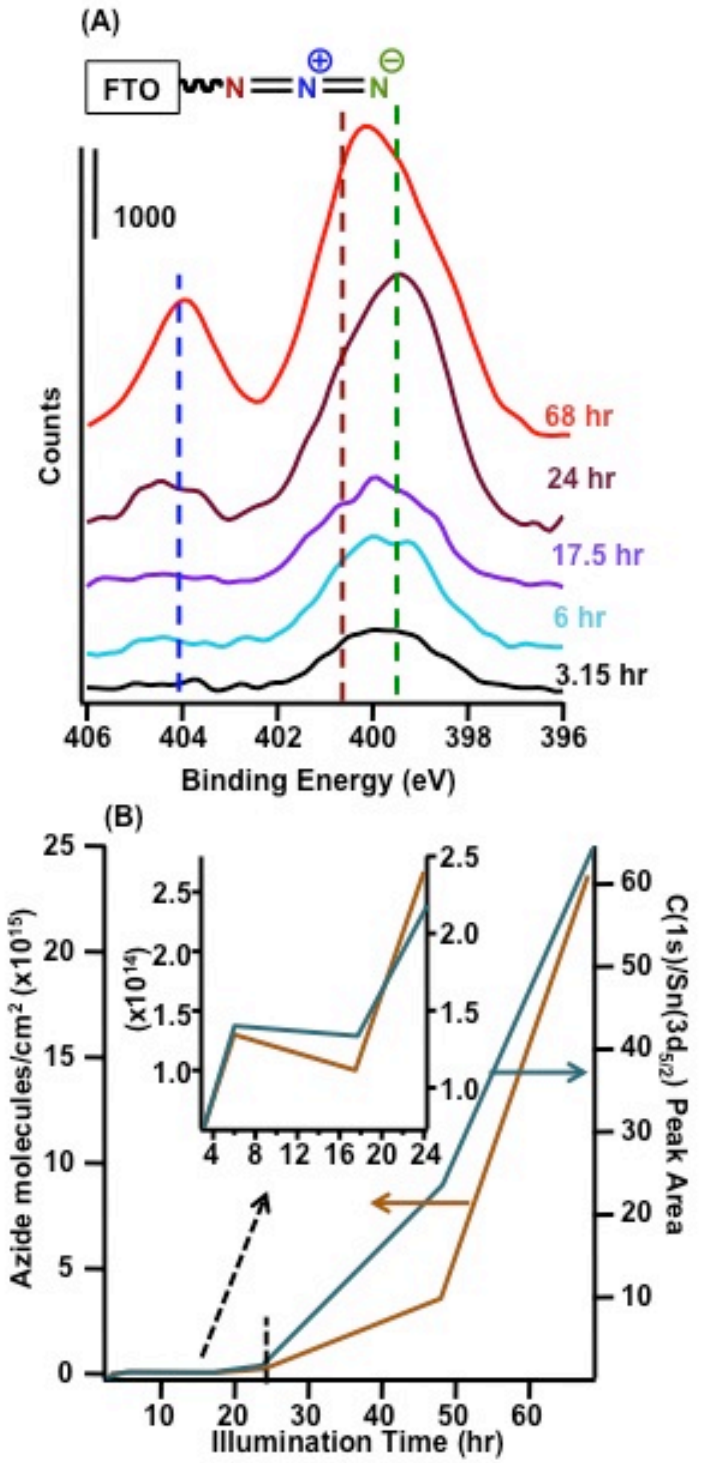

Figure 3.2: (A) XPS high resolution scan of N(1s) region with increasing illumination times for initial photochemical grafting step (B) Grafting kinetics of increasing illumination times comparing azide molecules/cm^2 on left axis and C(1s) to Sn($3d_{5/2}$) peak area ratio on right axis, inset: zoom of 3 to 24 hour illumination times

3.3.3. CuAAC Reaction of Azide-Modified Samples and [Ru(bpy)(tpy)"Cl]$^+$

Azide-modified surfaces were submersed into a solution of 1 mL of 5 mM [Ru(bpy)(tpy")Cl]$^+$ in DMSO, 1 mL of 10 mM Cu(II)(tris-(benzyltriazolyl-methyl)amine)$(BF_4)_2$ (henceforth referred to as Cu/TBTA) in DMSO, 1 mL 50 mM sodium ascorbate in H_2O diluted with an additional 2.25 mL of DMSO. The solution stirred at room temperature for ~15 hours to ensure complete reaction. The samples were rinsed sequentially with methanol and isopropanol for ~30 seconds each. The reaction scheme in Figure 3.3 summarizes the reaction with the azide modified SnO_2 surfaces and [Ru(bpy)(tpy")Cl]$^+$.

XPS analysis of the SnO_2 nanorods and FTO samples modified with [Ru(bpy)(tpy")Cl]$^+$ was used to determined the successfulness of CuAAC reaction. Figure 3.4a shows the XPS high-resolution scan on FTO of the Ru (3d) region, which overlaps with the C (1s) region. For the azide-modified FTO sample that was exposed to the full CuAAC reaction conditions, a new peak arises at 280 eV, which corresponds to the Ru ($3d_{5/2}$), the peak from Ru ($3d_{3/2}$) is not distinguishable from the C (1s) peak at 284.4 eV. A control was performed in which the azide-modified FTO sample was exposed to the CuAAC reaction except the Cu/TBTA solution was omitted. It is apparent that there is no Ru peak for the no Cu control. The azide-modified SnO_2 nanorods yielded similar results, as seen in Figure 3.4b. The azide-modified SnO_2 nanorods that were exposed to the full CuAAC reaction conditions show the same peak at 280 eV from the Ru ($3d_{5/2}$) and for the no Cu control there is no observable peak from Ru ($3d_{5/2}$). Comparison of the peak areas of the Ru ($3d_{5/2}$) and Sn ($3d_{5/2}$) and sensitivity

factor of 2.196 for the Ru ($3d_{5/2}$) which should be 3/2 the for Ru (3d) peaks,[29] an approximate coverage is determined to be 9.28 x 10^{13} Ru atoms/cm^2 for $[Ru(bpy)(tpy")Cl]^+$-modified FTO and 1.05 x 10^{14} Ru atoms/cm^2 for $[Ru(bpy)(tpy")Cl]^+$-modified SnO_2 nanorods.

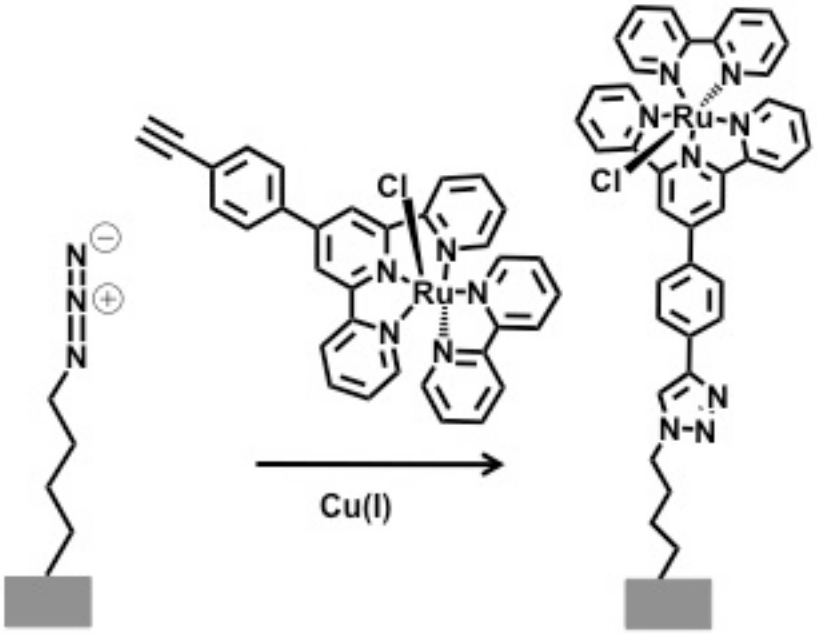

Figure 3.3: Reaction scheme of CuAAC reaction with azide-modified SnO_2 nanorods or FTO with $[Ru(bpy)(tpy'')Cl]^+$.

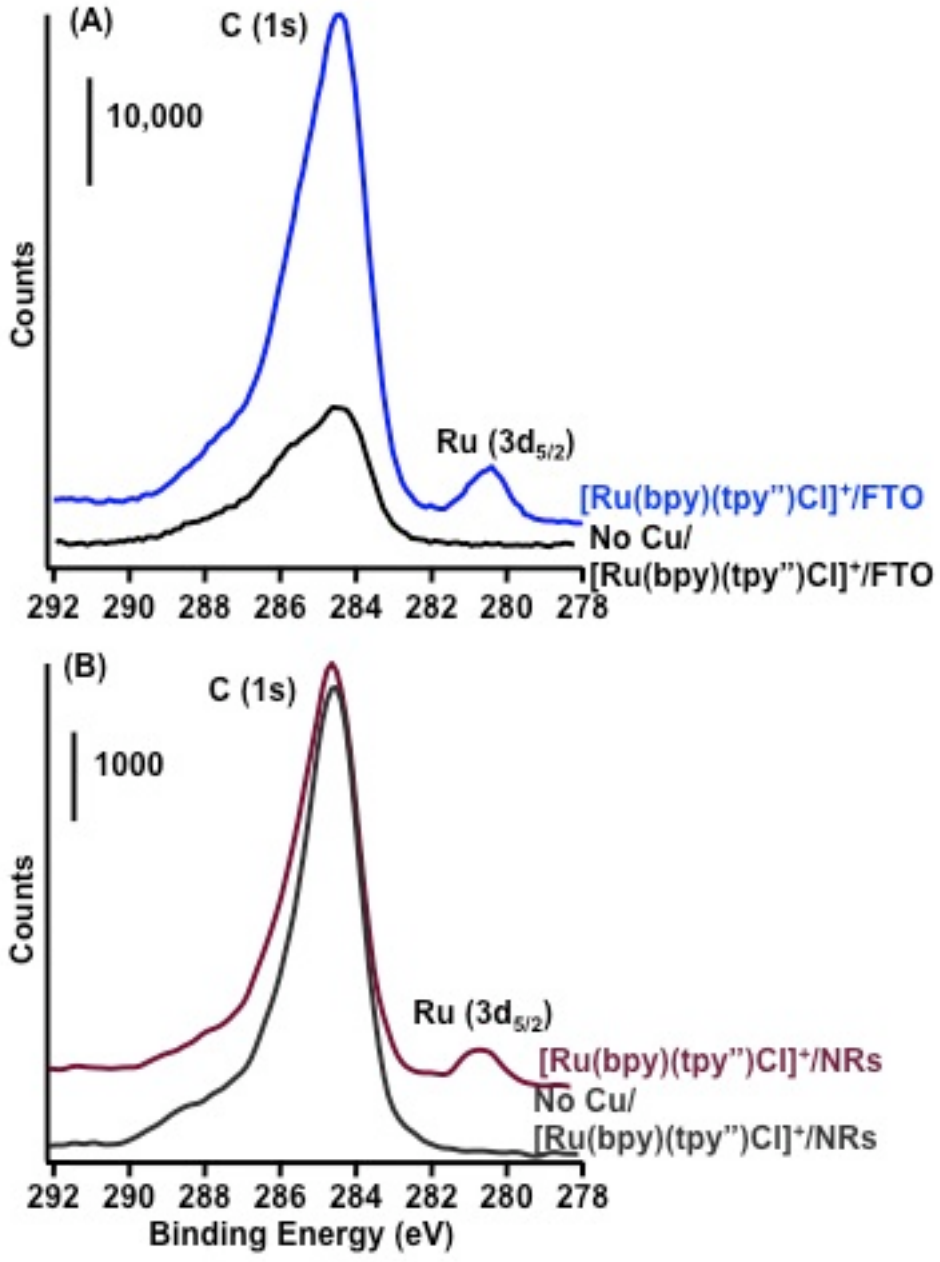

Figure 3.4: XPS high resolution scan of C (1s) and Ru (3d) region for (A) $[Ru(bpy)(tpy")Cl]^+$ /FTO and the no Cu control and (B) $[Ru(bpy)(tpy")Cl]^+$ /SnO_2 nanorods (NRs) and the no Cu control

3.3.4. Photoelectrochemical Characterization of [Ru(bpy)(tpy")Cl]+-Modified SnO_2 Nanorods

SnO_2 nanorods have many interesting properties for DSSCs, which depend on the ability to effectively separate charge.[2] Time-resolved surface photovoltage (TR-SPV) was performed on the $[Ru(bpy)(tpy")Cl]^+$-modified SnO_2 nanorods to characterize the electron injection. Figure 3.5a gives a representative transient signal at 500nm excitation. The initial negative signal results from the sample having a positive charge at the surface following electron injection into SnO_2 nanorods, which causes the sense electrode to polarize to a transient negative charge. The transient signal also has a positive sign followed by an exponential decay, corresponding to the recombination of charges. Integration of the total transient signal, normalization by incident photons, and plotting versus excitation wavelength, as shown in Figure 3.5b, elucidates the wavelength dependence of the $[Ru(bpy)(tpy")Cl]^+$ modified SnO_2 nanorods. Comparing to the UV-Vis, as seen in Figure 3.5c of the $[Ru(bpy)(tpy")Cl]^+$ modified SnO_2 nanorods and $[Ru(bpy)(tpy")Cl]^+$ in DMSO to the $[Ru(bpy)(tpy")Cl]^+$ is capable of injecting electrons at all absorbing wavelengths.

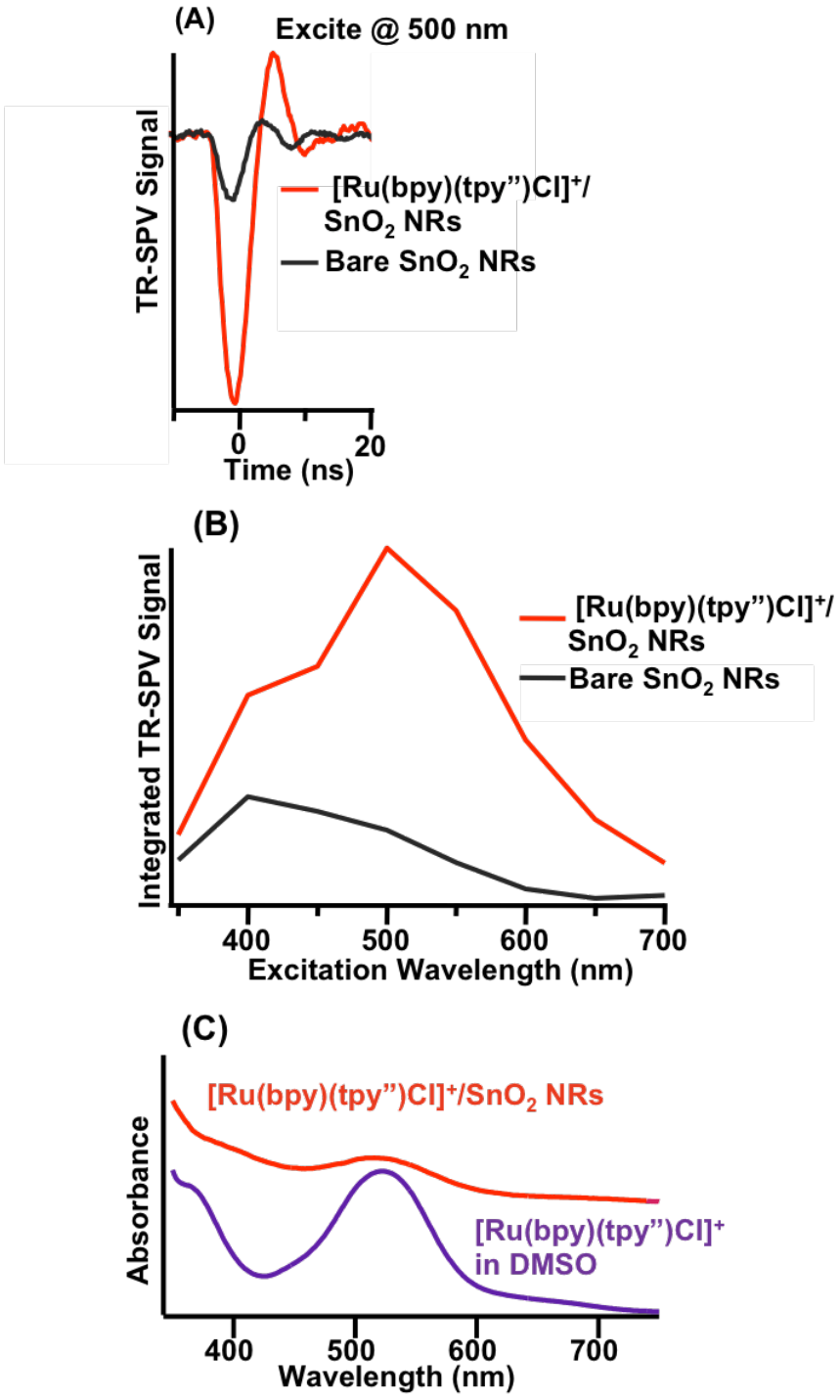

Figure 3.5: (A) Representative TR-SPV signal of $[Ru(bpy)(tpy")Cl]^+$-SnO_2 nanorods (NRs) and bare NRs, (B) the integrated total SPV signal versus excitation wavelength for $[Ru(bpy)(tpy")Cl]^+$-SnO_2 NRs and bare NRs, and (C) Diffuse reflectance UV-Vis of $[Ru(bpy)(tpy")Cl]^+$-SnO_2 and $[Ru(bpy)(tpy")Cl]^+$ in DMSO

3.3.5. Electrocatalytic Characterization of [Ru(bpy)(tpy")Cl]+ Modified FTO

The chloro ligand in ruthenium coordination complexes, like the $[Ru(bpy)(tpy")Cl]^+$ is theorized to increase the electrophilicity of the metal, allowing for the likely attachment of a water molecule to the metal center following loss of two electrons during electrocatalytic water oxidation, as depicted in Figure 3.6.[26] The Ru^{IV}-OH_2 complex is further oxidized to form the intermediate Ru^{VI}=O. An additional water molecule is likely involved at the electrophilic Ru^{VI}=O center to create a $Ru^{VI}OOH$ species. A loss of an additional proton then produces O_2 and the starting catalyst.[26]

To test the ability for $[Ru(bpy)(tpy")Cl]^+$ covalently tethered to the FTO surface to oxidize water, an electrochemical cell was assembled using 0.1 M n-$Bu_4N(PF_6)$ in acetonitrile (n-Bu_4N^+= tetrabutylammonium cation) was used. Water was added to the cell so that a ratio of 3:1 CH_3CN:H_2O by volume was achieved. The potential was scanned from 0 to 1.8 V vs. Ag/AgCl at a scan rate of 1.0 V/sec. As seen in Figure 3.7a, the cyclic voltammogram (CV) without H_2O (black curve) the oxidation and reduction peaks are clearly visible at 1.00 V and 0.900 V from the Ru (III/II) couple.[4] After the addition of 1 mL H_2O (blue curve), the peaks become larger and shift to lower potentials of ~0.95 V and 0.87 V.

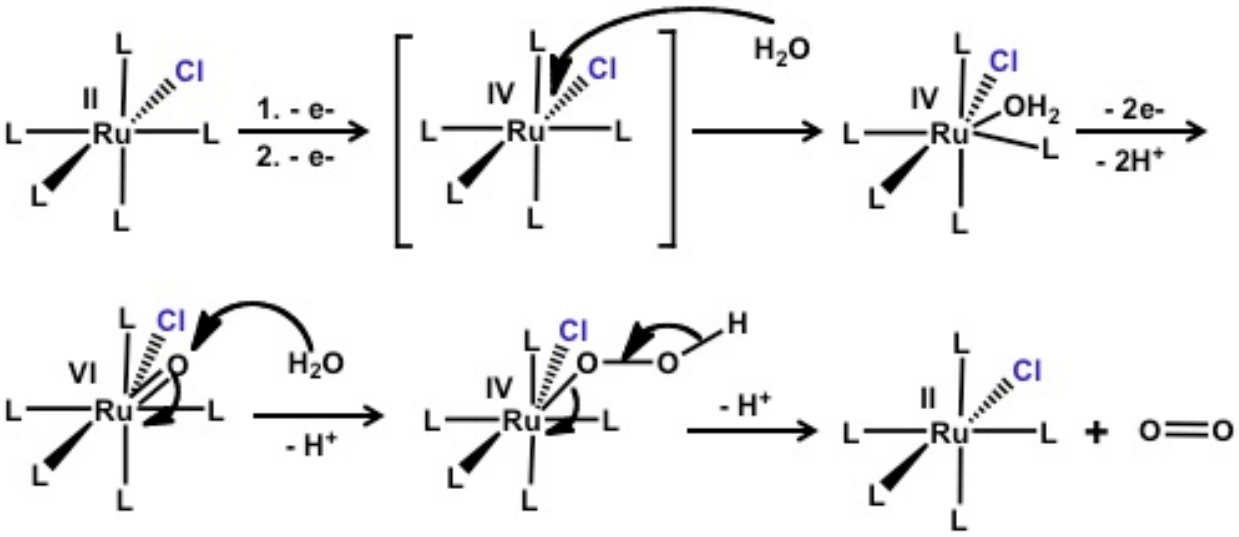

Figure 3.6: Proposed mechanism of water oxidation by ruthenium mononuclear catalyst highlighting the importance of the chloro ligand. Adapted from ref 26

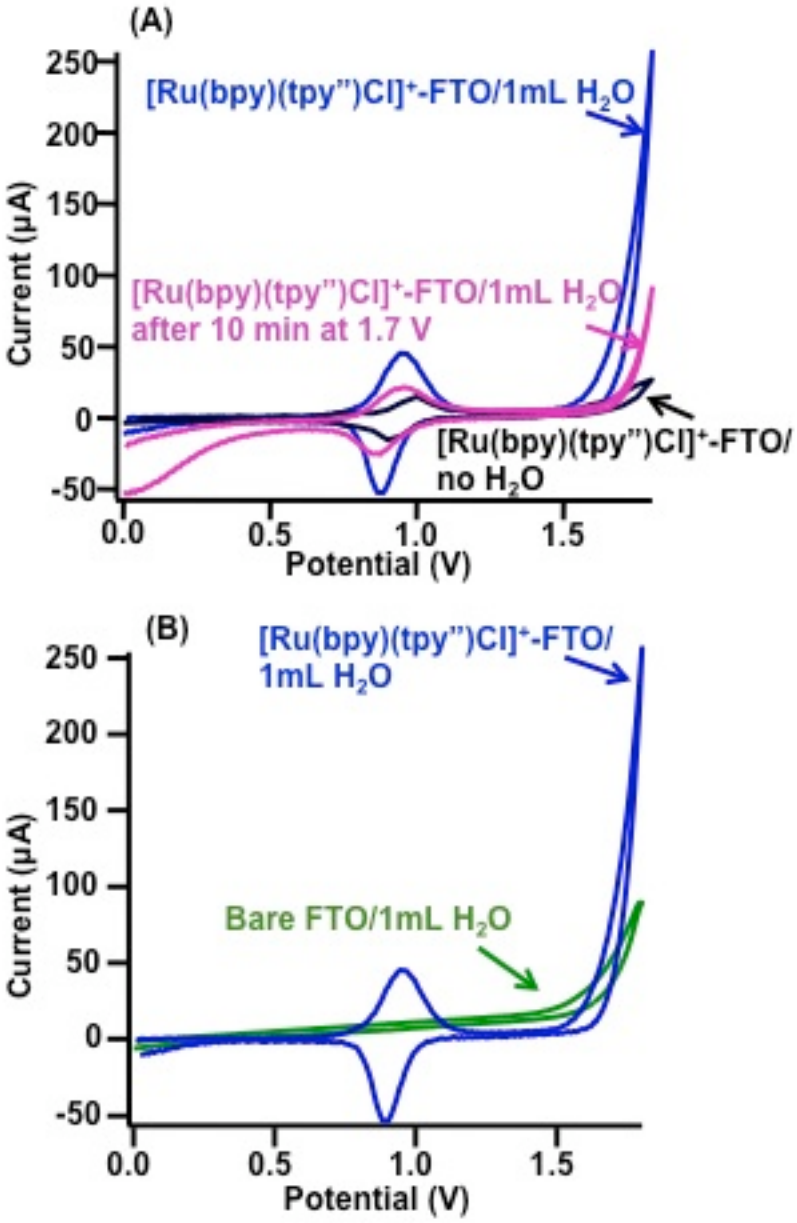

Figure 3.7: (A) CV of $[Ru(bpy)(tpy")Cl]^+$ modified FTO without H_2O (black), with 1mL H_2O (blue), and after being held at 1.7 V for 10 min (pink) and (B) comparison of $[Ru(bpy)(tpy")Cl]^+$ modified FTO with 1mL H_2O and bare FTO with 1mL H_2O

The change is attributed to the outer-sphere solvation effect.[24,36] Another feature that arises with the addition of H_2O is the onset of a catalytic wave at ~1.6 V from the oxidation to achieve the Ru^{VI}=O complex, [4,37] and reaches a maximum at 1.8 V where the electrocatalytic water oxidation is sustained. This over-potential is similar to what has been reported previously on FTO surfaces with water oxidation catalysts anchored through a phosphine group.[24] Integration under the anodic peak of the no H_2O CV and using the working electrode area of 0.785 cm^2 gives approximately 4.78 x 10^{13} $[Ru(bpy)(tpy")Cl]^+$ redox active molecules/cm^2, which closely correlates with XPS calculations. Comparison to an unmodified FTO electrode is shown in Figure 3.7b. The unmodified FTO shows small catalytic activity towards water oxidation, however there is a large enhancement for the FTO electrode with surface bound $[Ru(bpy)(tpy")Cl]^+$. The molecular tether was studied by stressing the system by holding the FTO working electrode at a constant potential of 1.7 V. After 10 minutes at 1.7 V, the CV (shown in pink) shows a reduction in the peaks associated with Ru(III/II) couple and a shift in the onset of the catalytic wave as well as an overall reduction in the electrocatalytic oxidation of H_2O. The decrease and change in catalytic activity could be caused from degradation of the molecular tether and/or degradation of the catalyst, however based on these electrochemical experiments it is difficult to elucidate the possible degradation routes.

3.4. Discussion

Because photochemical grafting on SnO_2 surfaces has only recently been investigated,[13,28] we used FTO as a model for determining the extent of photochemical grafting of 3-buten-1-ol because the planar morphology reduced any variations between sample surfaces. It was determined that at illumination times >24 hours multilayer formation occurred while at illumination hours <17 hours sub-monolayers were formed, therefore all photochemical grafting reactions occurred at illumination times of ~17 hours and never exceeded 24 hours. The SnO_2 nanorod morphology investigated the reactivity of well-defined crystal faces of (100) and (001). From our experimental results on the SnO_2 nanorods and previous results on SnO_2 nanocrystalline thin films,[13] the modular attachment of a photochemically active species is robust on all SnO_2 crystal faces. The TR-SPV results show the electron injection of $[Ru(bpy)(tpy")Cl]^+$ into the nanorods occurs at all absorbing wavelengths of the $[Ru(bpy)(tpy")Cl]^+$ complex.

We explored the electrocatalytic activity of the surface bound $[Ru(bpy)(tpy")Cl]^+$ FTO due to its excellent conductivity for electrochemical analysis. $[Ru(bpy)(tpy")Cl]^+$ was successfully tethered to the surface of FTO through CuAAC reaction. The electrochemical analysis compared the $[Ru(bpy)(tpy")Cl]^+$ modified FTO electrode and an unmodified FTO electrode. The unmodified FTO electrode yielded a small catalytic wave, but the presence of $[Ru(bpy)(tpy")Cl]^+$ greatly enhanced the electrocatalytic oxidation of water. The stability of the system was investigated by holding the $[Ru(bpy)(tpy")Cl]^+$ modified FTO electrode at 1.7 V for 10 minutes, followed by a CV scan. The CV showed a reduced amount of the $[Ru(bpy)(tpy")Cl]^+$ complex as

evidenced by the reduction in the peaks for the Ru(III/II) couple. A reduction in the electrocatalytic wave associated with water oxidation was also observed. The loss in electrocatalytic activity could be the result of catalyst degradation or from detachment of the catalyst from the FTO surface or a combination of both. Detailed mechanistic studies of mononuclear ruthenium water oxidation catalysts and their degradation pathways are still being investigated, however the ability to tether to an electrode surface can allow for improved mechanistic studies because the use of a sacrificial agent is no longer needed.[26,36]

3.5. Conclusions

SnO_2 possesses many properties, like high electron mobility and aqueous stability, which make it a leading candidate for renewable energy technologies.[3,37,38] The ability to modify the surfaces of many SnO_2 morphologies, like nanorods and planar FTO, through the use of a modular attachment chemistry employing the use of the CuAAC reaction broadens the use of SnO_2 in many applications such as photovoltaics and heterocatalysis.[3,38] In the work presented here, we show that the CuAAC reaction is a versatile method for tethering molecular species to SnO_2 surfaces. There is no noticeable variation in the reactivity of well-defined crystal faces or the conductivity of the substrate for the initial photochemical grafting of 3-buten-1-ol, mesylation, and azide termination of the SnO_2 surfaces. The CuAAC reaction with $[Ru(bpy)(tpy")Cl]^+$ and the azide-modified SnO_2 surfaces proceed under mild conditions and only in the presence of Cu. The resulting $[Ru(bpy)(tpy")Cl]^+$ modified SnO_2 nanorods are

photoelectrochemically active with electron injection at all absorbing wavelengths of the $[Ru(bpy)(tpy")Cl]^+$ complex. The $[Ru(bpy)(tpy")Cl]^+$ modified FTO surface was capable of electrocatalytically oxidizing water at over-potentials similar to what has been reported previously for FTO. [24] The work presented here further validates the versatility of the CuAAC reaction between various azide-modified SnO_2 surfaces and a ruthenium complex to yield surfaces that are photoelectrochemically and electrocatalytically active.

3.6. References

(1) Fortunato, E.; Ginley, D.; Hosono, H.; Paine, D. C. *Mrs Bulletin* **2007**, *32*, 242.

(2) Gratzel, M. *Nature* **2001**, *414*, 338.

(3) Jose, R.; Thavasi, V.; Ramakrishna, S. *Journal of the American Ceramic Society* **2009**, *92*, 289.

(4) Chen, Z. F.; Concepcion, J. J.; Hull, J. F.; Hoertz, P. G.; Meyer, T. J. *Dalton Transactions* **2010**, *39*, 6950.

(5) Hanson, K.; Brennaman, M. K.; Luo, H. L.; Glasson, C. R. K.; Concepcion, J. J.; Song, W. J.; Meyer, T. J. *Acs Applied Materials & Interfaces* **2012**, *4*, 1462.

(6) Mola, J.; Mas-Marza, E.; Sala, X.; Romero, I.; Rodriguez, M.; Vinas, C.; Parella, T.; Llobet, A. *Angewandte Chemie-International Edition* **2008**, *47*, 5830.

(7) Surendranath, Y.; Dinca, M.; Nocera, D. G. *J. Am. Chem. Soc.* **2009**, *131*, 2615.

(8) Asghar, M. I.; Miettunen, K.; Halme, J.; Vahermaa, P.; Toivola, M.; Aitola, K.; Lund, P. *Energy Environ. Sci.* **2010**, *3*, 418.

(9) Hinsch, A.; Kroon, J. M.; Kern, R.; Uhlendorf, I.; Holzbock, J.; Meyer, A.; Ferber, J. *Progress in Photovoltaics* **2001**, *9*, 425.

(10) Lunt, R. R.; Osedach, T. P.; Brown, P. R.; Rowehl, J. A.; Bulovic, V. *Adv. Mater.* **2011**, *23*, 5712.

(11) Brimblecombe, R.; Dismukes, G. C.; Swiegers, G. F.; Spiccia, L. *Dalton Transactions* **2009**, 9374.

(12) Sala, X.; Romero, I.; Rodriguez, M.; Escriche, L.; Llobet, A. *Angewandte Chemie-International Edition* **2009**, *48*, 2842.

(13) Benson, M. C.; Ruther, R. E.; Gerken, J. B.; Rigsby, M. L.; Bishop, L. M.; Tan, Y. Z.; Stahl, S. S.; Hamers, R. J. *Acs Applied Materials & Interfaces* **2011**, *3*, 3110.

(14) Devaraj, N. K.; Collman, J. P. *Qsar & Combinatorial Science* **2007**, *26*, 1253.

(15) Finn, M. G.; Kolb, H. C.; Fokin, V. V.; Sharpless, K. B. *Progress in Chemistry* **2008**, *20*, 1.

(16) Franking, R. A.; Landis, E. C.; Hamers, R. J. *Langmuir* **2009**, *25*, 10676.

(17) Comini, E.; Guidi, V.; Malagu, C.; Martinelli, G.; Pan, Z.; Sberveglieri, G.; Wang, Z. L. *Journal of Physical Chemistry B* **2004**, *108*, 1882.

(18) Wang, Y. L.; Guo, M.; Zhang, M.; Wang, X. D. *Crystengcomm* **2010**, *12*, 4024.

(19) Kislyuk, V. V.; Dimitriev, O. P. *Journal of Nanoscience and Nanotechnology* **2008**, *8*, 131.

(20) Gubbala, S.; Chakrapani, V.; Kumar, V.; Sunkara, M. K. *Advanced Functional Materials* **2008**, *18*, 2411.

(21) Andersson, A.; Johansson, N.; Broms, P.; Yu, N.; Lupo, D.; Salaneck, W. R. *Advanced Materials* **1998**, *10*, 859.

(22) Murakami, T. N.; Gratzel, M. *Inorganica Chimica Acta* **2008**, *361*, 572.

(23) Rakhshani, A. E.; Makdisi, Y.; Ramazaniyan, H. A. *Journal of Applied Physics* **1998**, *83*, 1049.

(24) Chen, Z. F.; Concepcion, J. J.; Luo, H. L.; Hull, J. F.; Paul, A.; Meyer, T. J. *J. Am. Chem. Soc.* **2010**, *132*, 17670.

(25) Duan, L. L.; Tong, L. P.; Xu, Y. H.; Sun, L. C. *Energy & Environmental Science* **2011**, *4*, 3296.

(26) Tseng, H.-W.; Zong, R.; Muckerman, J. T.; Thummel, R. *Inorganic Chemistry* **2008**, *47*, 11763.

(27) Lu, G.-Q.; Wieckowski, A. *Current Opinion in Colloid & Interface Science* **2000**, *5*, 95.

(28) Shah, S.; Benson, M. C.; Bishop, L. M.; Huhn, A. M.; Ruther, R. E.; Yeager, J. C.; Tan, Y. Z.; Louis, K. M.; Hamers, R. J. *Journal of Materials Chemistry* **2012**, *22*, 11561.

(29) Moulder, J. F.; Stickle, W. F.; Sobol, P. E.; Bomben, K. D. *Handbook of X-ray Photoelectron Spectroscopy*; Perkin-Elmer Corporation: Eden Prarie, MN, 1992.

(30) Wagner, C. D.; Naumkin, A. V.; Kraut-Vass, A.; Allison, J. W.; Powell, C. J.; Rumble, J. R., Jr *NIST X-ray Photoelectron Spectroscopy Database*; National Institue of Standards and Technology: Gaithersburg, MD, 2003; Vol. Version 3.5.

(31) Anta, J. A.; Mora-Seró, I.; Dittrich, T.; Bisquert, J. *Journal of Physical Chemistry C* **2007**, *111*, 13997.

(32) Kronik, L.; Leibovitch, M.; Fefer, E.; Burstein, L.; Shapira, Y. *Journal of Electronic Materials* **1995**, *24*, 379.

(33) Mora-Séro, I.; Dittrich, T.; Garcia-Belmonte, G.; Bisquert, J. *Journal of Applied Physics* **2006**, *100*.

(34) Strother, T.; Knickerbocker, T.; Russell, J. N.; Butler, J. E.; Smith, L. M.; Hamers, R. J. *Langmuir* **2002**, *18*, 968.

(35) Colavita, P. E.; Sun, B.; Tse, K.-Y.; Hamers, R. J. *J. Am. Chem. Soc.* **2007**, *129*, 13554.

(36) Roy, S.; Bagchi, B. *The Journal of Physical Chemistry* **1994**, *98*, 9207.

(37) Chen, Z. F.; Concepcion, J. J.; Jurss, J. W.; Meyer, T. J. *J. Am. Chem. Soc.* **2009**, *131*, 15580.

Chapter 4

A Stable Functionalization Method for the Introduction of a Short-chain Alkyne to a SnO_2 Nanocrystalline Thin Film to Enable Further CuAAC Mediated Surface Derivatization

4.1. Introduction

The ability to introduce a variety of functional groups onto the surface of SnO_2 would increase its use in applications such as solar harvesting devices and supports for heterocatalysis.[1-3] Recently, it has been demonstrated an organic azide introduced onto the surface of metal oxides, noble metals, and carbon materials is capable of undergoing the Cu(I) catalyzed azide-alkyne cycloaddition (CuAAC).[4-7] However organic azide installation often involves the use of long alkyl chains, which can inhibit electron transfer from a tethered electro- or photoactive species.[8,9] Another disadvantage of being limited to only an azide-modified surface is that only alkyne-containing molecules or nanoparticles can be attached to the surface via CuAAC. A step-wise method, similar to previous azide termination technique,[10] to introduce a terminal alkyne would require much more harsh and highly basic conditions that can lead to dissolution of the SnO_2 surface.[11-15] One solution is the direct attachment of the terminal alkynes to metal oxides. This has been only sparsely investigated but often relies on the adsorption of anchoring groups that lack stability under a wide variety of conditions.[16-18] The silicon literature offers some insight into methods of producing alkyne terminated surface through the thermal grafting of a long chain diyne as shown in Figure 4.1a, however, it

has been acknowledged the long alkyl chains are capable of hindering electron transfer.[19,20] Another method of attaching an alkyne group has been through silane grafting, shown in Figure 4.1b.[21] However, the M-O-M bond (where M = any metal of metalloid) is easily hydrolyzed and can cause the alkyne to become detached form the surface.[16] The limitations of current methods for introducing an alkyne group to the surface of a metal oxide highlight the need for alternate techniques.

Thermal grafting under mild heating conditions have shown to give alkyl, benzyl, or aryl functionality covalently bound to TiO_2 such that it is stable under a variety of conditions.[22,23] Thermal grafting requires gentle heating to remove the adsorbed water from the surface of the metal oxide, followed by formation of an ether-like linkage similar to the well-known Williamson Ether Synthesis. Metal oxide surfaces are comprised of hydroxyl groups and exposed Lewis acidic metal cations, which have unique reactivity where interesting surface functionalizations can occur. [23] The pKa of SnO_2 hydroxyl groups are <1, while that of secondary alcohols are ~16.[24,25] The work presented here shows the ability to thermally graft a short-chain terminal alkyne to SnO_2 surfaces. The resulting ether linkage to the surface of SnO_2 possesses enhanced stability as compared to thermally grafted molecules to TiO_2 surfaces.[23] The resulting terminal alkyne is confirmed to be orthogonal to the surface of SnO_2 due to its availability to undergo CuAAC reaction.

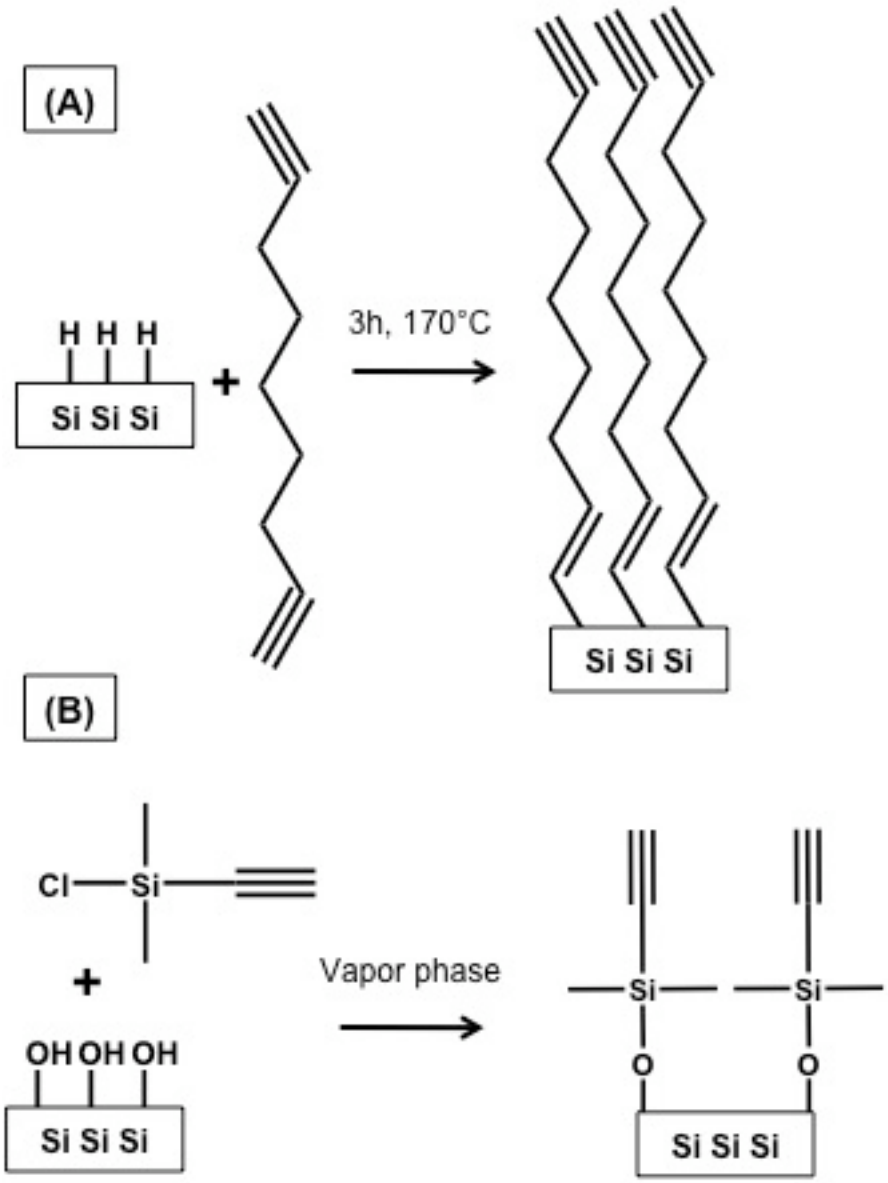

Figure 4.1: Schematic representation of two methods for introducing an alkyne modified Si surface through (A) alkyne (ref 19) or (B) silane grafting (ref 21).

4.2. Experimental

4.2.1. SnO_2 Nanocrystalline Thin Film Preparation

SnO_2 nanoparticles (20-70nm) were purchased from Nanostructured and Amorphous Materials. The nanoparticles were made into a paste using previously developed procedures.[10] SnO_2 nanocrystalline thin-films were created by screen-printing the SnO_2 paste onto fluorine-doped tin oxide (FTO) deposited onto a glass slide (sheet resistance 15 Ω/sq). The films were then sintered at 500°C for ~2 hours to yield a nanocrystalline film with good electrical contact to the substrate. Scanning electron microscopy was performed to characterize the film thickness to be ~700nm to 1μm, see Chapter 5, section 5.3.1 for SEM image.

4.2.2. Fourier-Transform Infrared (FTIR) Measurements

Infrared spectra were collected using an FTIR spectrometer (Vertex 70, Bruker Optics) at a resolution of 4 cm^{-1}. FTIR spectra were collected in single-bounce external reflection mode using a variable angle specular reflectance accessory with a wire grid polarizer (VeeMAX II). All reflection spectra were collected with p-polarized light at an incident angle of 50° from the surface normal. FTIR spectra of functionalized surfaces were measured using an unfunctionalized sample as the background. In some specified cases an attenuated total reflectance (ATR) accessory (Pike Gladiator Technologies) was used with a diamond crystal. Other cases FTIR analysis required the use of transmission with the material of interest evaporated onto CaF_2 salt plates. Residual

baselines were removed to improve the clarity of the spectra. Baseline correction was achieved using a polynomial fit to remove sloping and/or curved background. In each case, the experimental spectrum was fit to a polynomial using all points in the selected regions and avoid regions where containing peaks from surface species, and the resulting polynomial was then subtracted from the data. In general, fits were performed using several different polynomial orders in order to ensure that the spectral features observed were not sensitive to the precise details of the fitting procedure.

4.2.3. X-ray Photoelectron Spectroscopy (XPS) Measurements

XPS data were obtained using a custom-built XPS system (Physical Electronics Inc.) consisting of a model 10–610 Al Kα source (1486.6 eV photon energy) with a Model 10–420 toroidal monochromator and a model 10–360 hemispherical analyzer with a 16-channel detector array; measurements were typically performed using a electron takeoff angle of 45°. Peak areas were calculated by fitting the raw data to Voigt functions after a Shirley baseline correction. The spectra of each sample were shifted as necessary to make the primary C (1s) peak at a fixed energy of 284.4 eV; all other spectra for a given sample were shifted by the same amount. Approximate coverage of ATMB molecules/cm^2 was determined using the equation below:[26]

$$\frac{ATMB}{area} = \frac{A_F}{A_{Sn}} \frac{SF_{Sn}}{SF_F} \times \rho_{Sn:SnO_2} \times \lambda_{Sn:SnO_2} \times \cos\theta \times \left(\frac{1}{3}\right)$$

Where A is the peak area, SF is the sensitivity factor reported in literature, density of Sn atoms in SnO_2, λ is the inelastic mean free path of Sn 3d electrons through SnO_2, and θ is the electron collection angle of 45°. The factor of 1/3 accounts for there being 3 F atoms/1 ATMB molecule.

4.3. Results

4.3.1. Alkyne Functionalization of SnO_2 Nanocrystalline Thin Films and CuAAC Reaction with ATMB

SnO_2 thin films were submerged into a neat solution of propargyl alcohol and placed in a sealed vial at 80°C for ~15 hours. The samples were then removed and rinsed sequentially with methanol and isopropanol for ~30 seconds with each solvent. The alkyne-terminated surface, as shown in Figure 4.2, was submerged into a solution of 2 mL DMSO, 1 mL 50mM sodium ascorbate in H_2O, 1 mL 2 mM p-azido-trifluoromethoxy benzene (ATMB) in DMSO, and 2 mL 1 mM Cu(II)(tris-(benzyltriazolyl-methyl)amine)$(BF_4)_2$ (Cu/TBTA) in DMSO, and allowed to stir at room temperature for ~15 hours to ensure complete reaction with the porous thin-film. Synthesis of ATMB is described elsewhere.[17] Control experiments were performed in the absence of Cu/TBTA solution but still in the presence of ATMB.

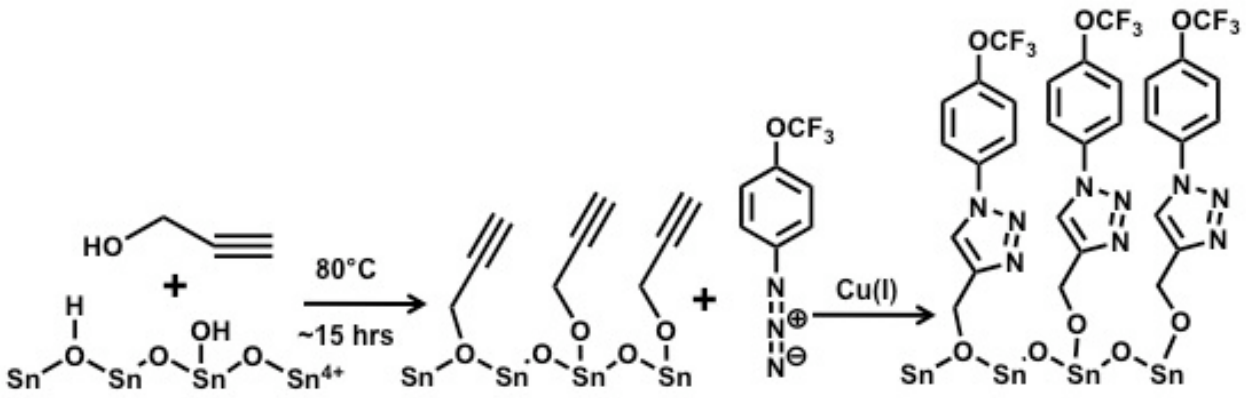

Figure 4.2: Reaction scheme of propargyl alcohol grafting to yield alkyne-modified SnO_2 nanocrystalline thin film followed by CuAAC reaction with ATMB.

4.3.2. Characterization of Thermal Grafting and CuAAC Reaction of Alkyne-Modified SnO_2 Surfaces

FTIR analysis of the alkyne-modified SnO_2 nanocrystalline thin-film, shown in Figure 4.3 reveals the characteristic peaks of the alkyne C-C stretch at 2111 cm^{-1}. Additionally there is a small feature on the broadened –OH region for the alkyne C-H stretch at 3318 cm^{-1}. For comparison, the FTIR of neat propargyl alcohol, which was taken using ATR accessory, is also shown. The large negative peak at 3479 cm^{-1} indicates loss of Sn-OH as compared to the bare SnO_2 nanocrystalline thin film background, indicating that grafting of propargyl alcohol proceeds through the surface hydroxyls. Smaller negative peaks in the CH_2 region 2925-2964 cm^{-1} are observed from the relative lack of $–CH_2$ functionality present in propargyl alcohol-grafted SnO_2 surface as compared to the "bare" SnO_2 background. It is difficult to remove all traces of adventitious carbon on the "bare" background when working in ambient atmosphere. Therefore the "bare" SnO_2 background has more $–CH_2$ groups than the alkyne-modified SnO_2, this observation confirms that propargyl alcohol grafts onto the surface of SnO_2 uniformly and is not displaced by CH_2 containing molecules in the atmosphere.

The FTIR Spectrum of the alkyne-modified surface after it was subjected to the CuAAC reaction with ATMB, the FTIR is shown in Figure 4.4. New peaks at 1186, 1224, and 1227 cm^{-1} are present, which correspond to the CF_3 stretches from ATMB. Additional we attribute a peak at 1517 cm^{-1} to the C-O bond stretch of ATMB. The sharp peaks at 1689 and 1716 cm^{-1} are attributed to adsorbed CO_2.[27]

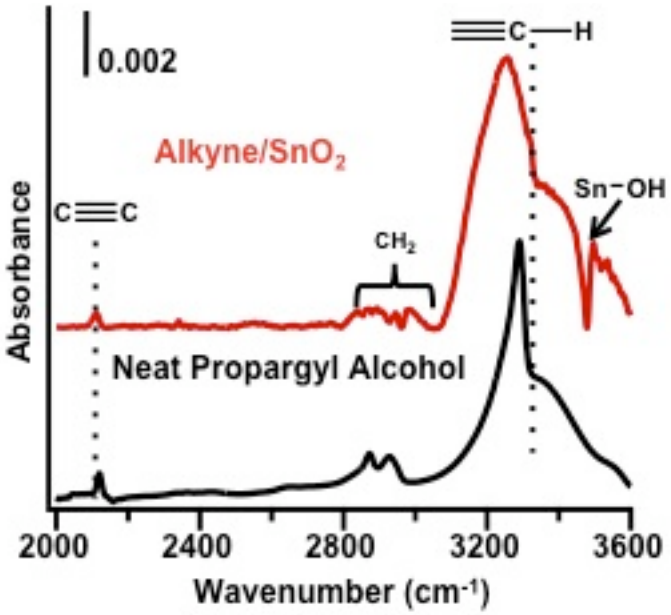

Figure 4.3: FTIR spectrum of Alkyne-modified SnO_2 (red) and neat propargyl alcohol (black). Appearance of peaks at 2111 cm^{-1} and 3318 cm^{-1} indicate presence of alkyne

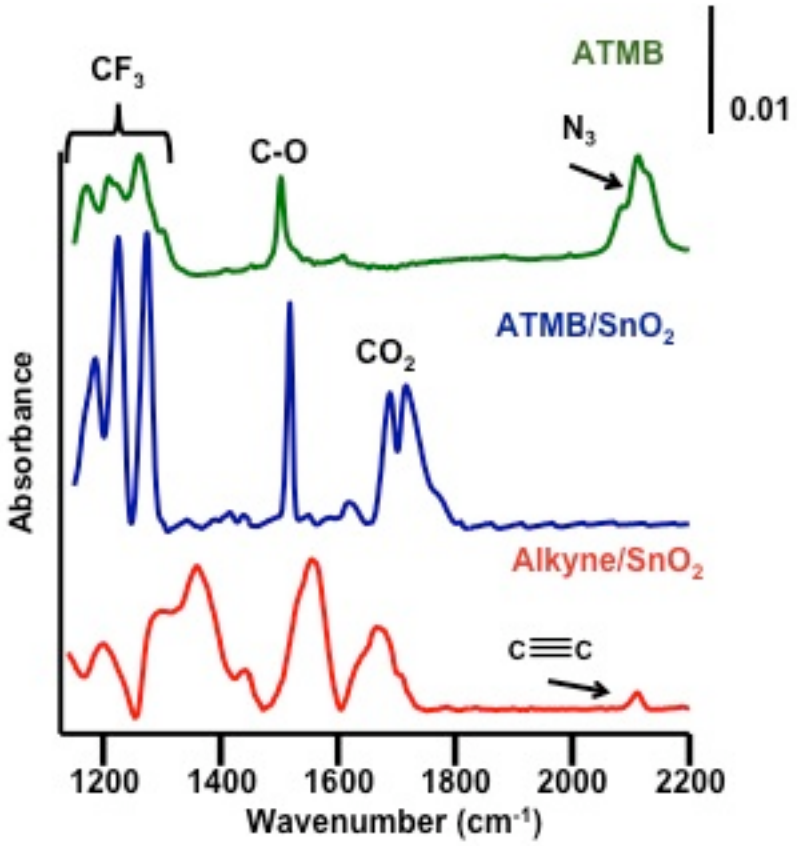

Figure 4.4: FTIR spectra of alkyne-modified SnO_2 (red), ATMB-modified SnO_2 (blue) and ATMB (green), ATMB spectrum scaled arbitrarily for clarity.

The peak at 2111 cm^{-1} from the alkyne C-C stretch is no longer present, indicating all of the alkyne groups were consumed during reaction with the azide and formation of the triazole ring. A spectrum of ATMB in chloroform taken in transmission mode using a CaF_2 salt plate is shown for comparison. The sharp peak sharp at 2113 cm^{-1} for ATMB is from the N_3 group, which is also not seen on the surface of SnO_2, strongly suggesting the CF_3 and C-O peaks observed are due to ATMB that has undergone covalent bond formation to the alkyne-modified surface via the CuAAC reaction. If these peaks were caused by non-specific binding of ATMB, the N_3 stretch at 2113 cm^{-1} should still be present.

4.3.3. XPS Characterization of ATMB-Modified SnO_2

XPS of the nanocrystalline thin films after CuAAC with ATMB show the appearance of F (1s) and N (1s) peaks, as seen in Figure 4.5. High resolution scans of the C (1s) region in Figure 4.5a for the ATMB-modified SnO_2 shows a high binding energy peak at 293.5 eV, from the C atoms in the CF_3 group. Conversely, this peak is not observed in the no-Cu control sample. We attribute the broad shoulder at the high binding energy side of the main peak at 284.4 eV to the presence of carbon bonding to oxygen and nitrogen atoms. The N (1s) high-resolution scan in Figure 4.5b gives a broad peak that is composed of two overlapping peaks at 401 eV and 400 eV. This peak shape is indicative of the formation of a triazole ring.[6,7,10] There is no N (1s) or F

(1s) signals for the no-Cu control, confirming no non-specific binding of ATMB occurs in the absence of Cu.

Comparison of the peak areas for F (1s), shown in Figure 4.5c and that of Sn ($3d_{5/2}$) taking sensitivity factors and using an inelastic mean free path of ~2nm for SnO_2,[28,29] an approximate coverage calculation of ATMB molecules was determined to be a monolayer with 5.89 $x10^{14}$ ATMB molecules/cm^2. This value is consistent with the formation of a monolayer as seen previously with other nanocrystalline thin-films.[30,31] From the control experiment it can be concluded that the CuAAC requires a source of Cu(I) for the cycloaddition to take place and there is no non-specific binding of ATMB to the surface of SnO_2 nanocrystalline surface in the presence of Cu.

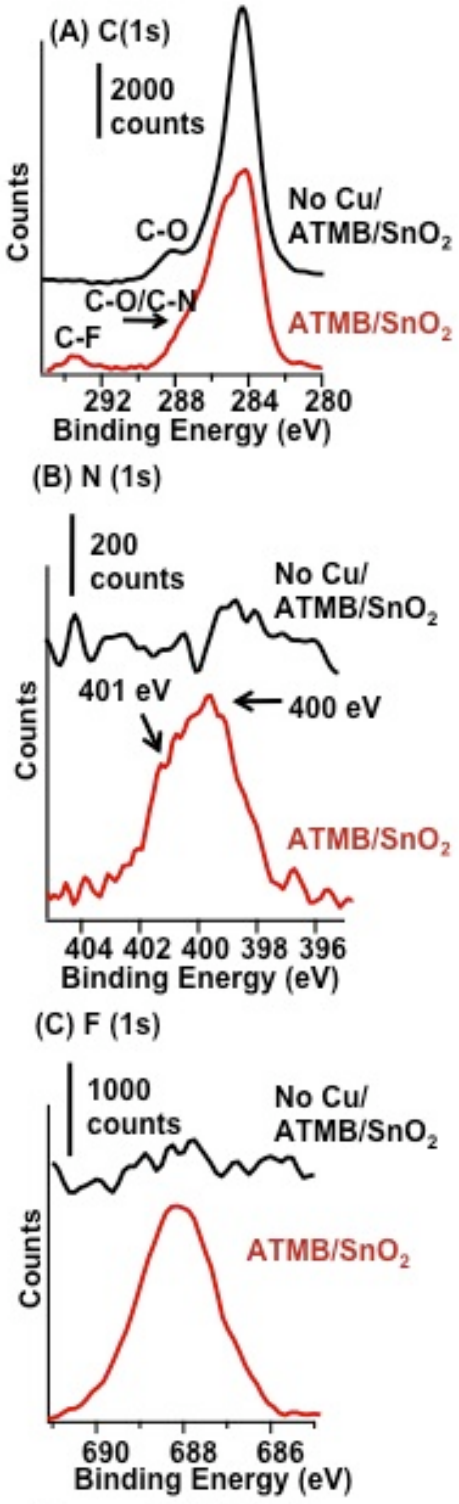

Figure 4.5: XPS high resolution scans of no-Cu control (black) and ATMB-modified SnO_2 (red) in the (A) C (1s) region, (B) N (1s) region, and (C) F(1s) region.

4.3.4. Maximization of ATMB Coverage Without Evidence of Polymerization Side-Reactions

Propargyl alcohol, under highly acidic conditions and elevated temperatures (>100°C) is capable of polymerization.[33,34] To ensure that polymerization does not occur at mild grafting temperatures while maximizing ATMB coverage, XPS analysis of the F (1s) and C (1s) peak areas relative to that of the Sn ($3d_{5/2}$) was compared ATMB modified samples that varied with initial grafting times. Samples were removed from the oven at varying intervals and were then subjected to CuAAC reaction with ATMB. The results are summarized in Table 4.1. There is some variability in the C/Sn ratio and the ATMB molecular coverage values, but there is no clear trend toward increasing molecular coverage observed. This suggests the thermal grafting is self-terminating at one monolayer and there is no evidence of a polymerization reaction occurring at 80°C with reaction times up to 3945 minutes.

Table 4.1: Summary of XPS analysis of ATMB-modified SnO_2 with increasing grafting times for initial alkyne modification

Grafting Time (min)	C/Sn Peak Ratio	ATMB molecules/ cm^2
1065	0.1845	5.89×10^{14}
2505	0.0986	3.54×10^{14}
3945	0.1694	6.09×10^{14}

4.3.5. Investigation of Aqueous Stability of ATMB Modified SnO_2 Surface and the Ether-like Linkage

To understand the stability of the thermally grafted propargyl alcohol linkage, the ATMB-modified SnO_2 nanocrystalline thin-films were subjected to various aqueous conditions. The characteristic C-F peak at 1222 cm^{-1}, as shown in Figure 4.6a-d, was used as a marker. The broadening and peak shift seen at pH 13 and 65°C can be explained by the increasing amount of water adsorption.[27] Figure 4.7, which gives the absolute peak intensities that were normalized to the same initial intensity versus time, shows the thermally grafted linkage is more stable at room temperature and pH 3 conditions than at pH 13 and 65°C H_2O, with the initial loss in intensity being the greatest. The thermally grafted alkyne and subsequent CuAAC reaction giving the ATMB-modified surface is stable in a variety of aqueous conditions for at least 72 hours.

A comparison of the thermally grafted alkyne versus carboxylic anchoring group was performed using propiolic acid, as shown in Figure 4.8. Using similar procedures reported in literature for carboxylic acid adsorption to metal oxides,[32,33] the propiolic acid was adsorbed onto the surface of SnO_2 nanocrystalline thin-film samples by submerging them overnight into a 9% (v/v) solution in methanol. FTIR analysis confirmed the presence of the alkyne group on the surface by the peak at 2120 cm^{-1} from the alkyne C-C bond. The change in the C=O stretch from 1680 cm^{-1} to 1625 and 1583 cm^{-1} for the asymmetric and symmetric carboxyl stretches, respectively, confirms the acid group becomes deprotonated upon adsorption to the surface of SnO_2.[32,34]

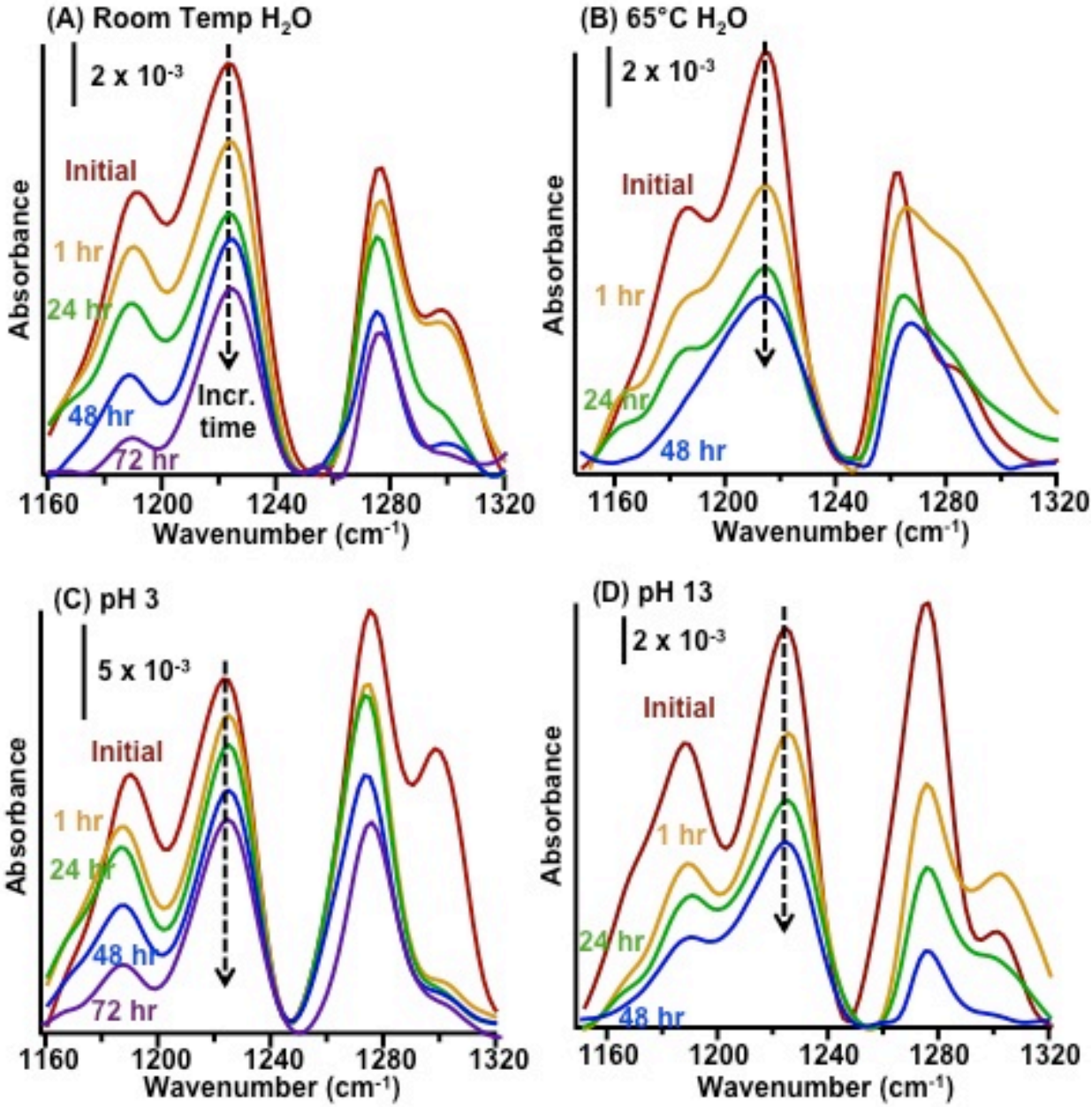

Figure 4.6: Enlarged (1160-1320 cm^{-1}) FTIR spectra of ATMB-modified SnO_2 thin films exposed to (A) room temperature H_2O, (B) 65°C H_2O, (C) pH 3, and (D) pH 13, for up to 72 hours. Absorbance value at 1222 cm^{-1} was used to track decrease in signal with increasing exposure time to various aqueous conditions

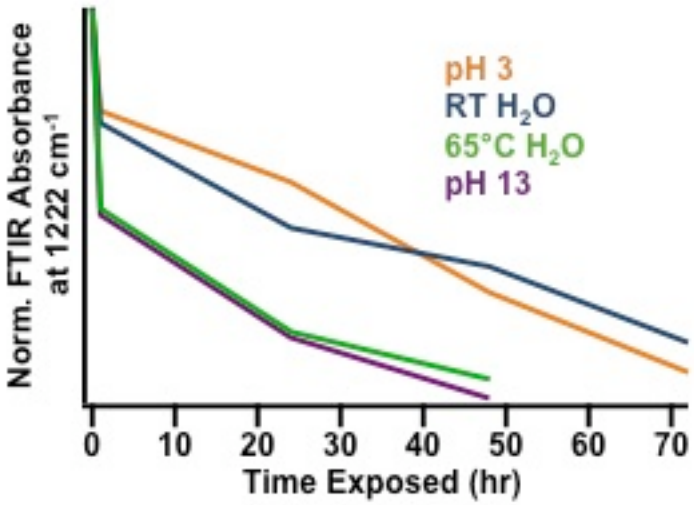

Figure 4.7: Normalized FTIR absorbance at 1222 cm^{-1}versus exposure time for each of the aqueous conditions. The thermal grafting functionalization and ATMB-modified SnO_2 thin film have greatest loss for pH 13 and 65°C H_2O aqueous conditions

The CuAAC reaction with ATMB was performed using the same procedure for the propargyl alcohol grafted samples. After CuAAC reaction, FTIR analysis reveals a broad peak, at 1216 cm^{1}, this peak is similar to C-F stretches; however, the characteristic triplet feature is not distinguishable as seen previously in Figure 4.4. One explanation for the discrepancy between the ATMB-modified SnO_2 through the two different methods of introducing an alkyne-modified surface is that H_2O is protonating the carboxylic acid linkage while the CuAAC reaction with ATMB is occurring, resulting in a reduced ATMB coverage.[27,35] It is observed that after CuAAC reaction, the reappearance of the C=O stretch at 1680 cm^{-1} from the protonated carboxylic functional group, suggests that the CuAAC reaction, which uses H_2O as a solvent, indeed causes protonation of the carboxyl anchoring group, thus changing the mode through which the alkyne is adsorbed to the surface and could lead to possible desorption.[34] From the FTIR analysis, it can be concluded that propiolic acid is capable of yielding an alkyne-modified SnO_2 nanocrystalline thin-film, however the CuAAC reaction conditions result in reduced ATMB coverage as well as the carboxylic acid linkage is capable of being protonated by H_2O.

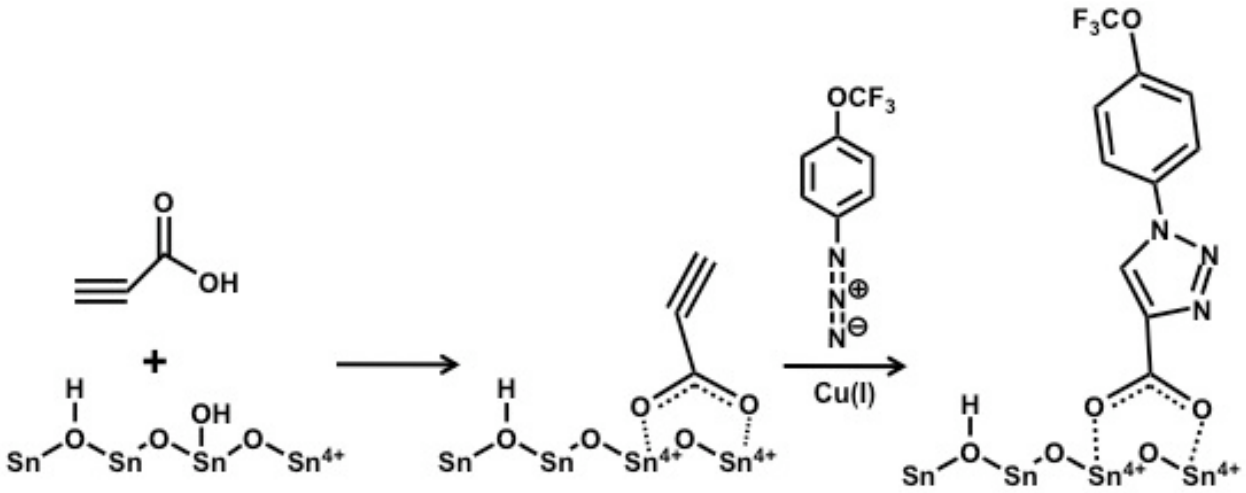

Figure 4.8: Reaction scheme for propiolic acid functionalization to give alkyne-modified SnO_2 followed by CuAAC reaction with ATMB

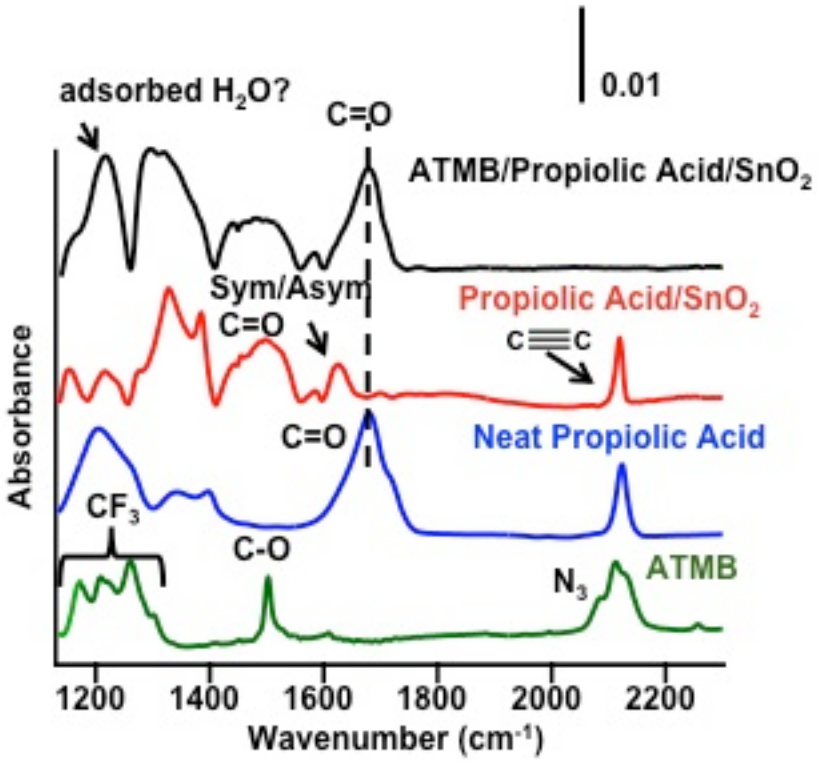

Figure 4.9: FTIR of ATMB (green) showing CF_3 triplet and azide stretch at 2115 cm^{-1}, neat propiolic acid scaled arbitrarily for clarity (blue) showing C=O stretch at 1680 cm^{-1}, propiolic acid modified SnO_2 (red) giving alkyne C-C stretch at 2120 cm^{-1} and change in C=O stretch to asymmetric stretch at 1625 cm^{-1} and symmetric at 1583 cm^{-1}, ATMB-propiolic acid SnO_2 (black) indicating the reappearance of the protonated C=O at 1680 cm^{-1} and the lack of distinctive CF_3 triplet stretch likely due to H_2O adsorption and desorption of propiolic acid.

4.4. Discussion

Thermal grafting of propargyl alcohol is capable of producing an alkyne-modified SnO_2 surface that is self-terminating. Although propargyl alcohol is capable of polymerization at temperatures >100°C or in the presence of concentrated acid, [36,37] the results reported here show no evidence of polymerization, likely due to the mild conditions used for thermal grafting. The thermal grafting occurs through the alcohol group, as evidenced by the ability for the alkyne group to participate in the CuAAC reaction with ATMB. The resulting ether-like linkage between the SnO_2 surface and the modified surface proves to be stable for at least 72 hours in a variety of aqueous conditions. This stability far exceeds reported results of other thermally grafted molecules.[22,23] A comparison of the introducing an alkyne-modified surface through the anchoring of a carboxylic acid group was performed using propiolic acid. The resulting alkyne-modified surface was not capable of producing an ATMB-modified surface with the surface coverage yield that is comparable to that of propargyl alcohol grafted surfaces likely due to H_2O causing protonation of the carboxyl group during the course of CuAAC reaction and leading to eventual desorption from the SnO_2 thin-film.

4.5. Conclusions

By exploiting the unique reactivity of the SnO_2 surface containing hydroxyl groups and exposed Sn^{4+} atomos which are highly Lewis acidic,[2] the method of thermally grafting propargyl alcohol provides a self-terminating short alkyl chain that allows for further fuctionalization by use of the CuAAC reaction. The resulting grafting

linkage is stable for several hours in a variety of aqueous conditions. The ability to form a stable surface species that is capable of undergoing a step-wise functionalization using a short alkyl chain poses many opportunities for future development in renewable energy applications, where the chain length of the organic interface controls electron injection.[8,9,38]

4.6. References

(1) Gupta, S. M.; Tripathi, M. *High Energy Chemistry* **2012**, *46*, 1.

(2) Batzill, M.; Diebold, U. *Progress in Surface Science* **2005**, *79*, 47.

(3) Alexander, B. D.; Kulesza, P. J.; Rutkowska, L.; Solarska, R.; Augustynski, J. *Journal of Materials Chemistry* **2008**, *18*, 2298.

(4) Devaraj, N. K.; Collman, J. P. *Qsar & Combinatorial Science* **2007**, *26*, 1253.

(5) Nebhani, L.; Barner-Kowollik, C. *Advanced Materials* **2009**, *21*, 3442.

(6) Landis, E. C.; Hamers, R. J. *Chemistry of Materials* **2009**, *21*, 724.

(7) Ruther, R. E.; Rigsby, M. L.; Gerken, J. B.; Hogendoorn, S. R.; Landis, E. C.; Stahl, S. S.; Hamers, R. J. *J. Am. Chem. Soc.* **2011**, *133*, 5692.

(8) Filippini, G.; Israeli, Y.; Goujon, F.; Limoges, B.; Bonal, C.; Malfreyt, P. *The Journal of Physical Chemistry B* **2011**, *115*, 11678.

(9) Chidsey, C. E. D.; Bertozzi, C. R.; Putvinski, T. M.; Mujsce, A. M. *Journal of the American Chemical Society* **1990**, *112*, 4301.

(10) Benson, M. C.; Ruther, R. E.; Gerken, J. B.; Rigsby, M. L.; Bishop, L. M.; Tan, Y. Z.; Stahl, S. S.; Hamers, R. J. *Acs Applied Materials & Interfaces* **2011**, *3*, 3110.

(11) Nishibayashi, Y.; Milton, M. D.; Inada, Y.; Yoshikawa, M.; Wakiji, I.; Hidai, M.; Uemura, S. *Chemistry-a European Journal* **2005**, *11*, 1433.

(12) *Chemistry of Tin*; 2nd ed.; Blackie Academic and Professional: London, 1998.

(13) Ljungdahl, N.; Kann, N. *Angewandte Chemie International Edition* **2009**, *48*, 642.

(14) Ju, Y.; Kumar, D.; Varma, R. S. *The Journal of Organic Chemistry* **2006**, *71*, 6697.

(15) Dureen, M. A.; Brown, C. C.; Stephan, D. W. *Organometallics* **2010**, *29*, 6594.

(16) Marcinko, S.; Fadeev, A. Y. *Langmuir* **2004**, *20*, 2270.

(17) Bishop, L. M.; Yeager, J. C.; Chen, X.; Wheeler, J. N.; Torelli, M. D.; Benson, M. C.; Burke, S. D.; Pedersen, J. A.; Hamers, R. J. *Langmuir* **2012**, *28*, 1322.

(18) Mani, G.; Johnson, D. M.; Marton, D.; Dougherty, V. L.; Feldman, M. D.; Patel, D.; Ayon, A. A.; Agrawal, C. M. *Langmuir* **2008**, *24*, 6774.

(19) Ciampi, S.; Bocking, T.; Kilian, K. A.; Harper, J. B.; Gooding, J. J. *Langmuir* **2008**, *24*, 5888.

(20) Yu, H.-Z.; Boukherroub, R.; Morin, S.; Wayner, D. D. M. *Electrochemistry Communications* **2000**, *2*, 562.

(21) Daugaard, A. E.; Hvilsted, S.; Hansen, T. S.; Larsen, N. B. *Macromolecules* **2008**, *41*, 4321.

(22) Chen, J.; Franking, R.; Ruther, R. E.; Tan, Y.; He, X.; Hogendoorn, S. R.; Hamers, R. J. *Langmuir* **2011**, *27*, 6879.

(23) English, C. R.; Bishop, L. M.; Chen, J. X.; Hamers, R. J. *Langmuir* **2012**, *28*, 6866.

(24) Houchin, M. R.; Warren, L. J. *Journal of Colloid and Interface Science* **1984**, *100*, 278.

(25) Takahashi, S.; Cohen, L. A.; Miller, H. K.; Peake, E. G. *The Journal of Organic Chemistry* **1971**, *36*, 1205.

(26) Wang, X. Y.; Landis, E. C.; Franking, R.; Hamers, R. J. *Accounts of Chemical Research* **2010**, *43*, 1205.

(27) Amalric-Popescu, D.; Bozon-Verduraz, F. *Catalysis Today* **2001**, *70*, 139.

(28) Moulder, J. F.; Stickle, W. F.; Sobol, P. E.; Bomben, K. D. *Handbook of X-ray Photoelectron Spectroscopy*; Perkin-Elmer Corporation: Eden Prarie, MN, 1992.

(29) Wagner, C. D.; Naumkin, A. V.; Kraut-Vass, A.; Allison, J. W.; Powell, C. J.; Rumble, J. R., Jr *NIST X-ray Photoelectron Spectroscopy Database*; National Institue of Standards and Technology: Gaithersburg, MD, 2003; Vol. Version 3.5.

(30) Franking, R.; Kim, H.; Chambers, S. A.; Mangham, A. N.; Hamers, R. J. *Langmuir* **2012**, *28*, 12085.

(31) Franking, R.; Hamers, R. J. *Journal of Physical Chemistry C* **2011**, *115*, 17102.

(32) Zhang, Q.-L.; Du, L.-C.; Weng, Y.-X.; Wang, L.; Chen, H.-Y.; Li, J.-Q. *The Journal of Physical Chemistry B* **2004**, *108*, 15077.

(33) Dobson, K. D.; McQuillan, A. J. *Spectrochimica Acta Part a-Molecular and Biomolecular Spectroscopy* **1999**, *55*, 1395.

(34) Neouze, M. A.; Schubert, U. *Monatshefte Fur Chemie* **2008**, *139*, 183.

(35) Titheridge, D. J.; Barteau, M. A.; Idriss, H. *Langmuir* **2001**, *17*, 2120.

(36) Yang, M. J.; Zheng, M.; Furlani, A.; Russo, M. V. *Journal of Polymer Science Part a-Polymer Chemistry* **1994**, *32*, 2709.

(37) Bartos, M.; Kapusta, S. D.; Hackerman, N. *Journal of the Electrochemical Society* **1993**, *140*, 2604.

(38) Listorti, A.; O'Regan, B.; Durrant, J. R. *Chemistry of Materials* **2011**, *23*, 3381.

Chapter 5

Ultra-thin ZrO_2 Coating on SnO_2 Nanocrystalline Thin-Film Enhances Electronic Coupling Between the Semiconducting Electrode and Adsorbed N719 Dye

5.1. Introduction

The improvement of photovoltaic devices, such as the DSSC, hinges on the ability to better understand and control the interfacial charge transfer between the organic or organometallic light absorber and the inorganic wide band-gap semiconductor.[1-3] TiO_2 has essentially dominated the DSSC research area due the relatively large tolerance to a variety of chemical conditions, low-toxicity, and inexpensive manufacturing costs.[4-7] However, SnO_2 has emerged as another promising candidate for solar energy technologies due to its electron mobility being orders of magnitude greater than TiO_2.[8,9] SnO_2 conduction band resides 0.5 eV lower in absolute energy thus electron injection from adsorbed dyes is thermodynamically more favorable as compared to TiO_2.[5,10] However, SnO_2 based DSSCs have yet to reach efficiency values that exceed TiO_2 based DSSCs.[11,12] Several studies have compared the initial electron injection into the conduction band of both of these metal oxides from an adsorbed dye have shown the rate of injection for SnO_2 is much less than TiO_2.[13-15] The discrepancies between the two metal oxides are theorized to exist due to the poor electronic overlap between the dye and the SnO_2 and/or the recombination rate dominating the lowered performance.[15-17]

Recently it has been shown that the introduction of a secondary metal oxide in the form of a conformal coating by either a deposition reaction or synthesis of core-shell structures increase the overall performance of SnO_2 solar devices.[11,18-27] One particular metal oxide of interest as a coating is ZrO_2 due to its relative chemical inertness, conduction band consisting of empty d-orbitals thought to increase electronic coupling between the semiconductor and dye, and the ability to reduce back electron transfer.[11,24,28] Kay et al, introduced a variety of metal oxide coatings to the SnO_2 nanoparticles before they were dispersed into a thin-film. They showed that the introduction of ZrO_2 on SnO_2 increased the solar efficiency and attributed the results to the reduction of back electron transfer from SnO_2 to the redox electrolyte and improved dye adsorption due to the increased basicity of the SnO_2 surface. Similarly, our results show that a ZrO_2 coating on the SnO_2 nanocrystalline thin-film also enhances the overall cell performance. Additionally, our time-resolved surface photovoltage measurements provide insight into the important role the ZrO_2 coating plays in the electronic coupling between the adsorbed dye and the nanocrystalline thin-film.

5.2. Experimental

5.2.1. Preparation of SnO_2 Nanocrystalline Thin Films and ZrO_2 Coated SnO_2 Nanocrystalline Thin Films

SnO_2 nanoparticles (20-70nm) were purchased from Nanostructured and Amorphous Materials. The nanoparticles were made into a paste using previously

developed procedures.[29] SnO_2 nanocrystalline thin-films were created by screen-printing the SnO_2 paste onto fluorine-doped tin oxide (FTO) deposited onto a glass slide (sheet resistance 15 Ω/sq). The films were then sintered at 500°C for ~2 hours to yield a nanocrystalline film with good electrical contact to the substrate. Scanning electron microscopy was performed to characterize the film thickness. The introduction of the ZrO_2 coating was completed using modified published procedures.[30,31] In summary, zirconium (IV) propoxide solution (70% v/v) in 1-propanol was introduced to the SnO_2 nanocrystalline thin-film on FTO in an inert atmosphere and allowed to react for ~1 minute. The films were then triply rinsed with inhibitor free anhydrous tetrahydrofuran (THF) followed by removal from the inert environment. The films were then heated to 400°C for ~1 hour. Scanning electron microscopy and x-ray photoelectron spectroscopy were performed to determine the extent of ZrO_2 conformal coating.

5.2.2. N719 Dye Loading Onto Nanocrystalline Thin Films

A concentrated solution of the ruthenium based dye, N719, (Silaronix) was created in a 1:1 mixture of anhydrous acetonitrile and n-butyl alcohol. Each of the thin films were submerged in the N719 solution for ~12 hours in an inert atmosphere. The ZrO_2 coated SnO_2 thin films were never soaked in the same container as the uncoated SnO_2 thin films to prevent undesired introduction of ZrO_2. Upon removal from the dye solution films were rinsed with anhydrous methanol to remove any un-adsorbed N719.

5.2.3. Optical Characterization

Diffuse reflectance UV-visible spectroscopy was completed using UV/Vis/NIR spectrometer (Jasco V-570) equipped with integrating sphere accessory. A Teflon spacer was used behind planar surfaces to ensure equal distance between sample surface and sampling window. Absorption spectra of solutions were obtained on a UV–visible spectrophotometer (UV240PC, Shimadzu).

5.2.4. Solar Cell Assembly and Experiment

The platnized counter electrode was created by spreading a thin layer of chloroplatinic acid hexahydrate solution (Sigma) on FTO glass slide. The electrode was then placed in a furnace at 470°C for 15 minutes. The electrolyte comprised of a 0.6M 1-propyl-3-methyl-imidazolium iodide (PMII), 0.03M I_2, 0.05M LiI, 0.1 M guanidine thiocyanate (GuNCS) and 0.5M 4-*tert*-butylpyridine (*t*-BP) in 85:15 anhydrous acetonitrile and valeronitrile. The custom built cell was assembled in a dry box with the counter electrode held by a 25 μm kapton spacer. The active area of the film was 0.196 cm^2 and the photovoltaic measurements were performed using solar simulator of 1 Sun, ~100 mW/cm^2.

5.2.5. Time-Resolved Surface Photovoltage (TR-SPV) Measurements

Time-resolved surface photovoltage measurements[32-34] were performed using a custom-made cell holder in which an FTO sense electrode was held 25 μm away from the sample surface. The sample was illuminated with short pulses (<3 ns, 200 μJ/pulse)

from a tunable laser system (NT340, Ekspla, Inc.); the resulting injection of electrons from the surface into the bulk induced transient changes in the potential, and these changes were measured at the pickup electrode. The sense electrode signal was amplified using a fast amplifier (Model TA2000B-3, FAST ComTec GmbH) with a 50 Ω input and output impedances, 1.5 GHz bandwidth, and 40x voltage gain. The amplified output was recorded on a sampling digital oscilloscope (Model DSO5054A, Agilent, Inc.).

5.2.6. Fourier-Transform Infrared (FTIR) Measurements

Infrared spectra were collected using an FTIR spectrometer (Vertex 70, Bruker Optics) at a resolution of 4 cm^{-1}. FTIR spectra were collected in single-bounce external reflection mode using a variable angle specular reflectance accessory with a wire grid polarizer (VeeMAX II, Pike Technologies). All reflection spectra were collected with p-polarized light at an incident angle of 50° from the surface normal. FTIR spectra of functionalized surfaces were measured using a background of 100 nm Au evaporated onto microscope glass slide. Residual baselines were removed to improve the clarity of the spectra. Baseline correction was achieved using a polynomial fit to remove sloping and/or curved background. A single polynomial was fit to each spectrum, taking care to avoid any regions containing peaks likely to be associated with surface species. The experimental spectrum was fit to a polynomial using all points in the selected regions, and the resulting polynomial was then subtracted from the data. In general, fits were

performed using several different polynomial orders in order to ensure that the spectral features observed were not sensitive to the precise details of the fitting procedure.

5.2.7. X-ray Photoelectron Spectroscopy (XPS) Measurments

XPS data were obtained using a custom-built XPS system consisting of a model 10–610 Al Kα source (1486.6 eV photon energy) with a Model 10–420 toroidal monochromator and a model 10–360 hemispherical analyzer with a 16-channel detector array; measurements were typically performed using an electron takeoff angle of 45°. Peak areas were calculated by fitting the raw data to Voigt functions after a Shirley baseline correction.[35,36] The spectra of each sample were shifted as necessary to make the primary C(1s) peak lie at a fixed energy of 284.4 eV; all other spectra for a given sample were shifted by the same amount. Concentration of Zr atoms/cm^2 was calculated using the equation shown:[37]

$$\frac{N_{Zr}\,atoms}{area} = \frac{A_{Zr}}{A_{Sn}}\frac{SF_{Sn}}{SF_{Zr}} \times \rho_{Sn:\,SnO_2} \times \lambda_{Sn:\,SnO_2} \times \cos\theta$$

Where A is the peak area, SF is the sensitivity factor reported in literature, density of Sn atoms in SnO_2, λ is the inelastic mean free path of Sn 3d electrons through SnO_2, and θ is the electron collection angle of 45°. The attenuation of Sn ($3d_{5/2}$) peak due to the ZrO_2 coating was determined to be negligible by experimental comparison of an uncoated SnO_2 thin film and a ZrO_2 coated thin film samples at the same sampling

alignment. These results were similar to what has been observed for ultra-thin coatings of ZrO_2 on a variety of surfaces.[38,39]

5.3. Results

5.3.1. Characterization of ZrO_2 coating on SnO_2 Nanocrystalline Thin Film

The ZrO_2 coating on SnO_2 reacts with the surface hydroxyl groups that are native to the SnO_2 surface, as shown in Figure 5.1. Upon exposure of zirconium (IV) propoxide solution to the SnO_2 surface, one or two of the propoxide ligands are displaced, leaving the Zr alkoxide directly bound to the surface of SnO_2. Any un-reacted zirconium (IV) propoxide is rinsed away by the THF, leaving only bound Zr atoms. The remaining alkoxide ligands are removed during the annealing process, giving the final ZrO_2 coating. Film thickness was determined by scanning electron microscopy (SEM) for both uncoated SnO_2 and ZrO_2 coated SnO_2 thin films.

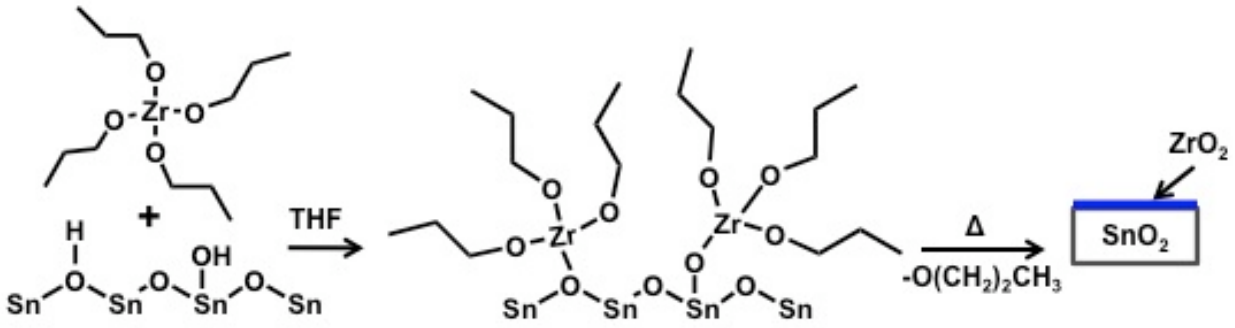

Figure 5.1: Reaction scheme for Zr (IV) propoxide reaction with SnO_2 surface resulting in ZrO_2 coating

As seen in Figure 5.2 there is no resolvable difference in the thickness and topography of the films after introduction of ZrO_2 coating. XPS analysis, in Figure 5.3, shows the appearance of Zr (3d) doublet at 184 eV, which is consistent with Zr atoms in ZrO_2.[38] Comparison of the Sn (3d) and Zr (3d) peak areas, atomic sensitivity factor values[40] of 4.095 for Sn ($3d_{5/2}$) and 2.216 for Zr (3d), an electron escape depth of ~2 nm give an approximate concentration of ~$2.57x10^{14}$ Zr atoms/cm^2, corresponding to about a monolayer of ZrO_2. [41]To determine the extent of ZrO_2 coating, the cycle of exposure to zirconium (IV) propoxide, THF rinse, and annealing was repeated multiple times. Additional cycles resulted in no experimental difference by XPS analysis, as summarized in Figure 5.4. One explanation for this observation is the reduced number of surface hydroxyl groups from the resulting ZrO_2 coating therefore the propoxide ligands are not displaced and the un-reacted zirconium (IV) propoxide is rinsed away. FTIR analysis was performed to confirm the difference of surface hydroxyl groups of a SnO_2 nanocrystalline thin film and a ZrO_2 coated SnO_2 nanocrystalline thin film. Figure 5.5 shows a sharp peak at 3480 cm^{-1} for the SnO_2 sample without ZrO_2, which corresponds to bridging surface hydroxyls that arise from the disassociation of water at the SnO_2 surface.[42] The ZrO_2 coated SnO_2 nanocrystalline thin film has a reduced peak that is shifted to 3467 cm^{-1}, this peak shift could be attributed to molecular water adsorbed on the surface of ZrO_2.[43] The reduction of surface hydroxyls and shift, combined with XPS and SEM analysis shows the coating is conformal, self-terminating at ~1 monolayer, and results in a change of the surface hydroxyl groups.

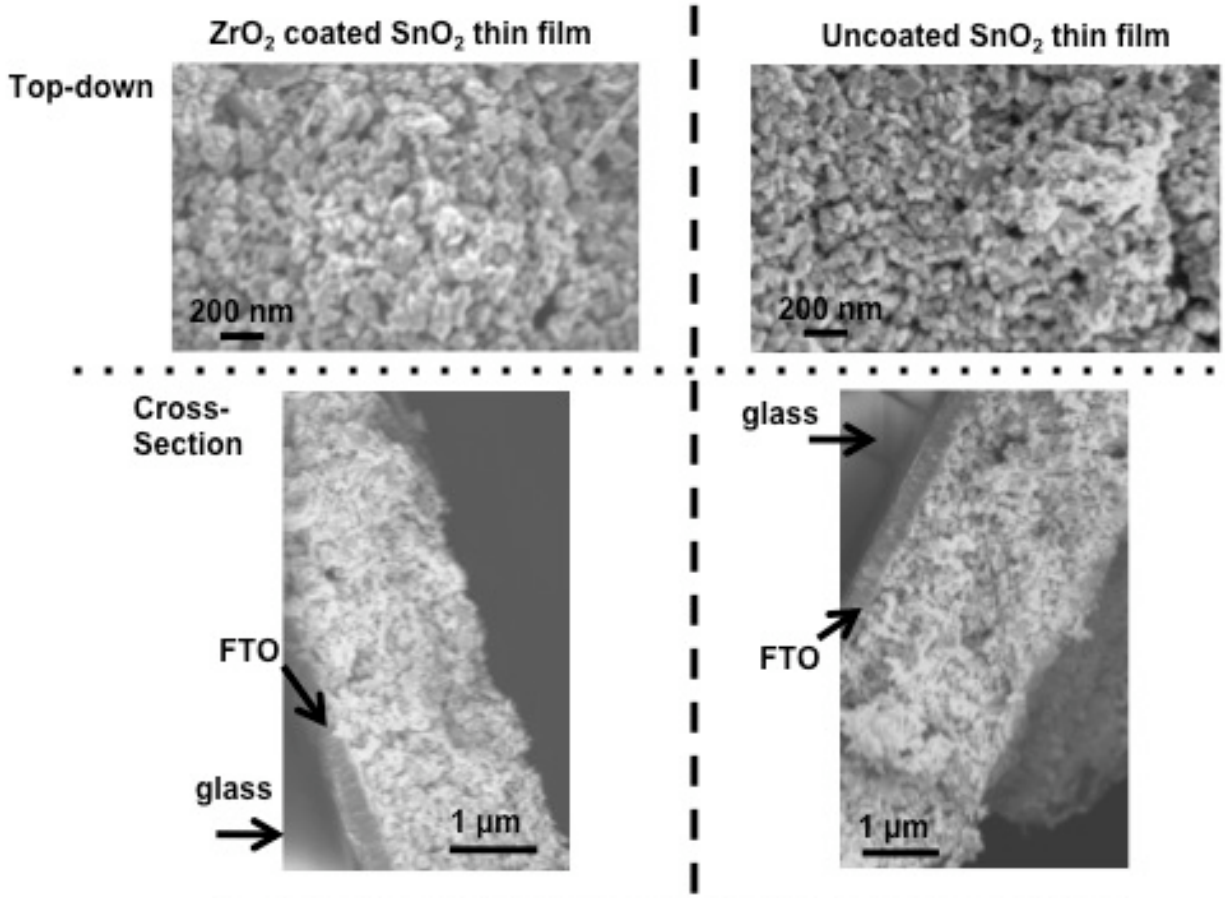

Figure 5.2: SEM images of ZrO_2 coated SnO_2 thin film on FTO and uncoated SnO_2 on FTO in top-down and cross-section views

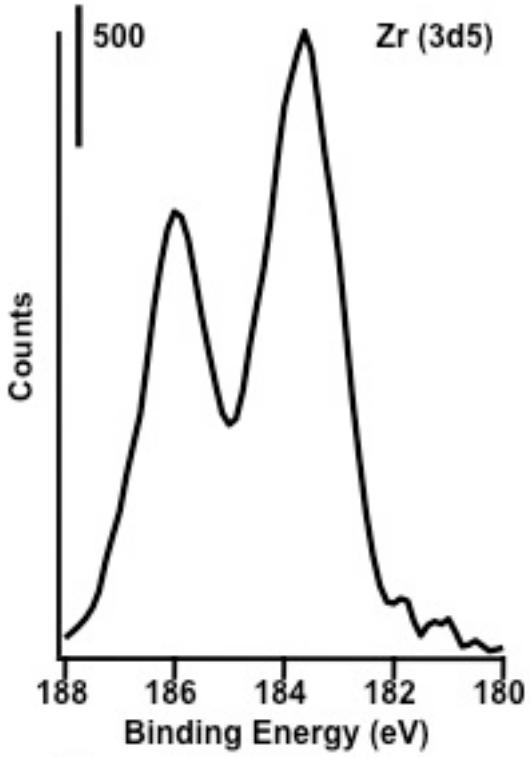

Figure 5.3: XPS High-resolution scan of Zr (3d5)

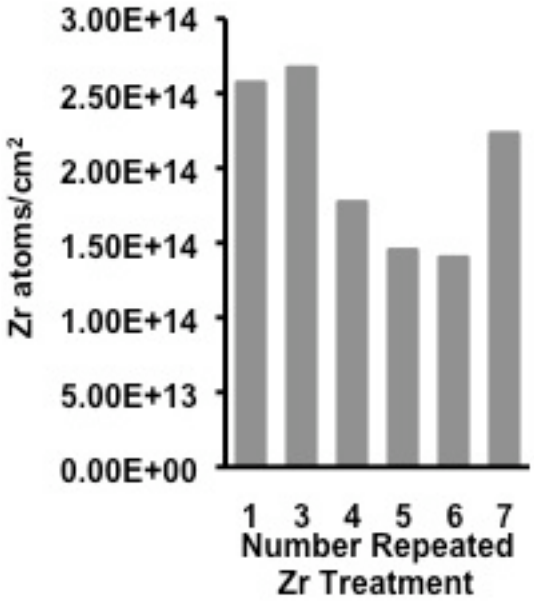

Figure 5.4: Bar graph showing the number of repeated Zr (IV) propoxide treatments and the coverage calculations by XPS analysis

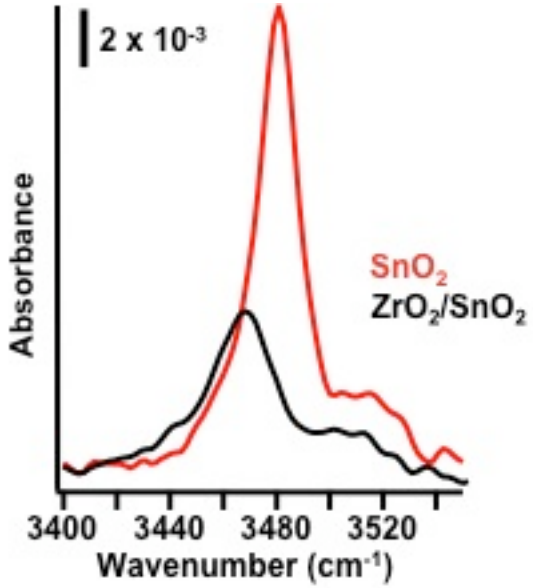

Figure 5.5: FTIR of –OH region for SnO_2 nanocrystalline thin film (red) and ZrO_2 coated SnO_2 nanocrystalline thin film (black(versus Au

5.3.2. N719 Dye Adsorption and Characterization

The ruthenium dye, N719, adsorbs to the metal oxide surface through the carboxylic groups as shown in Figure 5.6. N719 was adsorbed onto each of the nanocrystalline thin films as described in the experimental section, and diffuse reflectance UV-Vis was measured. The change in color of the films and the appearance of two peaks in the UV-Vis spectra shown in Figure 5.7 at 403 nm and 523 nm for both of the nanocrystalline thin-films confirms successful N719 dye loading, the slight red-shift from the peak maxima for N719 at 381 and 520 nm is indicative of increased delocalization upon dye adsorption to the nanocrystalline thin-film. XPS analysis of N719 on both of the nanocrystalline thin-films was performed to determine the approximate surface coverage of Ru atoms on each of the nanocrystalline films. Figure 5.8 shows the high resolution scan of the C (1s) peak at 284.4 eV, the Ru ($3d_{3/2}$) peak is not distinguishable from the C (1s) peak, however the Ru ($3d_{5/2}$) peak at 281 eV is clearly present. Using the Ru (3d) sensitivity factor of 3.696 and subtracting by 3/2 gives a value for the sensitivity of the Ru ($3d_{5/2}$) peak. The approximate coverage calculated was 6.49×10^{13} Ru atoms/cm^2 and 8.30×10^{13} Ru atoms/nm^2 for ZrO_2 coated SnO_2 and uncoated SnO_2, respectively. Based on the coverage estimations, the amount of N719 dye is experimentally not different for either of the films and can be concluded that any variances between these two films is not due to more favorable dye loading for either of the thin films.

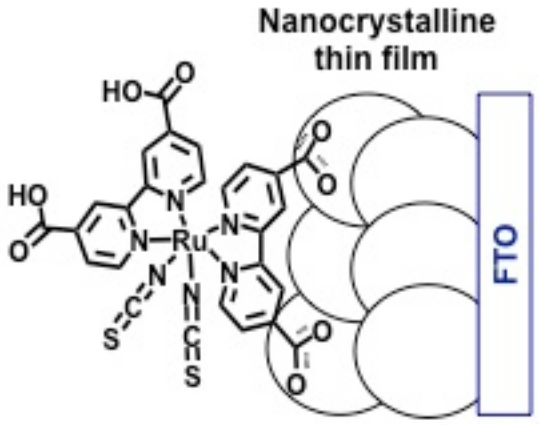

Figure 5.6: Representation of N719 adsorption onto nanocrystalline thin film

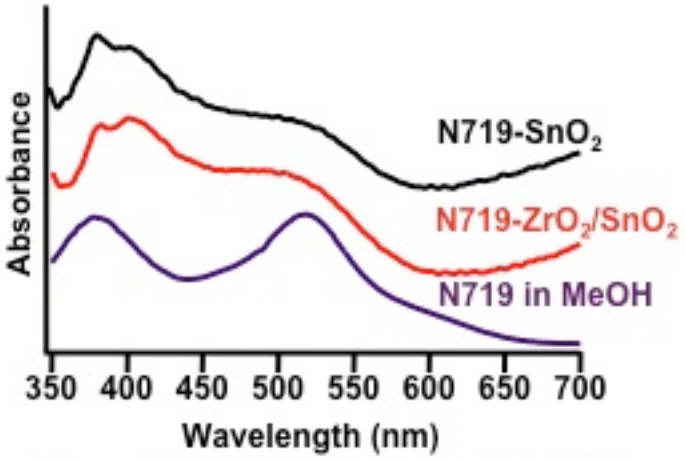

Figure 5.7: UV-Vis of N719 loaded SnO_2 (black), N719 loaded ZrO_2 coated SnO_2 (red), and N719 in methanol (purple)

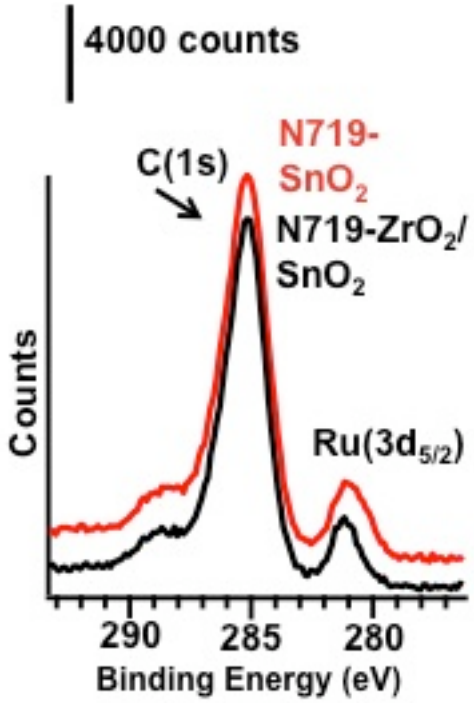

Figure 5.8: XPS high-resolution scan of Ru (3d) region for N719 on SnO_2 (red) and N719 on ZrO_2/SnO_2 (black)

5.3.3. Photovoltaic Characterization

Previous studies of a ZrO_2 coating through the introduction of a zirconium salt to suspended SnO_2 nanoparticles before being cast into a thin film showed that there was an enhancement in the solar efficiency. To confirm that our introduction of a ZrO_2 coating also showed an enhancement, we assembled the photovoltaic cell as described in the experimental section. The J-V curve generated, as seen in Figure 5.9 shows a greater J_{SC} at 2.635 mA for the ZrO_2 coated SnO_2 nanocrystalline thin-film and ~1.5 times enhancement in the efficiency, 0.707 %, versus the uncoated SnO_2 nanocrystalline thin-film with a J_{SC} of 1.869 mA and an efficiency of 0.531%. The J_{SC} is determined by the charge accumulation from the injected electrons that eventually becomes large enough that the electrons are transported to the FTO, this process is also in competition with the recombination.[44] Because the V_{OC} was comparable with 0.483 V for uncoated SnO_2 and 0.473 V for ZrO_2 coated SnO_2, we can conclude that in our system the nanocrystalline films have similar dynamic equilibrium for the recombination and electron generation.[44] Time-resolved surface photovoltage (TR-SPV) was used to better understand the origin of the J_{SC} change and the increase in efficiency of the N719 loaded nanocrystalline thin films.

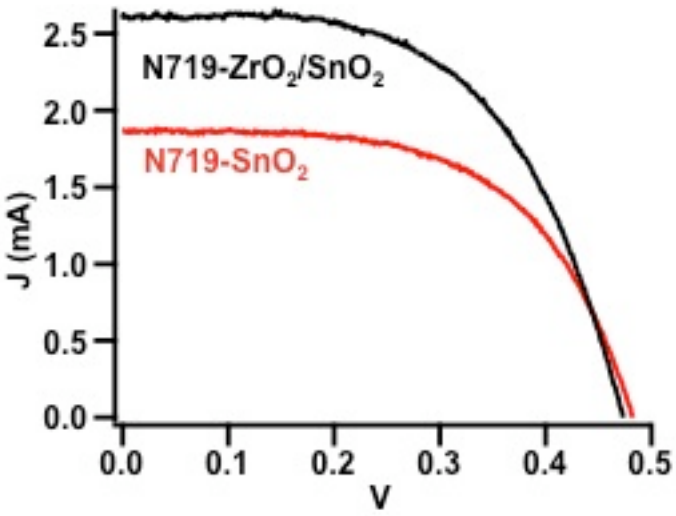

Figure 5.9: J-V curve at illumination of 1 sun

5.3.4. Time-Resolved Surface Photovoltage Characterization

The increase in the efficiency for metal oxide coated SnO_2 has been attributed to the metal oxide with greater conduction band energy introducing a potential barrier towards recombination, thus providing an overall reduction to back electron transfer.[11,45,46] Another possible explanation is the increased electronic coupling between the π* orbitals on the bypyridine ligand of N719 to the empty d-band orbitals introduced by ZrO_2 coating.[15] TR-SPV is used to probe the initial electron injection of the N719 dye as well the recombination. A TR-SPV experimental set up scheme can be seen in Chapter 2, Figure 2.15. A digital oscilloscope records a signal, shown in Figure 5.10a resulting from an excitation pulse of 200 μJ from the tunable Nd-YAG laser. The signal shows a sharp peak at t = 0 ns from the sense electrode polarizing caused by the accumulation of holes at the sample surface. A comparison to the bare films shows little response and only at short wavelengths. The peak maximum can be extracted and normalized per incident photon and plotted versus excitation wavelength to obtain information on the wavelength dependence. From Figure 5.10b, it is apparent that the initial charge injection for the ZrO_2 coated SnO_2 thin film is greater than the uncoated SnO_2 thin film. A comparison to the bare films shows minimal response with the greatest response only at short wavelengths. The change in sign followed by an exponential decay can be used to extract qualitative information about the recombination kinetics.

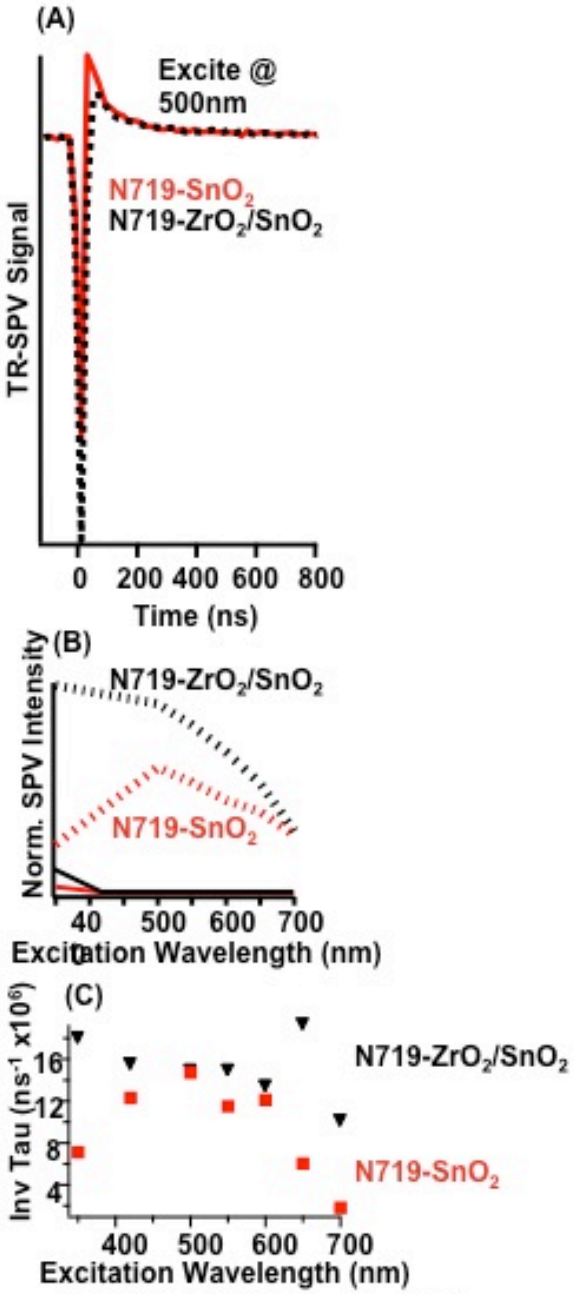

Figure 5.10: (A) TR-SPV signal at 500 nm excitation of N719-SnO_2 (red) and N719-ZrO_2/SnO_2 (dotted black); (B) Normalized SPV initial electron injection versus excitation wavelength for N719-ZrO_2/SnO_2 (dotted black), N719-SnO_2 (dotted red), bare ZrO_2/SnO_2 (solid black) and bare SnO_2 (solid red); (C) Qualitative rate of recombination versus excitation wavelength for N719-ZrO_2/SnO_2 (black triangles) and N719-SnO_2 (red squares)

Fitting the positive portion with a single exponential decay, gives a qualitative rate of recombination. It can be seen in Figure 5.10c that the rate of recombination is only reduced at short wavelengths (<350 nm) and long wavelengths (>650nm) but in the range the of N719 adsorption, the recombination rate is similar. The reduced recombination can be attributed to the suppression by the creation of a potential barrier.[11,45,46] Based on the TR-SPV results, we predict the electron injection enhancement is due to an increase in the electronic coupling between the nanocrystalline surface and the adsorbed dye and less due to reduced recombination.

5.4. Discussion

The addition of a ZrO_2 coating through the reaction of zirconium (IV) propoxide with the surface hydroxyl groups on SnO_2 provides a self-terminating monolayer. The motivation for introducing a ZrO_2 coating after the SnO_2 nanoparticles were processed into a thin film was to avoid creating insulating barriers between the nanoparticles which are known to result in reduced electron mobility.[26] The resulting ZrO_2 coating increases the solar conversion efficiency by ~1.5 times with an increase in the J_{SC}. The increase in J_{SC} could be the result of increased coupling between the π* orbitals on the bypyridine ligand on N719 dye and the introduction of d-band orbitals from the ZrO_2 coating. The TR-SPV measurements further elucidate the increased electronic coupling as evidenced by the increase in charge injection for the ZrO_2 coated SnO_2 thin films.[15,31]

A schematic representation of the band gap alignments, which assumes there is no interaction between the metal oxides and the adsorbed dye is shown in Figure 5.11. Previous studies on electron injection efficiency of adsorbed dye on ZrO_2 gave very low electron injection efficiency as compared to SnO_2 due to the conduction band alignment being less favorable.[17] Our results suggest that the electron injection is more favorable with the ZrO_2 coated SnO_2 nanocrystalline thin film than the uncoated SnO_2 nanocrystalline thin film therefore interaction between the SnO_2 and ZrO_2 coating must occur.[31] The addition of the ZrO_2 coating could create a surface with increased dye loading, which would appear as an enhancement in the electron injection for TR-SPV, however XPS analysis demonstrates that the N719 dye loading is not different. Therefore the electron injection enhancement is not due to increased dye loading. The recombination could also be decreased by the creation of the potential barrier; however, it is understood that the entire charge movement is within the bandwidth of the excitation pulse (<3 ns), therefore, the observations are only qualitative. A faster system is required to further investigate the electron injection rates of N719 into the conduction bands of ZrO_2 coated SnO_2 thin films and uncoated SnO_2 thin films.

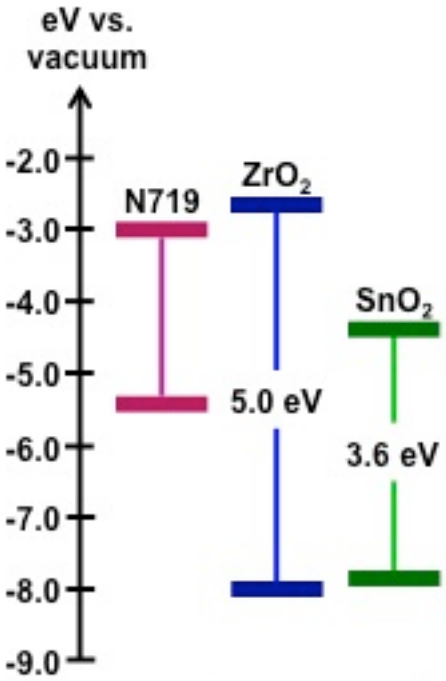

Figure 5.11: Illustration of band alignments for N719, ZrO_2, and SnO_2 assuming non-interacting conduction and valence bands

5.5 Conclusions

The addition of a ZrO_2 coating through the reaction of a zirconium alkoxide with the surface hydroxyl groups on SnO_2 provides a self-terminating monolayer. The ZrO_2 coating increased the solar efficiency as observed previously, which had been attributed to reduced recombination, however our TR-SPV results suggests the presence of Zr atoms increases the electronic coupling by introducing d band character.[11,31] The broad conduction band of SnO_2 consists of empty s and p orbitals from Sn^{4+}, and has a density of states several orders of magnitude lower compared to the TiO_2 conduction band comprised of d-orbitals.[47,48] For efficient charge injection to occur, the electronic coupling between the adsorbed dye and the semiconducting nanocrystalline thin-film needs to be favorable to reduce competing processes such as recombination.[49] The timescale of electron injection (<3 ns) is not accurately determined with the current Nd-YAG laser, however the magnitude of the TR-SPV signal is evidence that the electronic coupling between the N719 and the nanocrystalline film is enhanced. Increasing the electronic coupling between the adsorbed dye and SnO_2 through the introduction of an ultra-thin coating of a material that introduces d-band character may be a promising route to further increasing the efficiencies of future DSSCs.

5.6. References

(1) Grätzel, M. *Journal of Photochemistry and Photobiology C-Photochemistry Reviews* **2003**, *4*, 145.

(2) Wang, P.; Zakeeruddin, S. M.; Humphry-Baker, R.; Moser, J. E.; Gratzel, M. *Advanced Materials* **2003**, *15*, 2101.

(3) Watson, D. F.; Meyer, G. J. In *Annual Review of Physical Chemistry*; Annual Reviews: Palo Alto, 2005; Vol. 56, p 119.

(4) Ito, S.; Murakami, T. N.; Comte, P.; Liska, P.; Gratzel, C.; Nazeeruddin, M. K.; Gratzel, M. *Thin Solid Films* **2008**, *516*, 4613.

(5) Gratzel, M. *Nature* **2001**, *414*, 338.

(6) Chen, X.; Mao, S. S. *Chem. Rev.* **2007**, *107*, 2891.

(7) Nazeeruddin, M. K.; Kay, A.; Rodicio, I.; Humphrybaker, R.; Muller, E.; Liska, P.; Vlachopoulos, N.; Gratzel, M. *J. Am. Chem. Soc.* **1993**, *115*, 6382.

(8) Diebold, U. *Surf. Sci. Rep.* **2003**, *48*, 53.

(9) Batzill, M.; Diebold, U. *Progress in Surface Science* **2005**, *79*, 47.

(10) Hagfeldt, A.; Boschloo, G.; Sun, L. C.; Kloo, L.; Pettersson, H. *Chem. Rev.* **2010**, *110*, 6595.

(11) Kay, A.; Gratzel, M. *Chem. Mat.* **2002**, *14*, 2930.

(12) Snaith, H. J.; Ducati, C. *Nano Letters* **2010**, *10*, 1259.

(13) Bauer, C.; Boschloo, G.; Mukhtar, E.; Hagfeldt, A. *International Journal of Photoenergy* **2002**, *4*, 17.

(14) Benko, G.; Myllyperkio, P.; Pan, J.; Yartsev, A. P.; Sundstrom, V. *J. Am. Chem. Soc.* **2003**, *125*, 1118.

(15) Ai, X.; Anderson, N. A.; Guo, J. C.; Lian, T. Q. *Journal of Physical Chemistry B* **2005**, *109*, 7088.

(16) Green, A. N. M.; Palomares, E.; Haque, S. A.; Kroon, J. M.; Durrant, J. R. *Journal of Physical Chemistry B* **2005**, *109*.

(17) Katoh, R.; Furube, A.; Yoshihara, T.; Hara, K.; Fujihashi, G.; Takano, S.; Murata, S.; Arakawa, H.; Tachiya, M. *Journal of Physical Chemistry B* **2004**, *108*, 4818.

(18) Cai, F. S.; Yuan, Z. H.; Duan, Y. Q.; Bie, L. J. *Thin Solid Films* **2011**, *519*, 5645.

(19) Choi, S.-Y.; Kim, M.-H.; Kwon, Y.-U. *Physical Chemistry Chemical Physics* **2012**, *14*.

(20) Guo, J.; She, C.; Lian, T. *Journal of Physical Chemistry C* **2007**, *111*.

(21) Kim, J. Y.; Lee, S.; Noh, J. H.; Jung, H. S.; Hong, K. S. *Journal of Electroceramics* **2009**, *23*, 422.

(22) Kim, M. H.; Kwon, Y. U. *Journal of Physical Chemistry C* **2011**, *115*, 23120.

(23) Lee, C.; Lee, G. W.; Kang, W.; Lee, D. K.; Ko, M. J.; Kim, K.; Park, N. G. *Bull. Korean Chem. Soc.* **2010**, *31*, 3093.

(24) Li, T. C.; Goes, M. S.; Fabregat-Santiago, F.; Bisquert, J.; Bueno, P. R.; Prasittichai, C.; Hupp, J. T.; Marks, T. J. *Journal of Physical Chemistry C* **2009**, *113*, 18385.

(25) Niinobe, D.; Makari, Y.; Kitamura, T.; Wada, Y.; Yanagida, S. *Journal of Physical Chemistry B* **2005**, *109*.

(26) Palomares, E.; Clifford, J. N.; Haque, S. A.; Lutz, T.; Durrant, J. R. *J. Am. Chem. Soc.* **2003**, *125*, 475.

(27) Prasittichai, C.; Hupp, J. T. *Journal of Physical Chemistry Letters* **2010**, *1*, 1611.

(28) Comninellis, C.; Vercesi, G. P. *J. Appl. Electrochem.* **1991**, *21*, 335.

(29) Benson, M. C.; Ruther, R. E.; Gerken, J. B.; Rigsby, M. L.; Bishop, L. M.; Tan, Y. Z.; Stahl, S. S.; Hamers, R. J. *Acs Applied Materials & Interfaces* **2011**, *3*, 3110.

(30) Schwartz, J.; Bernasek, S. L. *Catalysis Today* **2001**, *66*, 3.

(31) Guo, J. C.; She, C. X.; Lian, T. Q. *Journal of Physical Chemistry C* **2007**, *111*, 8979.

(32) Anta, J. A.; Mora-Seró, I.; Dittrich, T.; Bisquert, J. *Journal of Physical Chemistry C* **2007**, *111*, 13997.

(33) Kronik, L.; Leibovitch, M.; Fefer, E.; Burstein, L.; Shapira, Y. *Journal of Electronic Materials* **1995**, *24*, 379.

(34) Mora-Séro, I.; Dittrich, T.; Garcia-Belmonte, G.; Bisquert, J. *Journal of Applied Physics* **2006**, *100*.

(35) Conny, J. M.; Powell, C. J. *Surface and Interface Analysis* **2000**, *29*, 856.

(36) Shirley, D. A. *Physical Review B* **1972**, *5*, 4709.

(37) Wang, X. Y.; Landis, E. C.; Franking, R.; Hamers, R. J. *Accounts of Chemical Research* **2010**, *43*, 1205.

(38) Chang, J. P.; Lin, Y. S.; Berger, S.; Kepten, A.; Bloom, R.; Levy, S. *Journal of Vacuum Science & Technology B* **2001**, *19*, 2137.

(39) Eswaranand, V.; Pradeep, T. *Journal of Materials Chemistry* **2002**, *12*, 2421.

(40) Moulder, J. F.; Stickle, W. F.; Sobol, P. E.; Bomben, K. D. *Handbook of X-ray Photoelectron Spectroscopy*; Perkin-Elmer Corporation: Eden Prarie, MN, 1992.

(41) Wagner, C. D.; Naumkin, A. V.; Kraut-Vass, A.; Allison, J. W.; Powell, C. J.; Rumble, J. R., Jr *NIST X-ray Photoelectron Spectroscopy Database*; National Institue of Standards and Technology: Gaithersburg, MD, 2003; Vol. Version 3.5.

(42) Pavelko, R. G.; Daly, H.; Hardacre, C.; Vasiliev, A. A.; Llobet, E. *Physical Chemistry Chemical Physics* **2010**, *12*, 2639.

(43) Merle-Méjean, T.; Barberis, P.; Othmane, S. B.; Nardou, F.; Quintard, P. E. *Journal of the European Ceramic Society* **1998**, *18*, 1579.

(44) O'Regan, B. C.; Durrant, J. R. *Accounts of Chemical Research* **2009**, *42*, 1799.

(45) Chen, S. G.; Chappel, S.; Diamant, Y.; Zaban, A. *Chem. Mat.* **2001**, *13*, 4629.

(46) Zaban, A.; Chen, S. G.; Chappel, S.; Gregg, B. A. *Chemical Communications* **2000**, 2231.

(47) Sorantin, P. I.; Schwarz, K. *Inorg. Chem.* **1992**, *31*, 567.

(48) Henrich, V. C., P. *The Surface Science of Metal Oxides*; Cambridge University Press: Cambridge, U.K., 1996.

(49) Listorti, A.; O'Regan, B.; Durrant, J. R. *Chem. Mat.* **2011**, *23*, 3381.

Chapter 6

Conclusions and Future Work

6.1. Conclusions

The work presented here showed a modular approach for tethering molecules that exhibit electrochemical, photoelectrochemical and electrocatalytic properties. The introduction of a surface bound azide group proceeded through a multi-step functionalization, which allowed for further reaction with molecules of interest. The first step involved the photochemical grafting of 3-buten-1-ol. The alcohol groups could then be replaced by a mesyl group, which provided an excellent leaving group for further transformations. The mesyl functional group was replaced by an azide group through a nucleophilic attack by N_3 upon treatment with NaN_3. The azide-modification proved to be a robust and not discriminatory towards different SnO_2 surfaces, including nanocrystalline thin films, nanorods, and planar fluorine-doped SnO_2. The azide-modified surfaces were able to undergo a cycloaddition reaction with a molecule bearing an alkyne functional group, through the CuAAC reaction.

The CuAAC reaction with an azide-modified surface yielded ferrocene and $[Ru(tpy)(tpy')]^{2+}$ modified SnO_2 nanocrystalline thin films. The ferrocene-modified thin films showed good electron transfer properties that exceed previous reports of ferrocene-modified SnO_2 and TiO_2 surfaces through a phosphine anchoring group.[1] $[Ru(tpy)(tpy')]^{2+}$ modified thin films are capable of separating photoexcited charges through excitation of the $[Ru(tpy)(tpy')]^{2+}$ followed by electron injection into the

conduction band of SnO_2. The electron injection occurs at all absorbing wavelengths of the $[Ru(tpy)(tpy')]^{2+}$ complex. We further tested the versatility of the azide functionalization technique on SnO_2 surfaces through the investigation of SnO_2 nanorods and planar FTO.

SnO_2 nanorods are an interesting nanostructure due to their reduced number of grain boundaries, which can retard electron mobilities.[2-5] The CuAAC reaction of the azide-modified SnO_2 nanorods with $[Ru(bpy)(tpy")Cl]^+$ produced photoelectrochemically active nanorods, where the $[Ru(bpy)(tpy")Cl]^+$ complex is capable of injecting photoexcited electrons at all absorbing wavelengths of the complex. The bare nanorods showed little photoelectrochemical response in the visible region. We tested the ability for the modular functionalization technique to produce a heterogeneous electrocatalytic system by tethering $[Ru(bpy)(tpy")Cl]^+$ to planar FTO. The $[Ru(bpy)(tpy")Cl]^+$-modified FTO electrodes were electrocatalytically active towards water oxidation, showing the $[Ru(bpy)(tpy")Cl]^+$ water oxidation properties were preserved after CuAAC reaction with azide-modified FTO. The tether proved to be stable in aqueous conditions at highly oxidizing potentials for over 10 minutes. We also investigated the CuAAC reaction with alkyne-modified SnO_2 thin films.

We have shown the versatility of CuAAC reaction with a variety of molecules and azide-modified SnO_2 surfaces, to demonstrate the ability for CuAAC reaction to proceed through an alkyne-modified surface; we used a short-chain alkyne. By exploiting the unique surface reactivity of SnO_2 which has highly Lewis acidic Sn^{4+} atoms and surface hydroxyl groups with pKas < 1,[6,7] we were able to thermally graft propargyl alcohol

through the alcohol group. The alkyne group was then exposed for further reaction via CuAAC with a small molecule bearing azido and trifluoromethoxy functional groups. The trifluoromethoxy group provided a distinct tag for XPS and FTIR analysis. The thermally grafted linkage and CuAAC reaction proved to give a stable modification that was able to withstand different aqueous conditions up to 72 hours. This stability far exceeds what has been shown for thermally grafted molecules on TiO_2 surfaces.[8,9]

Lastly, we investigated an ultra-thin coating of ZrO_2 to SnO_2 thin films through the reaction of Zr (IV) propoxide and the surface hydroxyl groups of SnO_2 and the resulting effect on electron injection. The ultra-thin coating is self-terminating at ~1 monolayer of ZrO_2 likely due to the reduction of surface hydroxyl groups after ZrO_2 coating introduction. Adsorption of a commercial Ru-based dye, N719, to both the ZrO_2 coated SnO_2 thin films and uncoated SnO_2 thin films, allowed for a direct comparison of initial electron injection via TR-SPV. Based on our results presented here, the ultra-thin coating of ZrO_2 on SnO_2 creates a surface in which initial electron injection from N719 is more favorable. We theorize the result of this observation is due to the increase in electronic coupling between the dye and the semiconductor surface through the introduction of d-band orbitals.[10,11]

6.2. Future Directions

The synthesis of stable interfaces introduces controllability and new degrees of versatility for the applications of SnO_2 in renewable energy technologies. We reported several SnO_2 surfaces that are capable of being modified with a variety of molecules that exhibit charge-transfer properties, however the modular functionalization technique can be extended to other applications such as scaffolds for polymerization reactions,[12] flexible platforms for organic light-emitting diodes,[13] and surfaces for the creation of biocompatible interfaces.[14] The introduction of ultra-thin coatings can drastically alter the surface that result in changes in surface hydroxyl groups as well as initial electron injection dynamics.[15-18] A comprehensive understanding of ultra-thin coatings can allow for better design of surfaces and interfaces for applications that rely on charge separation. From the work presented here, SnO_2 and the many functionalization techniques developed for SnO_2 can significantly broaden the applications for many different technologies and we predict the modular functionalization approach can be extended to several other metal oxide surfaces.

6.3. References

(1) Frantz, R.; Durand, J. O.; Lanneau, G. F.; Jumas, J. C.; Olivier-Fourcade, J.; Cretin, M.; Persin, M. *European Journal of Inorganic Chemistry* **2002**, 1088.

(2) Cheng, B.; Russell, J. M.; Shi, W. S.; Zhang, L.; Samulski, E. T. *J. Am. Chem. Soc.* **2004**, *126*, 5972.

(3) Shah, S.; Benson, M. C.; Bishop, L. M.; Huhn, A. M.; Ruther, R. E.; Yeager, J. C.; Tan, Y. Z.; Louis, K. M.; Hamers, R. J. *J. Mater. Chem.* **2012**, *22*, 11561.

(4) Wang, Y. L.; Guo, M.; Zhang, M.; Wang, X. D. *Crystengcomm* **2010**, *12*, 4024.

(5) Zhang, D. F.; Sun, L. D.; Yin, J. L.; Yan, C. H. *Advanced Materials* **2003**, *15*, 1022.

(6) Houchin, M. R.; Warren, L. J. *Journal of Colloid and Interface Science* **1984**, *100*, 278.

(7) Batzill, M.; Diebold, U. *Progress in Surface Science* **2005**, *79*, 47.

(8) English, C. R.; Bishop, L. M.; Chen, J. X.; Hamers, R. J. *Langmuir* **2012**, *28*, 6866.

(9) Chen, J.; Franking, R.; Ruther, R. E.; Tan, Y.; He, X.; Hogendoorn, S. R.; Hamers, R. J. *Langmuir* **2011**, *27*, 6879.

(10) Ai, X.; Anderson, N. A.; Guo, J. C.; Lian, T. Q. *Journal of Physical Chemistry B* **2005**, *109*, 7088.

(11) Guo, J.; She, C.; Lian, T. *Journal of Physical Chemistry C* **2007**, *111*.

(12) Schwartz, J.; Bernasek, S. L. *Catalysis Today* **2001**, *66*, 3.

(13) Andersson, A.; Johansson, N.; Broms, P.; Yu, N.; Lupo, D.; Salaneck, W. R. *Advanced Materials* **1998**, *10*, 859.

(14) Marti, A. *Injury-International Journal of the Care of the Injured* **2000**, *31*, S33.

(15) Li, T. C.; Goes, M. S.; Fabregat-Santiago, F.; Bisquert, J.; Bueno, P. R.; Prasittichai, C.; Hupp, J. T.; Marks, T. J. *Journal of Physical Chemistry C* **2009**, *113*, 18385.

(16) Lin, H.; Liu, Y. Z.; Liu, C. J.; Li, X.; Shen, H. P.; Zhang, J.; Ma, T. L.; Li, J. B. *J. Electroanal. Chem.* **2011**, *653*, 81.

(17) Niinobe, D.; Makari, Y.; Kitamura, T.; Wada, Y.; Yanagida, S. *Journal of Physical Chemistry B* **2005**, *109*, 17892.

(18) Palomares, E.; Clifford, J. N.; Haque, S. A.; Lutz, T.; Durrant, J. R. *Journal of the American Chemical Society* **2003**, *125*, 475.